Titre: Title:	Development of a Low-Noise Ultrafast Fiber Laser and Optimization of Nonlinear Crystals for Bright, High-Purity Entangled Photon Sources
Auteur: Author:	Colin Dietrich
Date:	2024
Type:	Mémoire ou thèse / Dissertation or Thesis
Référence: Citation:	Dietrich, C. (2024). Development of a Low-Noise Ultrafast Fiber Laser and Optimization of Nonlinear Crystals for Bright, High-Purity Entangled Photon Sources [Mémoire de maîtrise, Polytechnique Montréal]. PolyPublie. https://publications.polymtl.ca/59633/

POLYTECHNIQUE MONTRÉAL
affiliée à l'Université de Montréal

Development of a Low-Noise Ultrafast Fiber Laser and Optimization of Nonlinear Crystals for Bright, High-Purity Entangled Photon Sources

COLIN DIETRICH
Département de génie physique

Mémoire présenté en vue de l'obtention du diplôme de *Maîtrise* ès *sciences appliquées*
Génie physique

Octobre 2024

POLYTECHNIQUE MONTRÉAL
affiliée à l'Université de Montréal

Ce mémoire intitulé :

Development of a Low-Noise Ultrafast Fiber Laser and Optimization of Nonlinear Crystals for Bright, High-Purity Entangled Photon Sources

présenté par **Colin DIETRICH**
en vue de l'obtention du diplôme de *Maîtrise ès sciences appliquées*
a été dûment accepté par le jury d'examen constitué de :

Sébastien FRANCOEUR, président
Nicolas GODBOUT, membre et directeur de recherche
Denis SELETSKIY, membre

DEDICATION

To all my friends at the lab,
I will miss you...

À tous mes amis du labos,
vous me manquerez...

ACKNOWLEDGEMENTS

I would like to extend my deepest thanks to Dr. Stéphane Virally, who supervised me throughout this enriching project and taught me so much. I will always remember his unlimited dedication, ensuring we worked in the best conditions possible, the countless coffees and snacks, and, of course, his boundless love for Belgium.

I also wish to express my gratitude to Prof. Nicolas Godbout for giving me the opportunity to join the Laboratoire des Fibres Optiques, for providing valuable resources, and for serving as a member of my thesis jury.

Thank you to all my friends at the LFO and LODI. Special thanks to Rodrigo Becerra for teaching me so much, for his contagious positivity, and his humanity. A big thank you to Joseph Lamarre, without whom these two years of research would not have been the same, cheers to all the good moments we shared. I wish you all the best going forward. Thank you to Dr. Martin Poinsinet De Sivry and Raphaël Maltais-Tariant for the enjoyable times we spent together and for their wise advice throughout this journey. Many thanks to Sarah Albos and Valérie Monette for their kindness and support. Finally, thank you to all the lab members for the lunches, Spartan races, board games, and all the activities we shared.

I am especially grateful to the engineering physics technicians, particularly Mikael Leduc, who taught and assisted me greatly with the project, reminding me that sometimes you just have to dive in and test things without overthinking.

My thanks also go to the members of the FemtoQ group. First, to Prof. Denis Seletskiy for his wise advice throughout the project, and for including us in their enriching lab meetings. Special thanks to Patrick Cusson and Gabriel Demontigny for helping with both ultrafast photonics and quantum optics questions.

Finally, I would like to thank my friends and family outside the lab, particularly Titouan, Tom, Thomas, and Mathias, who helped clear my mind when it was most needed.

Lastly, I extend my gratitude to Professors Sébastien Francoeur and Denis Seletskiy for agreeing to be members of my jury, and I thank you in advance for your valuable feedback and comments, which will contribute to improving the quality of my thesis.

RÉSUMÉ

Cette thèse s'inscrit dans un projet plus vaste visant à développer une source fibrée brillante de photons intriqués, caractérisée par une haute pureté pour des applications en optique quantique. L'objectif est d'utiliser un laser à impulsions ultrarapides pour générer, via un processus de génération de seconde harmonique (SHG) suivi d'une conversion paramétrique spontanée (SPDC), des paires de photons intriqués à la même longueur d'onde que la source laser initiale. Une telle source quantique pourrait considérablement contribuer à la métrologie en offrant la possibilité de dépasser les limites classiques de résolution et de bruit. Ce travail pose les bases de ce projet à travers trois parties principales : la conception d'un laser fibré ultrarapide à faible bruit, l'application d'un processus de SHG pour le doublement de fréquence, et le développement d'un algorithme génétique pour optimiser les matériaux non linéaires du second ordre. Le système laser comprend un oscillateur maître (MO) à verrouillage de mode passif, associé à un amplificateur à fibre dopée à l'erbium (EDFA). Le MO génère des impulsions à une longueur d'onde centrale de 1559 nm, avec un taux de répétition de 60,9 MHz, des énergies d'impulsion allant de 30 à 75 pJ, et des durées comprises entre 594 et 312 fs, tout en maintenant un faible bruit d'intensité relatif de 0,081 %. L'EDFA amplifie les impulsions, élargissant ainsi la largeur spectrale de 4,5 à 55 nm avec une puissance moyenne de sortie maximale de 265 mW. Les mesures SHG FROG montrent une durée d'impulsion à la sortie de l'EDFA de 102 fs. Ces impulsions ont ensuite alimenté un processus de SHG dans un cristal de niobate de lithium périodiquement polarisé. Afin d'optimiser la puissance harmonique moyenne, tous les paramètres ont été ajustés, aboutissant à une période de réseau de 19,7 μm et une température de cristal de 70 °C, permettant ainsi d'obtenir des impulsions à une longueur d'onde centrale de 792 nm avec une puissance moyenne de 46 mW. Enfin, un algorithme génétique a été développé pour optimiser la structure des cristaux non linéaires du second ordre, améliorant les conditions d'accord de phase et la pureté spectrale des paires de photons intriqués générées par SPDC. Appliqué à la mise en phase de type II dans un cristal de phosphate de titanyle de potassium avec des impulsions de pompe centrées à 792 nm, cet algorithme a obtenu une fonction d'accord de phase avec une largeur de bande de 30 nm et une pureté spectrale de 98,5 %. De plus, il a démontré sa capacité à s'adapter à des profils cibles non conventionnels, montrant ainsi son potentiel pour diverses configurations. Les travaux futurs porteront sur la finalisation du processus SPDC et l'intégration des designs optimisés dans une source quantique complète.

ABSTRACT

This thesis is part of a broader project aimed at developing a bright, fiber-based source of entangled photons with high purity for quantum optics applications. The goal is to utilize an ultrafast pulsed laser to generate, via Second Harmonic Generation (SHG) followed by Spontaneous Parametric Down-Conversion (SPDC), entangled photon pairs at the same wavelength as the pump laser. Such a quantum source could significantly contribute to metrology by offering the potential to surpass the classical limits of resolution and noise. The work establishes the foundational steps of the project through three main components: the design of a low-noise ultrafast fiber laser, the implementation of the SHG process for frequency doubling, and the development of a genetic algorithm to optimize second-order nonlinear materials. The laser system includes a Master Oscillator (MO) employing passive mode-locking, combined with an Erbium-Doped Fiber Amplifier (EDFA). The MO produced pulses at a central wavelength of 1559 nm with a repetition rate of 60.9 MHz, pulse energies ranging from 30 to 75 pJ, and durations between 594 and 312 fs, along with a low relative intensity noise of 0.081%. The EDFA amplified the pulses, expanding the spectral bandwidth from 4.5 to 55 nm with a maximum averaged output power of 265 mW. SHG FROG measurements indicated a pulse duration of 102 fs at the output of the EDFA. These pulses were then used to drive the SHG process in a periodically poled lithium niobate crystal. All parameters were meticulously optimized to maximize the average harmonic power, resulting in a grating period of 19.7 μm and a crystal temperature of 70 °C, which produced pulses at a central wavelength of 792 nm with an average output power of 46 mW. Finally, a genetic algorithm was developed to optimize the structure of second-order nonlinear crystals, enhancing the phase-matching conditions and the spectral purity of the entangled photon pairs generated by SPDC. When applied to type-II phase matching in a Potassium Titanyl Phosphate crystal with pump pulses centered at 792 nm, the algorithm achieved a Phase Matching Function with a 30 nm spectral bandwidth and a spectral purity of 98.5%. It also demonstrated its capability to adapt to non-conventional target profiles, indicating its potential for various configurations. Future work will focus on completing the SPDC process and integrating the optimized designs into a functional quantum source.

TABLE OF CONTENTS

LIST OF TABLES

LIST OF FIGURES

LIST OF SYMBOLS AND ACRONYMS

APKTP	Aperiodically Poled Potassium Titanyl Phosphate
ASE	Amplified Spontaneous Emission
BBO	Beta Barium Borate
CNT-SA	Carbon Nanotube Saturable Absorber
CPA	Chirped Pulse Amplification
CW	Continuous Wave
DFG	Difference-Frequency Generation
EDFA	Erbium-Doped Fiber Amplifier
Er80	Erbium-Doped Polarization Maintaining Fiber
FC/APC	Fiber Connector / Angled Physical Contact
Fe	Iron
FR-103MN	Femtochrome autocorrelator model
FSR	Free Spectral Range
FTIR	Fourier-Transform Infrared Spectroscopy
FWM	Four-Wave Mixing
FWHM	Full Width at Half Maximum
GA	Genetic Algorithm
GDD	Group Delay Dispersion
GNLSE	Generalized Nonlinear Schrödinger Equation
GRIIRA	Green Induced Infrared Absorption
GVD	Group Velocity Dispersion
GVM	Group Velocity Mismatch
HWP	Half-Wave Plate
i-RIN	Integrated Root Mean Square Relative Intensity Noise
JSA	Joint Spectral Amplitude
KTP	Potassium Titanyl Phosphate
LIGO	Laser Interferometer Gravitational-Wave Observatory
MgO:PPLN	Magnesium Oxide-doped Periodically Poled Lithium Niobate
MO	Master Oscillator
MSE	Mean Squared Error
Nb	Niobium
NCME	Nonlinear Coupled Mode Equations
OCT	Optical Coherence Tomography

PBS	Polarizing Beam Splitter
PCGPA	Principal Component Generalized Projections Algorithm
PDC	Parametric Down-Conversion
PM	Polarization Maintaining
PM1550	Polarization-Maintaining fiber designed for 1550 nm operating wavelength
PM980	Polarization-Maintaining fiber designed for 980 nm operating wavelength
PMF	Phase Matching Function
PPLN	Periodically Poled Lithium Niobate
PPKTP	Periodically Poled Potassium Titanyl Phosphate
PSD	Power Spectral Density
QPM	Quasi-Phase Matching
RBW	Resolution Bandwidth
RIN	Relative Intensity Noise
RMS	Root Mean Square
SAM	Saturable Absorber Mirror
SESAM	Semiconductor Saturable Absorber Mirror
SFG	Sum-Frequency Generation
SH	Second Harmonic
SHG	Second Harmonic Generation
SHG FROG	Second Harmonic Generation Frequency-Resolved Optical Gating
SPAD	Single-Photon Avalanche Diode
SPDC	Spontaneous Parametric Down-Conversion
SPM	Self-Phase Modulation
SVEA	Slowly Varying Envelope Approximation
TBP	Time-Bandwidth Product
TEC	Thermoelectric Controller
THG	Third Harmonic Generation
TL	Transform-Limited
TOD	Third-Order Dispersion
WDM	Wavelength Division Multiplexer
XPM	Cross-Phase Modulation
Yb:KYW	Ytterbium-doped Potassium Yttrium Tungstate

LIST OF APPENDICES

CHAPTER 1 INTRODUCTION

1.1 General Introduction

Recent advancements in optical imaging and metrology have greatly improved the precision of measurement systems to the point where they are now often limited by the laws of quantum mechanics and quantum optics. The use of non-classical light sources has addressed these limitations, offering significant improvements in metrology. Non-classical light sources are known to enhance resolution and reduce noise [2–4]. A notable example is the use of bright squeezed states in the Laser Interferometer Gravitational-Wave Observatory (LIGO) interferometer for gravitational wave detection [5].

Traditional quantum light sources, which emit photons at detectable rates but with low brilliance, are not ideal for high-brightness applications such as imaging or spectroscopy in environments with substantial background noise [6]. This has led to an increased demand for more powerful quantum light sources that can provide the necessary photon flux for these applications.

At the same time, fiber-based light sources offer significant advantages, including ease of transport and operational flexibility, as they do not require precise alignment.

These advancements in quantum light sources could greatly benefit fields such as Fourier-Transform Infrared Spectroscopy (FTIR) [7, 8], quantum state tomography of light [9, 10], or Optical Coherence Tomography (OCT) [11, 12].

1.2 Research Objective

This thesis is part of a broader effort to design a fiber-based bright source of entangled photons. The project starts with the development of a low-noise, ultrafast fiber laser that serves as the pump. This pump is essential for achieving the high peak powers required to drive the nonlinear processes involved. It is used in a cascaded process that starts with Second Harmonic Generation (SHG) and is followed by Spontaneous Parametric Down-Conversion (SPDC) to generate entangled photon pairs at the same wavelength as the pump. The SPDC process is chosen to be non-degenerate to produce separable pairs (e.g. via polarization states in type-II SPDC). These bright branches of entangled photons, along with a small portion of the initial pump used as a local oscillator, have potential applications in several of the aforementioned fields. A specific application, inpired by the work of Virally et al. [13], sug-

gests that post-selection on one branch of a bright source of entangled photons produces pure quantum states in the twin branch, potentially offering significant metrological advantages over classical sources.

The focus of this thesis is on the initial stages of the project. This includes designing and characterizing the pump laser and implementing the SHG system. The next part of the project, the SPDC system for generating entangled photon pairs, has already begun and will be fully developed in another master's thesis.

Another objective of this work is to develop an algorithm for optimizing second-order nonlinear materials, which are crucial for bright quantum sources. Specifically, modulating the nonlinear susceptibility in these materials can significantly affect the spectral characteristics of the resulting optical processes. Building on previous methodologies, this algorithm is designed to enhance the spectral purity of entangled photon pairs generated through SPDC. By carefully adjusting phase-matching conditions within the crystal, the algorithm fine-tunes the crystal parameters to optimize either the phase matching function or the output spectra of the entangled pairs. Additionally, a collaboration has been initiated with the Fabulas Lab at Polytechnique Montréal to advance the development and design of these crucial second-order nonlinear materials.

1.3 Thesis Outline

This thesis is structured as follows: Chapter 2 reviews the theoretical background necessary for understanding the development and implementation of the proposed fiber-based laser system and the nonlinear processes it enables. Chapter 3 details the design, setup, and characterization of the master oscillator and erbium-doped fiber amplifier. Chapter 4 discusses the setup and results of the second harmonic generation and the single prism pulse compressor. Chapter 5 presents the optimization of second-order nonlinear materials using genetic algorithms. Finally, Chapter 6 summarizes the work and discusses the limitations, potential improvements, and future research directions.

CHAPTER 2 THEORY / LITERATURE REVIEW

2.1 Pulse Propagation in Optical Fibers

This section outlines the theoretical framework for developing an ultrafast fiber laser based on Agrawal's *Nonlinear Fiber Optics* [14], along with methodologies from previous projects at Polytechnique Montréal by Labranche [1] and Rivard [15]. Optical pulse generation process starts with a passive mode-locked fiber laser, amplified using an Erbium-Doped Fiber Amplifier (EDFA). This fiber laser relies on soliton propagation, wave packets that maintain their shape due to a balance between dispersion and nonlinearity.

The first part of this chapter derives the wave equation from Maxwell's equations to analyze light interaction with the fiber material. Section 2.1.1 examines the linear and nonlinear responses of the medium, specifically fused silica fibers used in the laser. The focus is on Group Velocity Dispersion (GVD) and Self-Phase Modulation (SPM). The interaction between SPM and GVD is crucial for stable soliton propagation.

A theoretical expression for a solitonic pulse is derived in Section 2.1.3, forming the basis for analyzing the operation of the laser. Section 2.1.4 examines passive mode-locking mechanisms and the influence of the saturable absorber on the lasing conditions.

Maxwell's Equations

In free space, light propagates without bounds, allowing it to spread or diffract freely [16]. In optical fibers, however, light is confined within the core by the surrounding cladding, guiding it along the fiber. This confinement affects the wave vector, propagation constant, and mode structure, which are important for understanding pulse propagation and dispersion effects [17].

To analyze light pulse transmission in optical fibers, Maxwell's equations provide the foundational framework:

$$\begin{cases} \nabla \times \mathbf{E} &= -\frac{\partial \mathbf{B}}{\partial t}, \\ \nabla \times \mathbf{H} &= \mathbf{J} + \frac{\partial \mathbf{D}}{\partial t}, \\ \nabla \cdot \mathbf{D} &= \rho_f, \\ \nabla \cdot \mathbf{B} &= 0. \end{cases} \tag{2.1}$$

Here, $\mathbf{E}$ and $\mathbf{H}$ represent the electric and magnetic field vectors, respectively. In optical fibers, where free charges and external electromagnetic sources are typically absent, $\mathbf{J}$ and

ρ_f are often assumed to be zero [17].

The electric flux density $\mathbf{D}$ and magnetic flux density $\mathbf{B}$ are related to the fields and material properties as follows:

$$\begin{aligned} \mathbf{D} &= \epsilon_0 \mathbf{E} + \mathbf{P}, \\ \mathbf{B} &= \mu_0 (\mathbf{H} + \mathbf{M}), \end{aligned} \tag{2.2}$$

where $\mathbf{P}$ and $\mathbf{M}$ are the induced electric and magnetic polarizations. In non-magnetic materials like optical fibers, $\mathbf{M} = 0$.

Using Maxwell's equations, the general wave equation is derived:

$$\underbrace{\nabla \times \nabla \times \mathbf{E}}_{=\nabla(\nabla\cdot\mathbf{E})-\nabla^2\mathbf{E}} - \frac{1}{c^2}\frac{\partial^2 \mathbf{E}}{\partial t^2} = \mu_0 \frac{\partial^2 \mathbf{P}}{\partial t^2}, \tag{2.3}$$

where $c = 1/\sqrt{\mu_0 \epsilon_0}$ is the speed of light in vacuum. This equation describes various optical phenomena. The left side represents the spatial and temporal variations of the electromagnetic field, while the right side represents the response of the medium, leading to linear effects like dispersion and nonlinear effects such as SHG, SPDC, and SPM.

2.1.1 Response of the Medium

The response of the medium to an incoming electric field plays a crucial role in determining how light propagates through it. By examining the right-hand term in the wave equation (2.3), different effects arising from this response can be analyzed.

The induced polarization in the medium can be divided into linear and nonlinear components:

$$\mathbf{P}_{\mathrm{L}}(\mathbf{r}, t) = \epsilon_0 \int_{-\infty}^{0} \chi^{(1)}(t') \cdot \mathbf{E}(\mathbf{r}, t - t') \, \mathrm{d}t', \tag{2.4}$$

$$\mathbf{P}_{\mathrm{NL}}(\mathbf{r}, t) = \epsilon_0 \int \cdots \int_{-\infty}^{0} \chi^{(n)}(t_1, \ldots, t_n) \vdots \mathbf{E}(\mathbf{r}, t - t_1) \cdots \mathbf{E}(\mathbf{r}, t - t_n) \, \mathrm{d}t_1 \cdots \mathrm{d}t_n, \tag{2.5}$$

where $\chi^{(n)}$ are tensors that depend on the polarization of the incoming electric field.

The linear polarization $\mathbf{P}_{\mathrm{L}}$ is associated with the first-order susceptibility $\chi^{(1)}$, which describes how the outer shell electrons of the medium respond proportionally to the applied field. This response is responsible for basic optical properties such as refraction and linear dispersion, where different frequencies of light travel at different speeds through the medium.

The nonlinear polarization $\mathbf{P}_{\mathrm{NL}}$ arises from the interaction between atomic clouds of neighbor-

ing atoms within the medium. These atomic clouds behave as coupled harmonic oscillators, which exhibit a nonlinear response under the influence of strong electromagnetic fields. This interaction results in higher-order susceptibilities $\chi^{(2)}, \chi^{(3)}, \ldots$, leading to effects such as SHG, Third Harmonic Generation (THG), and SPM. These nonlinear effects become significant at high local intensities and are critical in ultrafast and high-power optical systems.

Transitioning from the time domain to the frequency domain simplifies convolution products, transforming them into products in the frequency domain:

$$\mathbf{P} = \underbrace{\epsilon_0 \chi^{(1)} \cdot \mathbf{E_1}}_{\mathbf{P}^{\mathrm{L}}} + \underbrace{\epsilon_0 \left[\chi^{(2)} : \mathbf{E_1 E_2} + \chi^{(3)} \vdots \mathbf{E_1 E_2 E_3} + \ldots \right]}_{\mathbf{P}^{\mathrm{NL}}}. \tag{2.6}$$

Here, $\chi^{(1)}$, $\chi^{(2)}$, and $\chi^{(3)}$ correspond to the linear, second-order, and third-order nonlinear susceptibilities, respectively. The operators $\cdot$, $:$, and $\vdots$ denote first-, second-, and third-order tensor products. For linearly polarized fields, these tensors reduce to scalar forms, simplifying the mathematical treatment.

For the rest of this section, the following assumptions are made:

1. The optical field is assumed to be linearly polarized and maintains this polarization throughout the fiber, which simplifies the wave equation to a scalar form. This is valid given the use of polarization-maintaining fibers, which are specifically designed to prevent polarization drift.

2. The pulse spectrum is centered around a mean frequency ω_0 with a narrow spectral width $\Delta\omega$, such that $\frac{\Delta\omega}{\omega_0} << 1$. This is a reasonable assumption at telecommunications wavelengths (around 10^{15} s^{-1}), even for pulses as short as 100 femtoseconds, allowing the use of the Slowly Varying Envelope Approximation (SVEA).

3. The light pulse propagating along the z-axis with linear polarization can be expressed as:

$$E(\mathbf{r}, t) = A(z, t)\ F(x, y)\ e^{i\beta_0 z}\ e^{i\omega_0 t}. \tag{2.7}$$

   In this expression, $A(z, t)$ describes the amplitude of the pulse envelope, $F(x, y)$ represents the spatial distribution of the transverse electric field (which is determined by the core of the fiber structure), $e^{i\beta_0 z}$ accounts for the phase accumulation along the propagation direction, and $e^{i\omega_0 t}$ describes the oscillation at the carrier frequency. These components collectively describe how the pulse evolves as it travels through the fiber, considering both its spatial and temporal characteristics.

Linear Response

When a light pulse propagates through an optical fiber, the linear response of the medium, known as dispersion, plays a crucial role in altering the properties of the pulse. This response is governed by the linear susceptibility $\chi^{(1)}$, which determines the refractive index $n(\omega)$ and the absorption coefficient $\alpha(\omega)$. These parameters are essential for understanding how the pulse interacts with the medium. The dielectric constant, which encapsulates these effects, is given by:

$$\begin{aligned} \epsilon(\omega) &= 1 + \chi^{(1)}(\omega), \\ &= \left(n(\omega) + i\frac{\alpha(\omega)c}{2\omega} \right)^2 . \end{aligned} \tag{2.8}$$

The propagation constant $\beta(\omega)$, which describes how light propagates through the medium, can be derived from the refractive index:

$$\beta(\omega) = \frac{n(\omega)\omega}{c}. \tag{2.9}$$

Expanding $\beta(\omega)$ around a central frequency ω_0 using a Taylor series allows to understand the different dispersion effects on the pulse:

$$\beta(\omega) \approx \beta_0 + \beta_1(\omega - \omega_0) + \frac{1}{2}\beta_2(\omega - \omega_0)^2 + \frac{1}{6}\beta_3(\omega - \omega_0)^3 + \cdots , \tag{2.10}$$

where $\beta_0 = \beta(\omega_0)$, and $\beta_m = \left(\frac{d^m\beta}{d\omega^m}\right)_{\omega=\omega_0}$ for $m \geq 1$. Here, β_1 corresponds to the group velocity $v_g = \frac{1}{\beta_1}$, β_2 describes GVD, and β_3 accounts for Third-Order Dispersion (TOD).

To understand the influence of these components on an optical pulse as it propagates through a medium, it is essential to first examine how the pulse is represented in the spectral domain and how it behaves. The characteristics of an optical pulse, defined by its duration and spectral composition, can be expressed in the frequency domain as:

$$A(\omega) = \int_{-\infty}^{\infty} A(t)e^{-i\omega t}dt = |A(\omega)|e^{i\phi(\omega)}, \tag{2.11}$$

where $\phi(\omega) = \beta(\omega)z$ represents the spectral phase, which determines the phase shift experienced by each frequency component of the pulse. When the spectral phase is constant or linear with frequency, the pulse is unchirped and at the transform limit, meaning its temporal duration and spectral bandwidth achieve the minimum possible product. For Gaussian and

sech^2 pulses, the Time-Bandwidth Product (TBP) is given by:

$$\text{TBP} = \Delta\omega\Delta t = 0.44 \quad \text{(for Gaussian)} \quad \text{and} \quad 0.315 \quad \text{(for sech}^2\text{)}. \tag{2.12}$$

However, if the spectral phase has a nonlinear dependence on frequency, the pulse becomes chirped. This chirping effect is largely influenced by GVD, represented by the quadratic term in the Taylor expansion (2.10). This quadratic phase shift causes different frequency components to travel at varying speeds, leading to either temporal broadening or compression of the pulse. For instance, if a pulse with negative GVD passes through a medium with normal dispersion ($\beta_2 > 0$), it will compress. Conversely, if it propagates through a medium with anomalous dispersion ($\beta_2 < 0$), it will broaden further. Similarly, a pulse with positive GVD will compress in an anomalous dispersion medium and broaden in a normal dispersion medium.

To quantify this, consider an initially unchirped pulse with duration τ_0 and a central wavelength of 1550 nm propagating through a length L of fused silica fiber. The temporal broadening of the pulse due to anomalous dispersion is influenced by its initial shape, typically modeled as hyperbolic secant (sech^2) or Gaussian. The extent of this broadening is described by:

$$\Delta\tau_{\text{Gaussian}} = \tau_0\sqrt{1 + \left(\frac{4\ln 2 \cdot \beta_2 L}{\tau_0^2}\right)^2}, \quad \Delta\tau_{\text{sech}^2} = \sqrt{\tau_0^2 + \left(\frac{4\beta_2 L}{\tau_0}\right)^2}. \tag{2.13}$$

Additionally, TOD, represented by the cubic term in the Taylor expansion (2.10), introduces further complexities by affecting the symmetry and coherence of the pulse. TOD can induce ripples in the pulse envelope and cause temporal asymmetry, complicating the propagation dynamics. These effects are particularly significant in ultrafast optics, where precise control of pulse shape and duration is crucial.

Second-Order Nonlinear Response

Following the discussion on linear dispersion effects, it is important to consider nonlinear interactions, specifically those governed by the second-order susceptibility tensor, $\chi^{(2)}$. This tensor is responsible for phenomena such as SHG, Sum-Frequency Generation (SFG), Difference-Frequency Generation (DFG), and SPDC. However, these effects occur only in non-centrosymmetric materials.

An intuitive explanation decsribed in [18] comes from the symmetry properties of the polarization response in a medium. In centrosymmetric materials, the induced polarization response

to an electric field remains symmetric. This symmetry causes the second-order nonlinear polarization to cancel out under parity transformation, resulting in $\chi^{(2)} = 0$. Physically, this means that the influence of the electric field is mirrored equally in opposite directions, effectively canceling the second-order effect. In non-centrosymmetric materials, this symmetry is absent, allowing the nonlinear polarization to contribute, enabling the manifestation of second-order effects.

In the case of fused silica fibers, which are centrosymmetric, these second-order effects are negligible. Further discussions on this topic, especially regarding SPDC, will be explored in the chapter on spontaneous parametric down-conversion.

Third-Order Nonlinear Response

After addressing linear and second-order nonlinear effects, third-order nonlinear response can also play an important role in the pulse behavior. Particularly as the pulse exits the erbium-doped fiber amplifier with high peak powers. Under such conditions, several nonlinear effects arise, with SPM being the most significant.

The third-order nonlinear susceptibility, $\chi^{(3)}$, governs critical effects such as THG, Four-Wave Mixing (FWM), and nonlinear refraction. In standard fused silica fibers, where second-order effects are negligible, third-order nonlinear phenomena predominantly shape the optical behavior. However, in optical fibers, processes like THG and FWM tend to be inefficient without phase matching, leaving nonlinear refraction as the primary mechanism. This effect leads to an intensity-dependent refractive index.

To derive this intensity dependence, the second-order term in the polarization expansion is disregarded, focusing on light linearly polarized along the x-axis. This simplification reduces the susceptibility tensor to scalar components, $\chi^{(1)} = \chi^{(1)}_{xx}$ and $\chi^{(3)} = \chi^{(3)}_{xxxx}$. The induced polarization then becomes:

$$P(\omega) = \epsilon_0 \left(\chi^{(1)} + \underbrace{\frac{3}{4}\chi^{(3)}|A(\omega)|^2}_{\epsilon_{NL}} \right) A(\omega). \tag{2.14}$$

This expression introduces a nonlinear part of a dielectric constant ϵ_{NL}, allowing the third-order nonlinear contribution to the induced polarization to be expressed as $P^{(3)}_{\mathrm{NL}}(\omega) \approx \epsilon_0 \epsilon_{\mathrm{NL}} A(\omega)$.

This formulation leads to a new effective intensity-dependent refractive index n_{eff} and ab-

sorption coefficient α_{eff}:

$$\epsilon(\omega) = 1 + \chi^{(1)}(\omega) + \epsilon_{\text{NL}} = (n_{\text{eff}}(\omega) + i\alpha_{\text{eff}}(\omega)c/2\omega)^2, \tag{2.15}$$

with

$$n_{\text{eff}}(\omega) = n(\omega) + n_2(\omega)|A(\omega)|^2, \qquad \alpha_{\text{eff}}(\omega) = \alpha(\omega) + \alpha_2(\omega)|A(\omega)|^2. \tag{2.16}$$

Here, $n_2(\omega)$ is the nonlinear refractive index, and $\alpha_2(\omega)$ is the two-photon absorption coefficient, defined as:

$$n_2(\omega) = \frac{3}{8n(\omega)}\text{Re}[\chi^{(3)}], \qquad \alpha_2(\omega) = \frac{3\omega}{4n(\omega)c}\text{Im}[\chi^{(3)}]. \tag{2.17}$$

These expressions highlight how the intensity of light modifies the refractive properties of the medium through third-order nonlinear effects. This intensity dependence leads to various nonlinear phenomena, including SPM and Cross-Phase Modulation (XPM).

The nonlinear parameter,

$$\gamma(\omega_0) = \frac{\omega_0 n_2(\omega_0)}{cA_{\text{eff}}}, \tag{2.18}$$

where A_{eff} is the effective mode area of the fiber, is crucial for quantifying the strength of these effects in the fiber.

SPM occurs when an intense light beam induces a refractive index change proportional to its intensity. This modulation causes different parts of the beam to experience varying phase shifts, altering the phase of the light wave across the beam profile. The phase shift from SPM is given by:

$$\Delta\phi_{\text{SPM}}(\omega) = n_2(\omega)|A(\omega)|^2\beta(\omega)L, \tag{2.19}$$

where $\beta(\omega)$ is the propagation constant described in the next section, and L is the propagation length.

This phase modulation leads to changes in the instantaneous frequency of the light, contributing to spectral broadening. As the frequency components generated by SPM propagate, they interfere, creating spectral ripples. These ripples significantly impact the coherence and spectral output of the light source.

Higher-Order Nonlinear Response

Higher-order nonlinear responses, associated with odd-order susceptibilities such as $\chi^{(5)}$ and $\chi^{(7)}$, involve interactions where the induced polarization depends on higher powers of the electric field intensity. These responses lead to more complex nonlinear phenomena, including

higher harmonic generation, multi-photon absorption, and higher-order Kerr effects. As previously discussed for $\chi^{(2)}$, higher even-order nonlinear susceptibilities can be disregarded in centrosymmetric materials

In fused silica fibers, however, these higher-order nonlinear effects are negligible. This is due to the significantly smaller magnitude of higher-order susceptibilities, the much higher light intensities required to observe these effects, and the difficulty in achieving efficient phase matching under typical experimental conditions.

2.1.2 Fiber Modes

In the previous discussion, nonlinear optical phenomena were examined without considering the transverse distribution of the optical field, particularly in bulk media, where boundary effects can be disregarded due to the large size of the medium compared to the wavelength of light. However, in optical fibers, the behavior of light is fundamentally different. The propagation is no longer governed by simple plane waves but instead by well-defined transverse modes. These modes are dictated by the structural design and boundary conditions of the fiber, each associated with a unique propagation constant β. While this section provides only an intuitive overview of fiber modes to keep the theory concise, a more detailed treatment can be found in [14].

Although the representation of the wave changes in fibers, the fundamental principles governing both linear and nonlinear optical responses remain the same. The key difference in fibers is that the wavenumber $k(\omega)$ is often expressed as the propagation constant $\beta(\omega)$, where $k(\omega) = \frac{\omega n}{c}$ and $\beta(\omega) = \frac{\omega n_{\text{eff}}}{c}$. Here, n_{eff} is the effective refractive index, which depends on the specific mode of the fiber, incorporating both material dispersion, waveguide structure and boundary conditions.

Neglecting nonlinear polarization ($P_{\text{NL}} = 0$) in the wave equation and assuming low optical losses and uniform refractive index $n(\omega)$ in the core and cladding of step-index fibers, the equation simplifies to the Helmholtz Equation:

$$\Delta \mathbf{E}(\mathbf{r}, \omega) + n^2(\omega) \frac{\omega^2}{c^2} \mathbf{E}(\mathbf{r}, \omega) = 0. \tag{2.20}$$

Solving this under the given boundary conditions defines the guided modes, each with a propagation constant β, typically denoted as β_{mn} for mode indices m and n.

For linearly polarized modes, often used under the weakly guiding approximation, the modes are denoted as LP_{mn}, where m and n correspond to azimuthal and radial mode numbers. This approximation assumes a predominantly transverse and linearly polarized electric field

due to the small refractive index difference between the core and cladding.

In more complex fiber geometries, vector modes are denoted as HE_{lm}, where l and m indicate the modal order. These hybrid modes, such as HE_{11}, the fundamental mode in single-mode fibers, are solutions to the full vectorial wave equations, including both electric and magnetic field components in the direction of propagation. These modes accurately describe wave propagation in fibers with higher index contrasts and significant polarization effects.

2.1.3 Theoretical Foundations of Soliton Propagation

General Pulse Propagation Equation

In the previous section, the transverse mode of the electric field was derived from the Helmholtz Equation in the linear regime ($P_{\mathrm{NL}} = 0$). Now, by including the nonlinear polarization P_{NL} as a small perturbation to the linear polarization P_L, the starting equation becomes:

$$[\Delta + \beta(\omega)]E(\mathbf{r}, \omega) = -\mu_0 P_{\mathrm{NL}}(\mathbf{r}, \omega). \tag{2.21}$$

To obtain a general pulse propagation equation, several aspects must be considered:

1. The slowly varying approximation is applied, where $\frac{\partial^2 A(\omega,z)}{\partial z^2} \ll 2\beta_z(\omega)\frac{\partial A(\omega,z)}{\partial z}$, allowing the second derivative of $A(\omega, z)$ with respect to z to be neglected. This is valid because the envelope varies much more slowly than the carrier wave.

2. The propagation constant $\beta(\omega)$ is expanded as a Taylor series around the central frequency ω_0:
$$\beta(\omega) \approx \beta_0 + \beta_1(\omega - \omega_0) + \frac{1}{2}\beta_2(\omega - \omega_0)^2 + \dots \tag{2.22}$$

3. The nonlinear polarization P_{NL} is expanded, retaining only the third-order nonlinear terms since $\chi^{(2)} \approx 0$ in fused silica fibers, and higher-order terms are significantly weaker. Additionally, two-photon absorption is negligible in optical fibers.

4. For ultrashort optical pulses (<1 ps), the instantaneous response assumption of $\chi^{(3)}$ is invalid due to intrapulse Raman scattering, where high-frequency energy is transferred to lower frequencies, causing a spectral red shift. The third-order susceptibility, modified to account for this temporal dynamic, is given by:
$$\chi^{(3)}(t - t_1, t - t_2, t - t_3) = \chi^{(3)} R(t - t_1)\delta(t_1 - t_2)\delta(t - t_3), \tag{2.23}$$
where $R(t)$ is the normalized Raman response function.

5. The spectral width of such pulses is large enough to require considering the frequency dependence of the parameters α and γ by performing a Taylor expansion around the central frequency:

$$\begin{aligned}\gamma(\omega) &= \gamma(\omega_0) + \gamma_1(\omega-\omega_0) + \frac{1}{2}\gamma_2(\omega-\omega_0)^2,\\ \alpha(\omega) &= \alpha(\omega_0) + \alpha_1(\omega-\omega_0) + \frac{1}{2}\alpha_2(\omega-\omega_0)^2,\end{aligned} \tag{2.24}$$

where $\gamma_m = \left(\frac{\mathrm{d}^m\gamma}{\mathrm{d}\omega^m}\right)_{\omega=\omega_0}$ and $\alpha_m = \left(\frac{d^m\alpha}{d\omega^m}\right)_{\omega=\omega_0}$.

Considering these factors, a simplified version of the Generalized Nonlinear Schrödinger Equation (GNLSE) is obtained:

$$\begin{aligned}&\frac{\partial A(t,z)}{\partial z} + \frac{1}{2}\left(\alpha(\omega_0) + i\alpha_1\frac{\partial}{\partial t}\right)A(t,z) - i\sum_{n=1}^{\infty}\frac{i^n\beta_n}{n!}\frac{\partial^n A(t,z)}{\partial t^n}\\ &\qquad = i\left(\frac{\mathrm{d}^m\gamma}{\mathrm{d}\omega^m}\right)_{\omega=\omega_0}(\gamma(\omega_0) + i\gamma_1\frac{\partial}{\partial t})A(z,t)\int_0^{\infty}R(t')|A(z,t-t')|^2\,dt'.\end{aligned} \tag{2.25}$$

This equation covers a broad range of optical pulses and is applicable to pulses spanning just a few optical cycles, provided that a sufficient number of higher-order dispersion terms are incorporated.

Soliton

When a pulse propagates through an anomalous dispersion medium, such as fused silica fibers, a stable solution to the GNLSE emerges, known as a soliton. This stability results from a precise balance between GVD, which tends to broaden the pulse in the temporal domain, and SPM, which acts to compress it. The interaction between these two effects leads to a pulse that maintains its shape and energy during propagation, known as a soliton.

To derive the soliton solution, several simplifying assumptions are made. Higher-order dispersion terms beyond the second order are neglected, as their impact is minimal compared to the dominant second-order term. Absorption is also considered negligible due to the low optical losses in fused silica fibers. The temporal frame is shifted by defining $\tau = t - \beta_1 z$, which allows the pulse envelope to be tracked as it propagates along the fiber. These assumptions reduce the GNLSE to a simpler form:

$$\frac{i\partial A(t,z)}{\partial z} + \frac{i\alpha(\omega_0)}{2}A(t,z) - \frac{\beta_2}{2}\frac{\partial^2 A(t,z)}{\partial t^2} + \gamma(\omega_0)|A(t,z)|^2A(t,z) = 0 \tag{2.26}$$

Introducing the dimensionless variables,

$$u(t,z) = N\frac{A(t,z)}{\sqrt{P_0}}, \quad \xi = \frac{z}{L_D}, \quad t' = \frac{\tau}{\tau_0}, \tag{2.27}$$

further simplifies the analysis, where P_0 is the peak power of the pulse, $L_D = \tau_0^2/|\beta_2|$ is the dispersion length, and τ_0 is the pulse duration. The dimensionless parameter N is defined as $N^2 = \gamma P_0 L_D$, where N represents the soliton order. The equation for the pulse then becomes:

$$i\frac{\partial u(t',\xi)}{\partial \xi} + \frac{1}{2}\frac{\partial^2 u(t',\xi)}{\partial t'^2} + |u(t',\xi)|^2 u(t',\xi) = 0. \tag{2.28}$$

This equation has a well-known solution for $N = 1$, which corresponds to the fundamental soliton:

$$u(t',\xi) = \eta\,\mathrm{sech}(\eta t')e^{i\eta^2\xi/2} \quad \longrightarrow \quad A(z,t) = \sqrt{P_0}\,\mathrm{sech}(t/\tau_0)\,e^{iP_0\gamma(\omega_0)z/2}, \tag{2.29}$$

where η is an arbitrary parameter that represents the amplitude of the soliton.

Physically, this means that a fundamental soliton propagates through the fiber without changing its shape, thanks to the exact balance between the dispersive spreading of the pulse and the nonlinear self-focusing effects due to SPM. The sech function describes the temporal shape of the soliton, which is characteristic of the ability of the pulse to resist dispersion. The exponential term represents the phase evolution, indicating that while the shape of the pulse remains unchanged, its phase evolves in a predictable manner.

A key result from this derivation is the area theorem, given by:

$$P_0\tau_0^2 = \frac{\beta_2}{\gamma(\omega_0)} \tag{2.30}$$

This theorem states that the product of the peak power of the pulse and the square of its duration is a constant determined by the dispersion and nonlinearity parameters of the fiber. It implies that for a given fiber, reducing the pulse duration requires an increase in peak power, and vice versa.

2.1.4 Mode-Locking in Fiber Lasers

The laser built in this work relies on mode-locking to generate ultrashort laser pulses, typically in the picosecond (10^{-12} s) or femtosecond (10^{-15} s) range, by phase-locking multiple longitudinal modes in the laser cavity. This results in constructive interference and the formation of short pulses.

In laser operation, stable lasing occurs when the gain from the gain medium, such as a pumped erbium-doped fibers, equals the losses in the optical cavity. The cavity length L must satisfy the resonance condition for stable modes, with mode frequencies separated by the Free Spectral Range (FSR):

$$\nu_m = \frac{mc}{2L}, \quad \Delta\nu_{\text{FSR}} = \frac{c}{2L}, \quad \text{Gain} = \text{Loss}. \tag{2.31}$$

Mode-locking is achieved by favoring temporal modes with higher energies, locking the phases between different frequency components, resulting in the production of ultrashort pulses. In this work, passive mode-locking is implemented using a saturable absorber.

Saturable Absorber Mirror

The laser setup uses a Saturable Absorber Mirror (SAM) with a Bragg reflector. The performance of the SAM is defined by its modulation depth (ΔR), which quantifies the change in reflectivity from low intensity (R_{low}) to saturation intensity (R_{sat}):

$$\Delta R = R_{\text{low}} - R_{\text{sat}}.$$

This parameter influences laser dynamics in several ways [19]:

- **Threshold for Mode-Locking:** The modulation depth establishes the minimal light intensity necessary for mode-locking, correlating directly with the power required to transition the SAM between high and low absorption states. A higher modulation depth thus necessitates a greater intensity threshold.
- **Pulse Shaping:** Higher modulation depths facilitate the generation of shorter, more intense pulses by rendering the SAM transparent only at peak intensities.
- **Soliton Stability:** Insufficient modulation depth may fail to suppress Continuous Wave (CW) background or multiple pulsing, risking unstable mode-locking and noisy output.

Temperature variations also significantly affect SAM performance due to:

- **Thermal Expansion:** Higher temperatures lead to greater optical thickness and shift the spectral reflection of the SAM towards longer wavelengths.

- **Band Gap Reduction:** As temperature rises, the semiconductor band gap in the SAM narrows, allowing it to absorb photons of lower energy and saturate at longer wavelengths. This not only shifts the central wavelength but also affects the modulation depth, as the SAM starts to saturate at reduced energy levels with lower saturation reflectivity.

Given these temperature-dependent effects on the performance of the SAM, it is crucial to maintain precise temperature control of the SAM to ensure stable laser operation.

This section provided the necessary background on pulse propagation in optical fibers, including wave equation derivation, medium responses, and mode-locking principles using a saturable absorber. The practical implementation, involving laser system setup and characterization, will follow in Chapter 3, where these concepts will be applied experimentally. Building on this, the next chapter delves into the SHG process, where the laser will drive collinear SHG in a Periodically Poled Lithium Niobate (PPLN) crystal. The theoretical concepts essential for understanding SHG in this context are primarily drawn from Boyd's *Nonlinear Optics* [20].

2.2 Theoretical Development of Second Harmonic Generation

SHG is a fundamental nonlinear optical process in which an electric field interacts within a nonlinear material to produce a second harmonic electric field with twice the frequency (half the wavelength) of the fundamental field (see figure 2.1). This process is governed by the second-order nonlinear susceptibility $\chi^{(2)}$ in non-centrosymmetric material such as Lithium niobate or Potassium titanyl phosphate.

2.2.1 Second-Order Nonlinear Interactions

Second-order nonlinear processes involve interactions where energy and momentum are conserved among three electromagnetic fields in a non-centrosymmetric medium. These processes, known as three-wave mixing, require phase matching to ensure consistent phase relationship between the interacting waves as they propagate.

Several types of $\chi^{(2)}$ frequency conversion processes can occur depending on the momentum conservation and the input fields:

- **SHG:** Two photons from an input field combine to form a single photon with twice the frequency. The phase matching condition is $2\mathbf{k}_{\mathrm{F}} = \mathbf{k}_{\mathrm{SH}}$.

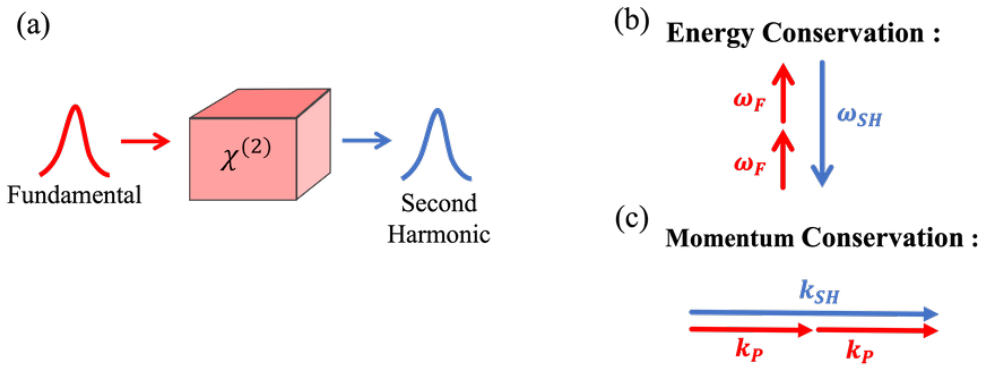

Figure 2.1 (a) Schematic of the SHG process in a nonlinear crystal. (b) Energy conservation between the fundamental and second harmonic photons. (c) Momentum conservation showing the relationship between the wave vectors of the fundamental and second harmonic photons.

- **SFG:** Two input fields combine to produce a single output field with a frequency equal to the sum of the input frequencies. The phase matching condition is $\mathbf{k}_1 + \mathbf{k}_2 = \mathbf{k}_{\text{SFG}}$.
- **DFG:** Two input fields produce an output field with a frequency equal to the difference between the input frequencies. The phase matching condition is $\mathbf{k}_1 - \mathbf{k}_2 = \mathbf{k}_{\text{DFG}}$.
- **SPDC:** A single input field interacts with quantum vacuum fluctuations, similar to DFG where one of the input fields is the vacuum. This interaction leads to the spontaneous generation of two output entangled fields, known as the signal and idler, with lower frequencies. The phase matching condition is $\mathbf{k}_{\text{pump}} = \mathbf{k}_{\text{signal}} + \mathbf{k}_{\text{idler}}$.

In the case of collinear propagation of the interacting fields, for efficient SHG, the phase mismatch $\Delta\mathbf{k} = 2\mathbf{k}_{\text{F}} - \mathbf{k}_{\text{SH}}$ must be minimized throughout the interaction. However, due to material dispersion, perfect phase matching is often difficult to achieve. This results in a lack of true momentum conservation, leading to destructive interference and reduced conversion efficiency. **Quasi-Phase Matching (QPM)** addresses this issue by using periodic modulation of the nonlinear susceptibility $\chi^{(2)}$ within the material to compensate for phase mismatch.

QPM is typically implemented through **periodic poling**, where the $\chi^{(2)}$ susceptibility of the crystal is periodically inverted at regular intervals along the propagation direction. This inversion effectively resets the phase of the interacting waves, allowing constructive interference to accumulate over longer distances. The poling period Λ is chosen to satisfy the condition:

$$\Lambda = \frac{2\pi}{\Delta\mathbf{k}} \quad \longrightarrow \quad \Delta\mathbf{k}_{\text{QPM}} = 2\mathbf{k}_{\text{F}} - \mathbf{k}_{\text{SH}} - \frac{2\pi}{\Lambda}. \tag{2.32}$$

By carefully designing the poling period, phase mismatch can be compensated, enhancing the efficiency of the nonlinear process.

In cases where periodic poling does not optimize phase matching across the entire interaction bandwidth, particularly for broadband or complex wave interactions, **aperiodic poling** is used. Aperiodic poling typically enables conversion across a wider range of wavelengths [21].

Figure 2.2 illustrates the influence of phase matching on the intensity of the Second Harmonic output field. In Figure 2.2(a), a bulk crystal with perfect phase matching shows a rapid increase in intensity, indicating that the interacting fields remain in phase, allowing efficient energy transfer. In Figure 2.2(b), imperfect phase matching in a bulk crystal results in intensity oscillations, as the fields periodically fall out of phase. Figure 2.2(c) showcases a periodically poled crystal utilizing quasi-phase matching, where periodic flipping of the nonlinear profile of the crystal extends the effective interaction length, leading to enhanced intensity growth. Finally, Figure 2.2(d) presents an aperiodically poled crystal, which enables precise control of the field evolution through variations in the poling period, optimizing output characteristics such as spectral purity.

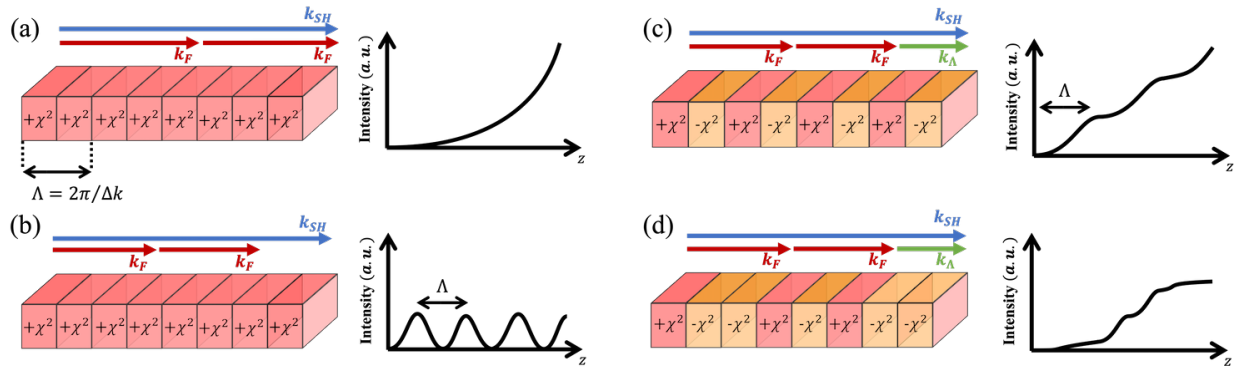

Figure 2.2 Effect of phase matching on SHG output intensity. (a) Perfect phase matching in a bulk crystal results in rapid intensity growth. (b) Imperfect phase matching causes intensity oscillations. (c) Quasi-phase matching in a periodically poled crystal enhances intensity growth. (d) Aperiodic poling allows fine control over intensity evolution.

Types of Phase Matching for SHG

Phase matching in SHG occurs in three configurations based on the polarizations of the interacting fields: Type 0, Type I, and Type II.

- **Type 0:** Both the fundamental and second harmonic fields share the same polarization, maximizing the nonlinear coefficient and conversion efficiency. However, achieving

phase matching in this configuration is more difficult due to strong dispersion.

- **Type I:** The fundamental field has a polarization orthogonal to that of the second harmonic field, typically with both photons of the fundamental wave polarized in the same direction. This configuration offers a good balance between efficiency and phase matching ease.

- **Type II:** The two photons of the fundamental wave have orthogonal polarizations, while the second harmonic wave has a polarization that is either ordinary or extraordinary. Type II provides more flexible phase matching conditions, especially in birefringent materials, but usually with lower conversion efficiency.

2.2.2 Nonlinear Coupled Mode Wave Equation for SHG

In the context of ultrashort pulses, such as those from soliton mode-locked lasers, the SHG process involves the interaction of multiple frequency components due to the broad spectral bandwidth. This broad spectrum leads to a combination of SHG and SFG processes. This section derives the nonlinear coupled mode wave equations that describe these interactions, offering a comprehensive framework for understanding SHG in PPLN crystals.

General Formulation of the Nonlinear Coupled Mode Equations

By applying the SVEA to each frequency component and assuming an ω-dependent carrier [22], $E(\mathbf{r},\omega) = e^{ik(\omega)z}A(\mathbf{r},\omega)$, and inserting it into Maxwell's equations, the coupled mode equations for the fundamental and second harmonic fields can be expressed as [23]:

$$\begin{aligned} i\frac{\partial A_{\mathrm{F}}(\mathbf{r},\omega)}{\partial z} &+ \frac{\nabla_T^2}{2k_{\mathrm{F}}(\omega)}A_{\mathrm{F}}(\mathbf{r},\omega) \\ &= -\frac{\omega^2}{c^2 k_{\mathrm{F}}(\omega)}\,\chi^{(2)}(z)\int \mathrm{d}\omega' \kappa_{\mathrm{F}}(\omega,\omega')e^{-i\Delta k(\omega,\omega')}A_{\mathrm{SH}}(\mathbf{r},\omega+\omega')A_{\mathrm{F}}^*(\mathbf{r},\omega'), \\ i\frac{\partial A_{\mathrm{SH}}(\mathbf{r},\omega)}{\partial z} &+ \frac{\nabla_T^2}{2k_{\mathrm{SH}}(\omega)}A_{\mathrm{SH}}(\mathbf{r},\omega) \\ &= -\frac{\omega^2}{c^2 k_{\mathrm{SH}}(\omega)}\,\chi^{(2)}(z)\int \mathrm{d}\omega' \kappa_{\mathrm{SH}}(\omega,\omega')e^{i\Delta k(\omega,\omega')}A_{\mathrm{F}}(\mathbf{r},\omega-\omega')A_{\mathrm{F}}(\mathbf{r},\omega'), \end{aligned} \tag{2.33}$$

where $A_{\mathrm{F}}(\mathbf{r},\omega)$ and $A_{\mathrm{SH}}(\mathbf{r},\omega)$ are the slowly varying amplitudes of the fundamental and second harmonic fields, $k_{\mathrm{F}}(\omega)$ and $k_{\mathrm{SH}}(\omega)$ are the corresponding wavenumbers, and $\Delta k(\omega,\omega') = k_{\mathrm{F}}(\omega) + k_{\mathrm{F}}(\omega') - k_{\mathrm{SH}}(\omega+\omega')$ denotes the phase mismatch.

The efficiency of the nonlinear interaction is further quantified by the overlap integrals $\kappa_{\mathrm{F}}(\omega,\omega')$ and $\kappa_{\mathrm{SH}}(\omega,\omega')$, defined as:

$$\begin{aligned}\kappa_{\mathrm{F}}(\omega,\omega') &= \frac{\int \mathrm{d}\mathbf{r} A_{\mathrm{F}}^*(\mathbf{r},\omega) A_{\mathrm{SH}}(\mathbf{r},\omega+\omega') A_{\mathrm{F}}^*(\mathbf{r},\omega')}{\int \mathrm{d}\mathbf{r} A_{\mathrm{F}}^*(\mathbf{r},\omega) A_{\mathrm{F}}(\mathbf{r},\omega)},\\ \kappa_{\mathrm{SH}}(\omega,\omega') &= \frac{\int \mathrm{d}\mathbf{r} A_{\mathrm{SH}}^*(\mathbf{r},\omega) A_{\mathrm{F}}(\mathbf{r},\omega+\omega') A_{\mathrm{F}}(\mathbf{r},\omega')}{\int \mathrm{d}\mathbf{r} A_{\mathrm{SH}}^*(\mathbf{r},\omega) A_{\mathrm{SH}}(\mathbf{r},\omega)}.\end{aligned} \tag{2.34}$$

Simplified Solution Under Perfect Phase Matching

To better understand the SHG process, a simplified case in a PPLN crystal, as developed in [23], is considered. In this scenario, the nonlinear susceptibility periodically changes sign along the propagation direction with a poling period Λ, as described by (2.32). The spatial variation of the nonlinear coefficient $d(z)$ can be expressed as a Fourier series:

$$d(z) = d_{\mathrm{eff}} \sum_m G_m e^{ik_m z}, \tag{2.35}$$

where $d_{\mathrm{eff}} = \frac{2}{\pi}\chi^{(2)}$ is the effective nonlinear coefficient, $k_m = 2\pi m/\Lambda$ represents the wavevector for the m-th harmonic, and $G_m = \frac{2}{m\pi}\sin(m\pi/2)$ are the Fourier coefficients.

Simplifying further, transverse distribution is neglected, the pump is assumed to be monochromatic with frequency ω, and only the term where k_m is closest to Δk is considered. Under these assumptions, the coupled mode equations for the fundamental and second harmonic fields simplify to:

$$\begin{aligned}\frac{\partial A_{\mathrm{F}}(z)}{\partial z} &= i\frac{\omega^2 d_{\mathrm{eff}}}{c^2 k_{\mathrm{F}}} A_{\mathrm{SH}}(z) A_{\mathrm{F}}^*(z) e^{-i(\Delta k - k_m)z},\\ \frac{\partial A_{\mathrm{SH}}(z)}{\partial z} &= i\frac{\omega^2 d_{\mathrm{eff}}}{c^2 k_{\mathrm{SH}}} A_{\mathrm{F}}^2(z) e^{i(\Delta k - k_m)z}.\end{aligned} \tag{2.36}$$

Two distinct solutions arise from these simplified equations:

1. **Low Conversion Approximation:** For small energy conversion, where the amplitude of the fundamental wave remains nearly constant ($A_{\mathrm{F}}(0) = A_{\mathrm{F}}(z)$) and the second harmonic initially has no energy ($A_{\mathrm{SH}}(0) = 0$), the solution for the second harmonic field is:
$$|A_{\mathrm{SH}}(z)| = \frac{\omega^2 d_{\mathrm{eff}} z}{c^2 k_{\mathrm{SH}}} |A_{\mathrm{F}}(0)|^2 \mathrm{sinc}\left(\frac{\Delta k z}{2}\right) e^{i\frac{\Delta k z}{2}}. \tag{2.37}$$

2. **High Conversion Approximation (Pump Depletion):** In the case of significant energy conversion, where the fundamental wave experiences depletion ($A_{\mathrm{F}}(0) \neq A_{\mathrm{F}}(z)$), the solutions for the fundamental and second harmonic fields are given by:

$$
\begin{aligned}
|A_{\mathrm{F}}(z)| &= |A_{\mathrm{F}}(0)|\mathrm{sech}\left(\frac{\omega^2 d_{\mathrm{eff}}|A_{\mathrm{F}}(0)|z}{c^2 k_{\mathrm{SH}}}\sqrt{\frac{k_{\mathrm{SH}}}{2k_{\mathrm{F}}}}\right), \\
|A_{\mathrm{SH}}(z)| &= |A_{\mathrm{F}}(0)|\sqrt{\frac{2k_{\mathrm{F}}}{k_{\mathrm{SH}}}}\tanh\left(\frac{\omega^2 d_{\mathrm{eff}}|A_{\mathrm{F}}(0)|z}{c^2 k_{\mathrm{SH}}}\sqrt{\frac{k_{\mathrm{SH}}}{2k_{\mathrm{F}}}}\right).
\end{aligned}
\tag{2.38}
$$

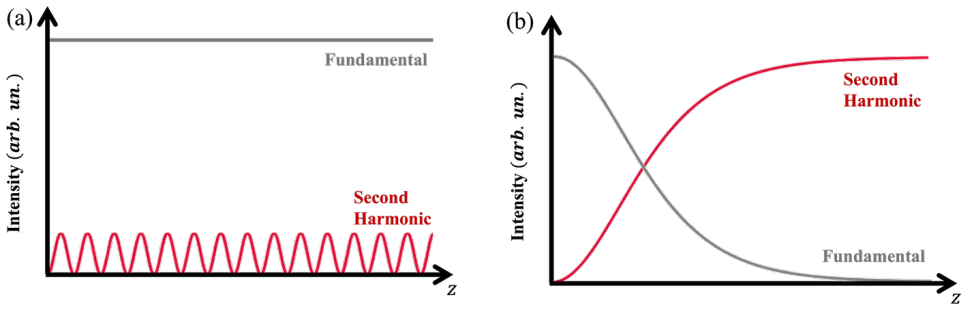

Figure 2.3 Effect of phase matching on SHG output intensity. (a) Solution for imperfect phase matching in the low conversion approximation. (b) Solution in the high conversion approximation.

Figure 2.3 illustrates the dynamics of SHG under varying conditions. In the case of low conversion with imperfect phase matching, the second harmonic field exhibits oscillations with a periodicity determined by the coherence length of the SHG process. Conversely, in the high conversion scenario, where the fundamental wave is significantly depleted, the second harmonic field initially increases rapidly but eventually saturates, following hyperbolic secant and tangent functions. This saturation indicates a reduction in conversion efficiency as the fundamental wave energy is consumed. While these idealized models provide insight into SHG principles, they are limited and do not capture real-world complexities, such as material imperfections, non-ideal phase matching, and the broad spectral bandwidth of ultrashort pulses, all of which can alter SHG efficiency.

This section has established the theoretical framework for understanding the SHG process in PPLN, with particular attention to its behavior under ultrashort pulses. A detailed experimental investigation of SHG in PPLN crystals will follow in Chapter 4. The next section builds on this foundation by introducing the essential concepts of SPDC. Focus will be placed on understanding the entanglement process through SPDC, providing the theoretical basis necessary for optimizing these materials in Chapter 5. The SPDC theory draws primarily

from [24,25] for the SPDC Hamiltonian and first-order perturbation theory, from [22] for the nonlinear coupled mode wave equation, and from [24, 26, 27] for the spectral purity analysis and optimization strategies.

2.3 Theoretical Development of Spontaneous Parametric Down-Conversion

SPDC is a fundamental process in quantum optics for generating entangled photon pairs. During SPDC, a high-energy photon from a pump laser interacts with a second-order nonlinear crystal and splits into two lower-energy photons, known as the signal and idler, while conserving both energy and momentum [24] (see figure 2.4). This process is driven by the nonlinear susceptibility $\chi^{(2)}$ of the crystal and quantum vacuum fluctuations, which initiate the generation of the signal and idler photons. The resulting photon pairs exhibit strong entanglement, leading to non-classical correlations that are valuable for applications in fields such as imaging, quantum cryptography, and quantum computing [2,3].

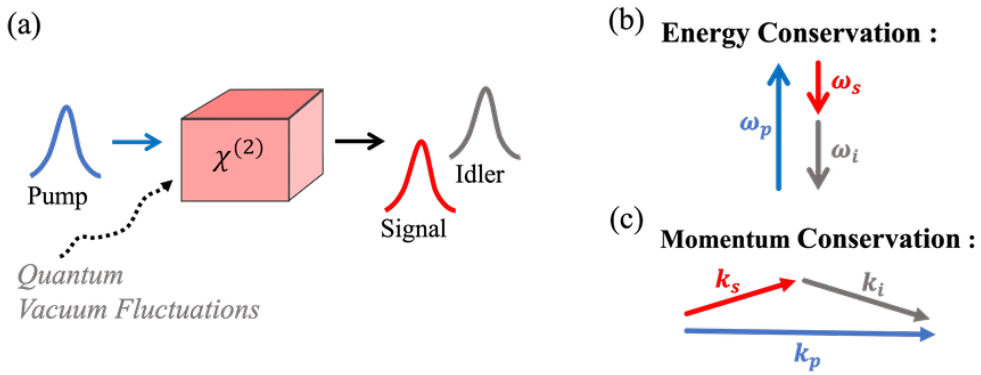

Figure 2.4 (a) Schematic of the SPDC process in a nonlinear crystal. (b) Energy conservation between the pump, signal, and idler photons. (c) Momentum conservation showing the relationship between the wave vectors of the pump, signal, and idler photons.

Phase Matching

As previously explained, the principles of phase matching discussed in section 2.2.1 for SHG can also be applied to SPDC and other second-order nonlinear processes. However, there is a key difference: in SPDC, vacuum fluctuations can take any form, meaning that phase matching can always occur in some mode.

In SPDC, the goal is not simply to minimize the phase mismatch $\Delta\mathbf{k} = \mathbf{k}_{\text{pump}} - \mathbf{k}_{\text{signal}} - \mathbf{k}_{\text{idler}}$, but rather to achieve specific phase matching conditions to generate photons in the desired modes.

QPM is often employed to address phase mismatch issues. In QPM, the poling period Λ is selected to meet the condition:

$$\Lambda = \frac{2\pi}{\Delta \mathbf{k}} \quad \longrightarrow \quad \Delta \mathbf{k}_{\text{QPM}} = \mathbf{k}_{\text{pump}} - \mathbf{k}_{\text{signal}} - \mathbf{k}_{\text{idler}} - \frac{2\pi}{\Lambda}. \tag{2.39}$$

A particularly interesting approach is QPM with aperiodic poling. This method allows for a broader Phase Matching Function (PMF) [28] and can be specifically designed to produce photon pairs with high spectral purity, making it ideal for generating pure entangled photon sources [29].

2.3.1 The SPDC Hamiltonian

Classical Description

To study the SPDC interaction in detail, the Hamiltonian governing this process must be defined. The starting point is the energy of the electromagnetic field system [18, 24, 25]:

$$H(t) = \frac{1}{2} \int \mathrm{d}^3 r \Big(\overrightarrow{B} \cdot \overrightarrow{H} + \overrightarrow{E} \cdot \overrightarrow{D} \Big), \tag{2.40}$$

where $\overrightarrow{H} = \overrightarrow{B}/\mu_0$ for a non-magnetic medium. Substituting the expression for the electric flux density (2.2) yields:

$$H = \underbrace{\frac{1}{2} \int \mathrm{d}^3 r \left(-\frac{1}{\mu_0} B^2 + \epsilon_0 (1 + \chi^{(1)}) E^2 \right)}_{H_{\text{free}}} + \underbrace{\frac{2}{3} \epsilon_0 \int \mathrm{d}^3 r \chi^{(2)} E^3}_{H_{\text{SPDC}}}. \tag{2.41}$$

For simplicity, $\chi^{(1)}$ is assumed to be diagonal, with the coordinate system aligned to the optical axes of the crystal. In the interaction picture, the Hamiltonian is divided into the free part, H_{free}, describing light propagation with a refractive index $n^2 = 1 + \chi^{(1)}$, and the interaction part, H_{SPDC}, representing the nonlinear SPDC process.

The nonlinear interaction is categorized based on the polarizations of the pump, signal, and idler fields:

- **Type-0 SPDC:** All three fields (pump, signal, idler) have the same polarization.
- **Type-I SPDC:** The polarization of the pump field is orthogonal to the polarizations of both the signal and idler fields, which share the same polarization.
- **Type-II SPDC:** The signal and idler fields have orthogonal polarizations.

The phase matching type depends on the polarizations of these fields, determining the specific value of $\chi^{(2)}$. For simplicity, the subscripts on $\chi^{(2)}$ are omitted, assuming it corresponds to the relevant phase matching scenario. Labeling the fields as pump (p), signal (s), and idler (i), the SPDC Hamiltonian is expressed as:

$$H_{\text{SPDC}} = \frac{2}{3}\epsilon_0 \int \mathrm{d}^3 r \chi^{(2)} E_p E_s E_i. \tag{2.42}$$

In this form, $\chi^{(2)}$ encapsulates the interaction dynamics, while E_p, E_s, and E_i represent the electric fields of the pump, signal, and idler photons, respectively.

From Classical to Quantum Description

Transitioning from the classical to the quantum description of the electromagnetic field involves quantizing the electric field modes, treating them as harmonic oscillators with specific commutation relations [24,25]. This quantization allows for a simplified quantum mechanical framework to describe the interaction of light with matter.

In classical electrodynamics, the electric field $\mathbf{E}$ is described as a sum of plane waves, each characterized by a wavevector $\mathbf{k}$ and polarization s. In the quantum framework, the classical amplitudes are replaced by quantum operators, which correspond to the creation and annihilation of photons in each mode.

The electric field operator for a mode with wavevector $\mathbf{k}$ and polarization s is given by [25]:

$$\hat{E}_i(\mathbf{r}, t) = i \sum_{\mathbf{k}} \sqrt{\frac{\hbar \omega_k}{2\epsilon_0 n_{ki} V}} \left(\hat{a}_{\mathbf{k}} \epsilon_{\mathbf{k}i} e^{i(\mathbf{k}\cdot\mathbf{r} - \omega_k t)} - \hat{a}^\dagger_{\mathbf{k}} \epsilon^*_{\mathbf{k}i} e^{-i(\mathbf{k}\cdot\mathbf{r} - \omega_k t)} \right), \tag{2.43}$$

where ω_k is the angular frequency of the mode, V is the mode volume, and $\epsilon_{\mathbf{k}i}$ is a unit polarization vector. The summation index $\mathbf{k} = (\mathbf{k}, s)$ labels the wavevector $\mathbf{k}$ and the polarization $s \in \{1, 2\}$.

The operators $\hat{a}_{\mathbf{k}}$ and $\hat{a}^\dagger_{\mathbf{k}}$ represent the annihilation and creation of photons in the mode $\mathbf{k}$, respectively. These operators obey the commutation relations:

$$[\hat{a}_{\mathbf{k}}, \hat{a}^\dagger_{\mathbf{k}'}] = \delta_{\mathbf{k},\mathbf{k}'}, \quad [\hat{a}_{\mathbf{k}}, \hat{a}_{\mathbf{k}'}] = [\hat{a}^\dagger_{\mathbf{k}}, \hat{a}^\dagger_{\mathbf{k}'}] = 0. \tag{2.44}$$

These commutation relations ensure that the field, when quantized in quasi-monochromatic waves, behaves as a collection of harmonic oscillators, each with its own frequency ω_k. The Hamiltonian for the free electromagnetic field, representing the total energy of all field modes,

is:

$$\hat{H}_{\text{free}} = \sum_{\mathbf{k}} \hbar\omega_k \left(\hat{a}^\dagger_{\mathbf{k}} \hat{a}_{\mathbf{k}} + \frac{1}{2} \right). \tag{2.45}$$

This Hamiltonian indicates that each monochromatic mode contributes an energy $\hbar\omega_k$ for each photon present, plus a zero-point energy $\frac{1}{2}\hbar\omega_k$ due to quantum vacuum fluctuations.

For SPDC, the interaction Hamiltonian is expressed as:

$$\hat{H}_{\text{SPDC}} = \frac{2}{3}\epsilon_0 \int \mathrm{d}^3 r \chi^{(2)} \hat{E}_p \hat{E}_s \hat{E}_i, \tag{2.46}$$

Here, $\hat{E}_p$, $\hat{E}_s$, and $\hat{E}_i$ are the electric field operators for the pump, signal, and idler photons, respectively.

2.3.2 Nonlinear Coupled Mode Wave Equation for SPDC

To derive the nonlinear coupled mode wave equation for the SPDC process, the starting point is the Heisenberg equation of motion in the interaction picture. These equations are used to derive the quantum Maxwell's equations in a medium without charges and currents [30, 31]:

$$\nabla^2 \hat{E}_\alpha(\mathbf{r}, \omega) + \frac{\epsilon(\omega)\omega^2}{c^2} \hat{E}_\alpha(\mathbf{r}, \omega) = -2\mu_0 \epsilon_0 \omega^2 \chi^{(2)}_{\alpha\beta\gamma}(\mathbf{r}) \int d\omega' \hat{E}_\beta(\mathbf{r}, \omega + \omega') \hat{E}^\dagger_\gamma(\mathbf{r}, \omega'), \tag{2.47}$$

where the subscripts α, β, and γ represent the signal, idler, or pump photons.

For each frequency component, the slowly-varying envelope approximation is assumed with an ω-dependent carrier. The electric field $E(\mathbf{r}, t)$ is then decomposed via a Fourier transform:

$$\hat{E}(t, \mathbf{r}) = \int \hat{E}(\omega, \mathbf{r}) e^{i\omega t} d\omega = \int \hat{A}(\mathbf{r}, \omega) e^{ik(\omega)z - \omega t} d\omega, \tag{2.48}$$

where $k(\omega) = \frac{n(\omega)\omega}{c}$ and $n(\omega)$ is the refractive index.

Inserting (2.48) in (2.47), the coupled mode equations for SPDC are derived:

$$
\begin{aligned}
&i\frac{\partial \hat{A}_i(\mathbf{r},\omega)}{\partial z} + \frac{\nabla_T^2}{2k_i(\omega)}\hat{A}_i(\mathbf{r},\omega) \\
&\quad = -\frac{\omega^2}{c^2 k_i(\omega)}\,\chi^{(2)}(z)\int \mathrm{d}\omega' \kappa_i(\omega,\omega') e^{-i\Delta k(\omega,\omega')}\hat{A}_p(\mathbf{r},\omega+\omega')\hat{A}_s^\dagger(\mathbf{r},\omega'), \\
&i\frac{\partial \hat{A}_s(\mathbf{r},\omega)}{\partial z} + \frac{\nabla_T^2}{2k_s(\omega)}\hat{A}_s(\mathbf{r},\omega) \\
&\quad = -\frac{\omega^2}{c^2 k_s(\omega)}\,\chi^{(2)}(z)\int \mathrm{d}\omega' \kappa_s(\omega,\omega') e^{-i\Delta k(\omega,\omega')}\hat{A}_p(\mathbf{r},\omega+\omega')\hat{A}_i^\dagger(\mathbf{r},\omega'), \\
&i\frac{\partial \hat{A}_p(\mathbf{r},\omega)}{\partial z} + \frac{\nabla_T^2}{2k_p(\omega)}\hat{A}_p(\mathbf{r},\omega) \\
&\quad = -\frac{\omega^2}{c^2 k_p(\omega)}\,\chi^{(2)}(z)\int \mathrm{d}\omega' \kappa_p(\omega,\omega') e^{-i\Delta k(\omega,\omega-\omega')}\hat{A}_s(\mathbf{r},\omega-\omega')\hat{A}_i(\mathbf{r},\omega'),
\end{aligned}
\tag{2.49}
$$

where the subscripts i, s, and p correspond to the idler, signal, and pump fields, respectively. $\Delta k(\omega,\omega') = k_s(\omega) + k_i(\omega) - k_p(\omega')$ represents the phase mismatch between the interacting waves.

The overlap integrals κ_i, κ_s, and κ_p are defined as:

$$
\begin{aligned}
\kappa_i(\omega,\omega') &= \frac{\int \mathrm{d}\mathbf{r}\hat{A}_i^\dagger(\mathbf{r},\omega)\hat{A}_p(\mathbf{r},\omega+\omega')\hat{A}_s^\dagger(\mathbf{r},\omega')}{\int \mathrm{d}\mathbf{r}\hat{A}_i^\dagger(\mathbf{r},\omega)\hat{A}_i(\mathbf{r},\omega)}, \\
\kappa_s(\omega,\omega') &= \frac{\int \mathrm{d}\mathbf{r}\hat{A}_s^\dagger(\mathbf{r},\omega)\hat{A}_p(\mathbf{r},\omega+\omega')\hat{A}_i^\dagger(\mathbf{r},\omega')}{\int \mathrm{d}\mathbf{r}\hat{A}_s^\dagger(\mathbf{r},\omega)\hat{A}_s(\mathbf{r},\omega)}, \\
\kappa_p(\omega,\omega') &= \frac{\int \mathrm{d}\mathbf{r}\hat{A}_p^\dagger(\mathbf{r},\omega)\hat{A}_s(\mathbf{r},\omega-\omega')\hat{A}_i(\mathbf{r},\omega')}{\int \mathrm{d}\mathbf{r}\hat{A}_p^\dagger(\mathbf{r},\omega)\hat{A}_p(\mathbf{r},\omega)}.
\end{aligned}
\tag{2.50}
$$

These integrals account for the spatial overlap of the interacting fields, playing a crucial role in determining the efficiency of the nonlinear interaction.

To solve these coupled-mode equations numerically, the pump field is treated as a classical amplitude due to its much stronger intensity relative to the signal and idler fields, i.e., $\hat{A}_p(\mathbf{r},\omega) \to \mathcal{A}_p(\mathbf{r},\omega)$. Additionally, the Heisenberg equations are multiplied by the output

state $\langle\psi|$ from the left and the initial vacuum state $|0\rangle$ from the right [22]:

$$\begin{aligned}
&i\frac{\partial\mathcal{A}_i^{(\mathrm{out})}(\mathbf{r},\omega)}{\partial z}+\frac{\nabla_T^2}{2k_i(\omega)}\mathcal{A}_i^{(\mathrm{out})}(\mathbf{r},\omega)\\
&\quad=-\frac{\omega^2}{c^2k_i(\omega)}\,\chi^{(2)}(z)\int \mathrm{d}\omega'\kappa_i(\omega,\omega')e^{-i\Delta k(\omega,\omega')}\mathcal{A}_p(\mathbf{r},\omega+\omega')\mathcal{A}_s^{(\mathrm{vac})*}(\mathbf{r},\omega'),\\
&i\frac{\partial\mathcal{A}_s^{(\mathrm{out})}(\mathbf{r},\omega)}{\partial z}+\frac{\nabla_T^2}{2k_s(\omega)}\mathcal{A}_s^{(\mathrm{out})}(\mathbf{r},\omega)\\
&\quad=-\frac{\omega^2}{c^2k_s(\omega)}\,\chi^{(2)}(z)\int \mathrm{d}\omega'\kappa_s(\omega,\omega')e^{-i\Delta k(\omega,\omega')}\mathcal{A}_p(\mathbf{r},\omega+\omega')\mathcal{A}_i^{(\mathrm{vac})*}(\mathbf{r},\omega'),\\
&i\frac{\partial\mathcal{A}_p(\mathbf{r},\omega)}{\partial z}+\frac{\nabla_T^2}{2k_p(\omega)}\mathcal{A}_p(\mathbf{r},\omega)\\
&\quad=-\frac{\omega^2}{c^2k_p(\omega)}\,\chi^{(2)}(z)\int \mathrm{d}\omega'\kappa_p(\omega,\omega')e^{-i\Delta k(\omega,\omega-\omega')}\mathcal{A}_s^{(\mathrm{out})}(\mathbf{r},\omega-\omega')\mathcal{A}_i^{(\mathrm{out})}(\mathbf{r},\omega'),
\end{aligned}\tag{2.51}$$

where the output field amplitude $\mathcal{A}_\alpha^{(\mathrm{out})}=\langle\psi|\hat{A}_\alpha|0\rangle$ and the vacuum field amplitude $\mathcal{A}_\alpha^{(\mathrm{vac})*}=\langle 0|\hat{A}_\alpha|\psi\rangle$ are defined. The dynamics of the vacuum amplitudes require an additional set of coupled equations for the vacuum fields:

$$\begin{aligned}
&i\frac{\partial\mathcal{A}_i^{(\mathrm{vac})}(\mathbf{r},\omega)}{\partial z}+\frac{\nabla_T^2}{2k_i(\omega)}\mathcal{A}_i^{(\mathrm{vac})}(\mathbf{r},\omega)\\
&\quad=-\frac{\omega^2}{c^2k_i(\omega)}\,\chi^{(2)}(z)\int \mathrm{d}\omega'\kappa_i(\omega,\omega')e^{-i\Delta k(\omega,\omega')}\mathcal{A}_p(\mathbf{r},\omega+\omega')\mathcal{A}_s^{(\mathrm{out})*}(\mathbf{r},\omega'),\\
&i\frac{\partial\mathcal{A}_s^{(\mathrm{vac})}(\mathbf{r},\omega)}{\partial z}+\frac{\nabla_T^2}{2k_s(\omega)}\mathcal{A}_s^{(\mathrm{vac})}(\mathbf{r},\omega)\\
&\quad=-\frac{\omega^2}{c^2k_s(\omega)}\,\chi^{(2)}(z)\int \mathrm{d}\omega'\kappa_s(\omega,\omega')e^{-i\Delta k(\omega,\omega')}\mathcal{A}_p(\mathbf{r},\omega+\omega')\mathcal{A}_i^{(\mathrm{out})*}(\mathbf{r},\omega'),
\end{aligned}\tag{2.52}$$

The coupled equations (2.51) and (2.52) can be solved under the following initial and boundary conditions at $z=0$:

$$\begin{aligned}
&\mathcal{A}_p=\textit{initial pump},\\
&\mathcal{A}_s^{(\mathrm{out})}=\mathcal{A}_i^{(\mathrm{out})}=0,\\
&\mathcal{A}_s^{(\mathrm{vac})}=\mathcal{A}_i^{(\mathrm{vac})}=\textit{vacuum fluctuations noise}.
\end{aligned}\tag{2.53}$$

2.3.3 First-Order Time-Dependent Perturbation Theory

In the previous section, the nonlinear coupled equations offered a detailed yet complex description of the interaction between the pump, signal, and idler fields within the crystal.

First-order perturbation theory simplifies this by treating the nonlinear interaction as a small perturbation to the initial state of the system. This approach is particularly advantageous for describing SPDC, where the focus is on first-order effects, especially under weak nonlinear conditions. A key concept in this framework is the PMF, which captures the momentum conservation in the second-order nonlinear material. The PMF notably plays a crucial role in determining the spectral properties of the generated photon pairs. By employing first-order perturbation theory, one can also easily calculate the Joint Spectral Amplitude (JSA), offering a simpler understanding of the photon pair correlations.

Parametric Down-Conversion (PDC) State with First-Order Perturbation

To simplify the analysis, assume collinear propagation of the fields along the z-axis of a crystal with length L. The expression in (2.48) is decomposed to separate the transverse and longitudinal distributions:

$$\begin{aligned}\hat{E}(t,\mathbf{r}) &= \int_{-\infty}^{\infty} \hat{A}(z,\omega)F(x,y)e^{ik(\omega)z-\omega t}d\omega \\ &= i\int d\omega\sqrt{\frac{\hbar\omega_0}{4\pi c\epsilon_0 n(\omega_0)}}\left(F_i(x,y)\hat{a}_i(\omega)e^{i(k(\omega)z-\omega t)} - F_i^*(x,y)\hat{a}_i^\dagger(\omega)e^{-i(k(\omega)z-\omega t)}\right),\end{aligned} \tag{2.54}$$

where $\hat{A}(z,\omega)$ is the slowly-varying amplitude along the z-axis, and $F(x,y)$ is the normalized transverse profile. The approximation $\omega \approx \omega_0$ in the first factor corresponds to the rotating wave approximation. For a collimated Gaussian beam in a bulk crystal, $F(x,y)$ is a Gaussian distribution. In the case of a single-mode waveguide, $F(x,y)$ represents the mode profile of the waveguide.

The evolution of the SPDC state is then studied starting from the Schrödinger equation:

$$\hbar\frac{\mathrm{d}}{\mathrm{d}t}|\psi(t)\rangle = \hat{H}_I(t)|\psi(t)\rangle \tag{2.55}$$

The quantum state of the SPDC output at time t is given by:

$$|\psi(t)\rangle_{\mathrm{SPDC}} = \mathcal{T}\exp\left(-\frac{i}{\hbar}\int_0^t \mathrm{d}t'\hat{H}_I(t')\right)|0\rangle \approx \exp\left(-\frac{i}{\hbar}\int_{-\infty}^{\infty}\mathrm{d}t\hat{H}_I(t)\right)|0\rangle, \tag{2.56}$$

where $|0\rangle = |0\rangle_s|0\rangle_i$ is the initial vacuum state. The time-ordering operator $\mathcal{T}$ is necessary because $\hat{H}_I(t)$ varies with time, leading to non-commutativity at different times and resulting in complex effects. In the low pump-power regime, these effects are minimal and can be disregarded [24]. However, at higher pump powers, this assumption may introduce inaccuracies.

The SPDC state is developed by performing a perturbation expansion:

$$\begin{aligned}|\psi(t)\rangle_{\text{SPDC}} = \underbrace{|0\rangle}_{\textbf{vacuum}} &- \underbrace{\frac{i}{\hbar}\int_0^t dt' \hat{H}_{\text{SPDC}}(t')|0\rangle}_{\textbf{photon-pair emission}} \\ &+ \underbrace{\left(\frac{i}{\hbar}\right)^2 \int_0^t dt' \hat{H}_{\text{SPDC}}(t') \int_0^{t'} dt'' \hat{H}_{\text{SPDC}}(t'')|0\rangle}_{\textbf{four-photon emission}} + \underbrace{\cdots}_{\textbf{higher-order photon pairs}}\end{aligned} \tag{2.57}$$

The zero-order term represents vacuum emission, the first-order term describes photon-pair emission, the second-order term corresponds to four-photon emission, and so on. As long as the incoming pump field is not too intense, the emission of higher-order photon pairs can be safely ignored due to the low probability of generating multiple pairs.

The first-order perturbation description of the SPDC state thus involves retaining only the terms up to photon-pair emission. By substituting the definition of the Hamiltonian (2.46) and using the field decomposition from (2.54), the photon-pair emission term is obtained as:

$$\begin{aligned}\int_0^t dt' \hat{H}_{\text{SPDC}} = \mathcal{B}\int_0^t dt' \int_{-\frac{L}{2}}^{\frac{L}{2}} dz \int\int\int d\omega_p\, d\omega_s\, d\omega_i \Bigg[\\ O_{\text{None}} \exp\left\{i\left[k_p(\omega_p) + k_s(\omega_s) + k_i(\omega_i)\right] z - i(\omega_p + \omega_s + \omega_i)t\right\} \hat{a}_p(\omega_p)\hat{a}_s(\omega_s)\hat{a}_i(\omega_i) \\ + O_{\text{SFG}} \exp\left\{i\left[k_p(\omega_p) + k_s(\omega_s) - k_i(\omega_i)\right] z - i(\omega_p + \omega_s - \omega_i)t\right\} \hat{a}_p(\omega_p)\hat{a}_s(\omega_s)\hat{a}_i^\dagger(\omega_i) \\ + O_{\text{DFG}} \exp\left\{i\left[k_p(\omega_p) - k_s(\omega_s) + k_i(\omega_i)\right] z - i(\omega_p - \omega_s + \omega_i)t\right\} \hat{a}_p(\omega_p)\hat{a}_s^\dagger(\omega_s)\hat{a}_i(\omega_i) \\ + O_{\text{SPDC}} \exp\left\{i\left[k_p(\omega_p) - k_s(\omega_s) - k_i(\omega_i)\right] z - i(\omega_p - \omega_s - \omega_i)t\right\} \hat{a}_p(\omega_p)\hat{a}_s^\dagger(\omega_s)\hat{a}_i^\dagger(\omega_i) \\ - \text{h.c.}\Bigg]\end{aligned} \tag{2.58}$$

where the constants are encapsulated in $\mathcal{B}$, and the overlap function of the transverse distributions is in O_i:

$$\mathcal{B} = \frac{\chi^{(2)}}{2}\sqrt{\frac{\hbar\omega_{p0}\omega_{s0}\omega_{i0}}{\epsilon_0\pi^3c^3n_p(\omega_p 0)n_s(\omega_s 0)n_i(\omega_i 0)}}, \quad O_{\text{SPDC}} = \int dxdy F_p(x,y)F_s^*(x,y)F_i^*(x,y) \tag{2.59}$$

The different terms in (2.58) represent various second-order nonlinear processes. The second, third, and fourth terms correspond to sum-frequency generation, difference-frequency generation, and parametric down-conversion, respectively. The first term, due to the energy conservation condition $\omega_p + \omega_s + \omega_i = 0$ being unphysical, can be ignored. Additionally, it is assumed that energy and momentum conservation are satisfied only for the last term,

allowing the other two to be discarded. This approximation is valid if the phase-matching conditions are adequately met experimentally.

Several simplifications can then be made:

- **Z-integration:** The z integration yields the phase-matching function of the crystal:

$$\Phi(\omega_s, \omega_i) = \text{sinc}\left[\Delta k(\omega_s, \omega_i)\frac{L}{2}\right], \tag{2.60}$$

  where the phase-mismatch function is $\Delta k(\omega_s, \omega_i) = k_p(\omega_s + \omega_i) - k_s(\omega_s) - k_i(\omega_i)$. The integration is performed from $-\frac{L}{2}$ to $\frac{L}{2}$.

- **Time-integration:** Extending the time integration bounds to $\pm\infty$, justified by considering the state before and after the crystal interaction, yields a delta function $2\pi\delta(\omega_p - \omega_s - \omega_i)$, allowing for integration over the pump frequencies ω_p.

- **Classical pump approximation:** Given the weak nonlinear interaction, the incoming pump field must be relatively strong and can be treated as a classical field: $\hat{a}_p(\omega_p) \to \alpha(\omega_p)$, where $\alpha(\omega_p)$ represents the pump spectrum amplitude.

Considering all these factors, the final SPDC state after propagating through a crystal of length L is:

$$\begin{aligned} |\psi\rangle_{\text{SPDC}} &= e^{\{2\pi\mathcal{B}O_{\text{SPDC}}\int\int d\omega_s d\omega_i L\Phi(\omega_s,\omega_i)\alpha(\omega_s+\omega_i)\hat{a}_s^\dagger(\omega_s)\hat{a}_i^\dagger(\omega_i) - \text{h.c.}\}}|0\rangle \\ &\approx |0\rangle + \left[2\pi\mathcal{B}O_{\text{SPDC}}\int\int d\omega_s d\omega_i L \underbrace{\Phi(\omega_s,\omega_i)\alpha(\omega_s+\omega_i)}_{f(\omega_s,\omega_i)}\hat{a}_s^\dagger(\omega_s)\hat{a}_i^\dagger(\omega_i) - \text{h.c.}\right]|0\rangle, \end{aligned} \tag{2.61}$$

where the JSA $f(\omega_s, \omega_i)$ is defined, characterizing the spectral correlations of the photon pairs. In first-order perturbation theory, the JSA is the product of the pump distribution $\alpha(\omega_s + \omega_i)$, representing energy conservation in the process, and the phase-matching function $\Phi(\omega_s, \omega_i)$ of the crystal, representing momentum conservation.

Spectral Purity

In the context of SPDC, spectral purity refers to the extent to which the generated photon pairs are confined to a single spectral mode. High spectral purity is crucial for various quantum information applications, such as quantum cryptography and quantum computing, where indistinguishability of photons is essential.

The purity of the entangled state generated in SPDC can be analyzed using the Schmidt decomposition of the JSA function $f(\omega_s, \omega_i)$:

$$f(\omega_s, \omega_i) = F \sum_k \lambda_k \phi_k(\omega_s) \psi_k(\omega_i), \tag{2.62}$$

where λ_k are the normalized eigenvalues $\sum_k |\lambda_k|^2 = 1$, and $\phi_k(\omega_s)$ and $\psi_k(\omega_i)$ are the corresponding eigenfunctions for the signal and idler photons. $F = \sqrt{\int d\omega_s d\omega_i f(\omega_s, \omega_i) f^*(\omega_s, \omega_i)}$ is a normalization constant. Using this decomposition, the broadband frequency modes $\hat{A}_k^\dagger$ and $\hat{B}_k^\dagger$ can be defined as:

$$\begin{aligned} \hat{A}_k^\dagger &= \int d\omega_s \, \phi_k(\omega_s) \hat{a}_s^\dagger(\omega_s), \\ \hat{B}_k^\dagger &= \int d\omega_t \, \psi_k(\omega_t) \hat{a}_t^\dagger(\omega_t), \end{aligned} \tag{2.63}$$

such that the SPDC state becomes:

$$\begin{aligned} |\psi\rangle_{\text{SPDC}} &= e^{\left\{B' \sum_k (\lambda_k \hat{A}_k^\dagger \hat{B}_k^\dagger - \lambda_k^* \hat{A}_k \hat{B}_k)\right\}} |0\rangle \\ &= \bigotimes_k \hat{S}_k(\zeta_k) |0\rangle \\ &\approx |0\rangle + B' \sum_k (\lambda_k \hat{A}_k^\dagger \hat{B}_k^\dagger - \lambda_k^* \hat{A}_k \hat{B}_k) |0\rangle, \end{aligned} \tag{2.64}$$

The squeezing operator is defined as $\hat{S}_k(\zeta_k) = e^{\left\{-\zeta_k \hat{A}_k^\dagger \hat{B}_k^\dagger + \zeta_k^* \hat{A}_k \hat{B}_k\right\}}$, where $\zeta_k = -B'\lambda_k$ and $B' = 4BO_{\text{SPDC}}\alpha_0 FL$. In the SPDC process, photon pairs with a specific JSA are emitted into a superposition of broadband frequency modes, $\hat{A}_{\mathbf{k}}^\dagger$ and $\hat{B}_{\mathbf{k}}^\dagger$. The detection of a photon in mode $\hat{B}_{\mathbf{k}}^\dagger$ ensures its partner is in mode $\hat{A}_{\mathbf{k}}^\dagger$, and vice versa.

For example, a Single-Photon Avalanche Diode (SPAD) with detection efficiency η detecting the idler photon can herald the presence of its partner, the signal photon [24]. This can be described by the observable $\hat{\pi}_1$ characterizing the case where a "click" has occurred on the detector for the idler, and the observable $\hat{\pi}_0$ if "no click" has occurred:

$$\begin{aligned} \hat{\pi}_1 &= \eta \sum_k |\phi_k(\omega_s), 1\rangle\langle\phi_k(\omega_s), 1|, \\ \hat{\pi}_0 &= \sum_k |\phi_k(\omega_s), 0\rangle\langle\phi_k(\omega_s), 0|. \end{aligned} \tag{2.65}$$

The signal state after a "click" detection event becomes:

$$\rho_s = \eta \sum_k |\lambda_k|^2 |\phi_k(\omega_s), 1\rangle\langle\phi_k(\omega_s), 1|. \tag{2.66}$$

This derivation gives a deep understanding of the purity of the state. After the detection process, the heralded signal state is projected into a statistical mixture of broadband states with probability $\eta|\lambda_k|^2$. However, if the JSA presents circular symmetry, it is separable $f(\omega_s, \omega_i) = f(\omega_s) \cdot f(\omega_i)$, and the sum in (2.62) only has one non-zero term. The signal photon will then be heralded in a pure state $|\psi\rangle_s\langle\psi|_s$. Hence, spectral purity for SPDC means the generated photons are confined to a single spectral mode.

The purity of the state can be characterized using various metrics, with one of the most commonly used being the cooperativity K defined as:

$$K = \frac{1}{\sum_k |\lambda_k|^4} = \frac{1}{g^{(2)} - 1}, \tag{2.67}$$

where $g^{(2)}$ corresponds to the unheralded second-order auto-correlation function of the SPDC state. This relation between $g^{(2)}$ and K is only valid in the low gain regime and becomes more complex otherwise. For an ideal pure state, $K = 1$ ($g^{(2)} = 2$), and values $K \gg 1$ ($g^{(2)} \to 1$) indicate the presence of many modes and lower purity.

When employing a CW pump laser, the JSA is given by $f(\omega_s, \omega_i) = E_p\delta(\omega_s+\omega_i-\omega_p)\Phi(\omega_s, \omega_i)$, resulting in a diagonal yet non-separable distribution. Consequently, generating photon pairs in a singular frequency mode using a CW laser is unattainable. In contrast, pulsed lasers can facilitate the production of pure states in SPDC.

2.3.4 Optimizing Spectral Purity in SPDC

In SPDC, the JSA, depending on the PMF and pump envelope, is critical for determining the spectral correlations between signal and idler photons.

The PMF depends on the phase-matching conditions within the nonlinear crystal, influenced by factors such as dispersion, poling period, crystal temperature, and crystal length. The pump envelope is dictated by the temporal profile of the pump pulse, often Gaussian.

Achieving high spectral purity in SPDC involves shaping the JSA so that the detection of the heralding photon does not affect the state of the signal photon. As seen previously, this requires the JSA to be factorable. Factorability is often achieved by aligning the PMF and pump envelope in both shape and bandwidth. Various methods can be used to achieve this, including spectral filtering, group velocity matching, aperiodic poling, or a combination of these techniques.

Spectral Filtering

One straightforward approach to improve spectral purity is spectral filtering of the SPDC output [24]. By applying narrowband filters to the signal, idler, or both, the bandwidth and correlations in the JSA can be reduced. However, while this method is simple and easy to implement, it causes significant photon loss, as filtering removes large portions of the spectrum, reducing the overall brightness of the source.

Group Velocity Matching

A more effective method for enhancing spectral purity in SPDC is through group velocity matching [26, 27]. This involves engineering the crystal so that the group velocities of the interacting fields are aligned. Two primary approaches can be used: asymmetric and symmetric group velocity matching (see figure 2.5).

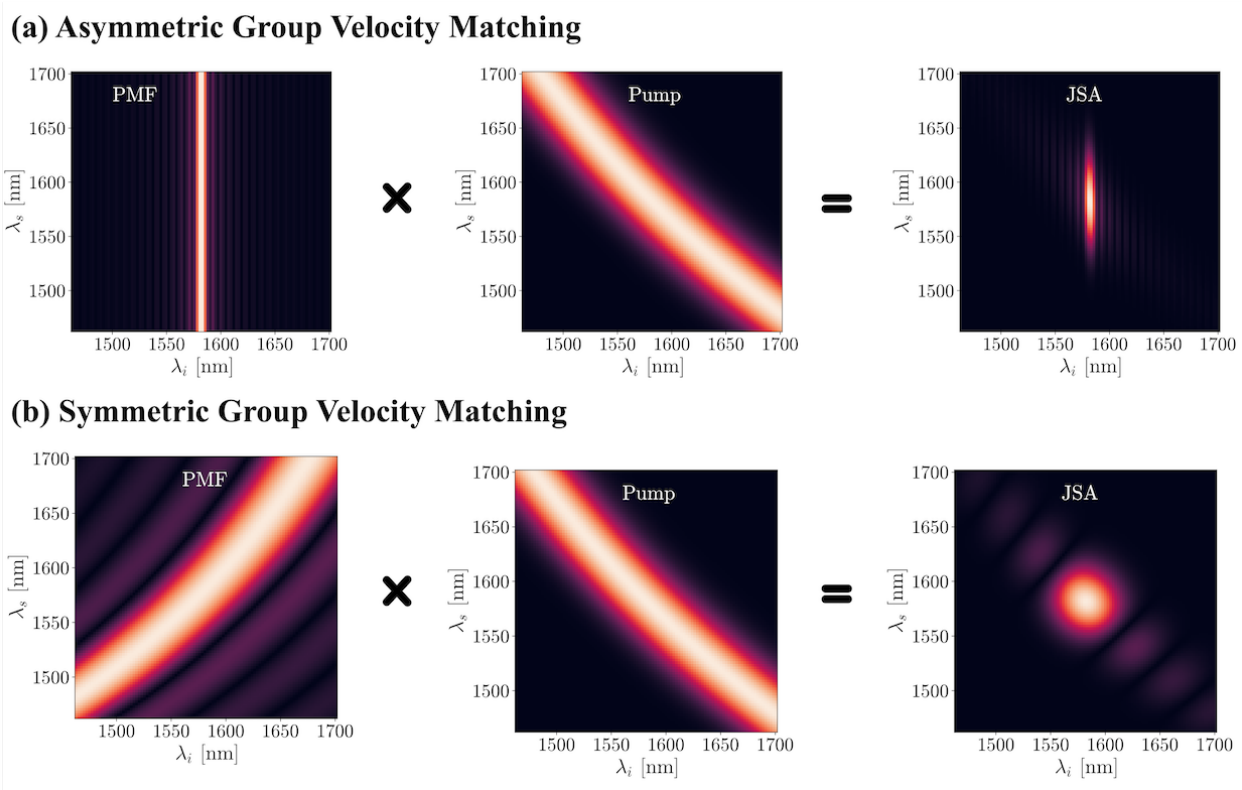

Figure 2.5 Comparison of asymmetric (a) and symmetric (b) group velocity matching regimes and their impact on the JSA.

Group velocity, v_g, is defined as:

$$v_g = \left(\frac{d\beta}{d\omega}\right)^{-1}, \tag{2.68}$$

where β is the propagation constant. Ideally, the group velocities of the pump, signal, and idler waves should be matched, ensuring that the signal and idler photons generated at different points in the crystal maintain a well-defined phase relationship.

Expanding the phase-matching condition around the central frequencies and considering first-order terms, the Group Velocity Mismatch (GVM) is given by:

$$\Delta v_g = \frac{1}{v_{g,p}} - \frac{1}{v_{g,s}} - \frac{1}{v_{g,i}}. \tag{2.69}$$

Perfect group velocity matching occurs when $\Delta v_g = 0$, maximizing interaction efficiency. However, achieving perfect matching in practice is challenging.

This leads to two main regimes:

1. **Asymmetric Group Velocity Matching:** This involves engineering the crystal so that the group velocity of either the signal or idler photon matches that of the pump:

   $$v_{g,s} \text{ or } v_{g,i} = v_{g,p}. \tag{2.70}$$

   This broadens the interaction time between the pump and one of the down-converted photons, narrowing the corresponding spectral bandwidth and resulting in a vertical PMF, leading to a separable, asymmetric JSA, as shown in Figure 2.5(a).

2. **Symmetric Group Velocity Matching:** In this case, the crystal is engineered so that the group velocities of both signal and idler photons are symmetrically matched with the pump:

   $$v_{g,p} = \frac{v_{g,s} + v_{g,i}}{2}. \tag{2.71}$$

   This results in an elongated PMF along the diagonal, orthogonal to the pump envelope, minimizing spectral correlations, as illustrated in Figure 2.5(b).

Asymmetric group velocity matching offers high spectral purity with minimal photon loss but is sensitive to frequency variations and crystal parameter changes. In contrast, symmetric matching is more stable and reliable, with minimal alignment issues, though it requires more complex crystal engineering. In this work, symmetric matching is chosen for its ability to generate broadband, bright, and pure SPDC states.

Symmetric Group Velocity Matching with Aperiodic Poling

To further enhance spectral purity, symmetric group velocity matching can be combined with aperiodic poling. Aperiodic poling involves varying the poling period of the crystal along its length to shape the PMF more precisely, eliminating typical sidelobes of the sinc function and enhancing the purity of the generated photon pairs, as shown in Figure 2.6.

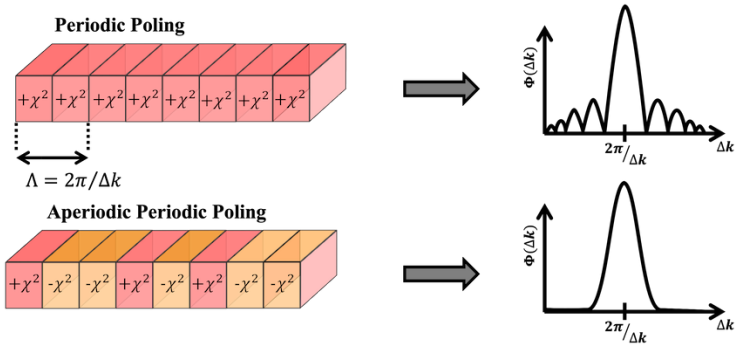

Figure 2.6 Impact of aperiodic poling on the PMF, enhancing spectral purity.

This chapter presented an overview of the SPDC process, with a focus on phase matching and advanced techniques such as quasi-phase matching and aperiodic poling. These concepts form the foundation for the algorithm introduced in Chapter 5, which is designed to optimize second-order nonlinear materials for generating pure entangled states.

CHAPTER 3 ULTRAFAST FIBER LASER SYSTEM

To meet the requirements for a source of entangled photons, the choice of the pump laser is critical. In this work, a custom, low-noise, ultrafast fiber laser system has been designed as the pump. This choice offers several advantages over a CW source:

1. **Enhanced Brightness:** Although the average power may be relatively low, the short pulse duration (typically on the order of a few hundred femtoseconds) allows for high peak powers. These high peak powers enhance the efficiency of nonlinear conversion processes, leading to a brighter source of spontaneous parametric down-conversion with high photon flux.

2. **Broadband Phase Matching:** The broad spectral bandwidth of ultrafast laser pulses enables phase matching over a wide range of wavelengths in nonlinear crystals such as periodically poled lithium niobate. This is beneficial for generating broadband entangled photon pairs.

3. **Low Noise:** The pulsed laser exhibits low noise characteristics, ensuring that the generated SPDC photon pairs possess a high signal-to-noise ratio. This is crucial for high-fidelity quantum experiments, where background noise can severely degrade the quality of entangled photon pairs. Low relative intensity noise helps maintaining the coherence and purity of the quantum states generated through SPDC.

4. **Purity:** As discussed in Section 2.3.3, generating photon pairs in a single frequency mode using a CW laser is not achievable. In contrast, pulsed lasers are more effective at enabling the production of pure quantum states in spontaneous parametric down-conversion processes.

Compared to CW lasers, pulsed lasers offer superior temporal and spectral control, which is essential for efficient and effective entangled pair generation. These properties make them more suitable for advanced quantum optics experiments.

This chapter describes the laser specifically designed for this project, which is primarily based on the methodologies developed in previous projects at Polytechnique Montréal. It incorporates Alexis Labranche's design approaches [1] and Laurent Rivard's advanced fiber splicing techniques [15]. The laser is composed of two main parts: the *Master Oscillator* (MO), operating on the principle of mode-locking as discussed in section 2.1.4, generates

optical solitons which are then amplified and spectrally broadened in the *Erbium-Doped Fiber Amplifier* (EDFA).

3.1 Master Oscillator

This section details the Master Oscillator setup and evaluates its performance across both first and second-order soliton regimes. The system ensures stable operation over a variety of pulse energies and durations. Specifically, in the first-order regime, it produces stable solitons at a central wavelength of approximately 1559 nm with a repetition rate of 60.9 MHz, supporting pulse energies ranging from 30 to 75 pJ and temporal widths from 594 to 312 fs. In addition, the second-order regime maintains stable solitons at a central wavelength of about 1560 nm with a doubled repetition rate of 121.8 MHz, and accommodates pulse energies from 30 to 72 pJ with durations from 380 to 261 fs.

3.1.1 Setup

Figure 3.1 illustrates the configuration of the master oscillator. The laser system is designed using Polarization Maintaining (PM) fibers and components to minimize sensitivity to external perturbations, such as stress-induced variations and temperature fluctuations, which helps reduce spectral and polarization instabilities.

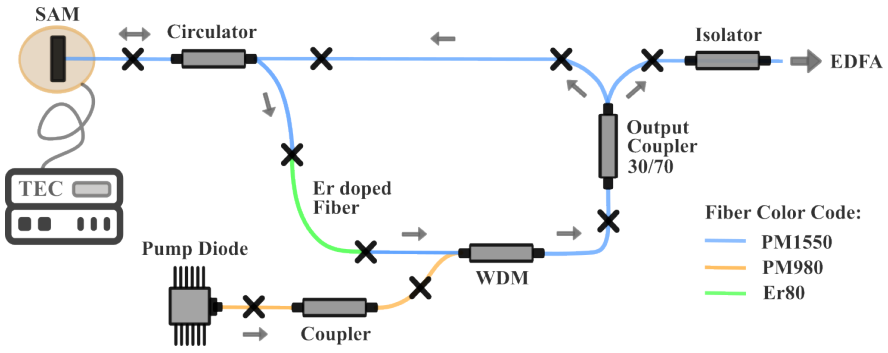

Figure 3.1 Schematic of the mode-locked fiber laser system. Fiber types are differentiated by color codes: blue for PM fiber designed for 1550 nm (PM1550), orange for PM fiber designed for 980 nm (PM980), and green for highly doped PM erbium fiber (Er80). Crosses in the diagram indicate the locations of fiber splices. This figure is adapted from the master thesis of Alexis Labranche [1].

Laser Components and Configuration

The system begins with a **fiber Bragg grating-stabilized pump diode** at 979 nm, coupled to a PM fiber. This diode is stabilized in current and temperature by a laser diode controller. The CW light from the pump is directed through a **PM Wavelength Division Multiplexer (WDM)**, which reflects it to another port. This port configuration allows for counter-directional pumping of the gain medium, achieving higher gain compared to co-directional pumping, although it slightly increases the noise figure [32].

Stimulated emission from the gain fiber proceeds through the WDM to a **PM 30/70 output coupler**, which splits the light by directing 29% as output while recirculating 65% back into the laser cavity. The recirculated light passes through a **PM circulator** and is modulated by a **SAM**. The SAM acts as a passive mode-locking device, generating short pulses by absorbing lower-intensity light and transmitting higher-intensity light.

The circulator ensures unidirectional light flow, guiding the signal from the output coupler to the SAM and then back to the gain medium. This setup prevents any back reflections that could destabilize the mode-locking process. An **optical isolator** placed after the output coupler further prevents reflected or back-scattered light from re-entering the laser cavity, which is crucial for maintaining stable laser operation. A detailed list of the components in the laser setup can be found in Annex A. Furthermore, Annex B provides the optimized splicing parameters inspired from Rivard's work [15] for connecting Polarization-Maintaining fiber (PM1550) to Erbium-Doped Polarization Maintaining Fiber (Er80) using the FFS-2000 Vytran splicer from Thorlabs.

Gain Medium and Repetition Rate

The gain medium consists of a 20 cm segment of Er80 fiber, optimized for operation at the 1550 nm wavelength. Signal propagation occurs through PM1550 fiber, with the total optical cavity length being approximately 3.2 m. The refractive indices of the Er80 and PM1550 fibers are $n_{Er80} = 1.46$ and $n_{PM1550} = 1.449$, respectively, resulting in a cavity repetition rate of approximately 61 MHz, which closely matches the experimentally measured value of 60.9 MHz.

Group Velocity Dispersion and System Stability

The total GVD within the cavity is computed by considering the contributions from various components: a $+500$ fs^2 Group Delay Dispersion (GDD) from the Saturable Absorber Mirror, -2.283×10^4 fs^2/m GVD from the PM1550 fiber, and $+3.005 \times 10^4$ fs^2/m GVD from the

Er80 fiber. The resulting total GDD is approximately -66459 fs^2, with an average GVD of -19571 fs^2/m. This high GDD helps stabilize solitons against environmental perturbations, such as temperature fluctuations and mechanical vibrations, which are critical for maintaining the shape and size of the soliton. However, this also makes the system more susceptible to timing jitter due to the Gordon-Haus effect [33] [34], where phase and frequency shifts induced by Amplified Spontaneous Emission (ASE) noise lead to increased timing jitter.

Temperature Control and Environmental Stability

Despite the robustness of soliton formation in fiber lasers against temperature fluctuations, certain parameters like the threshold current for soliton formation, the central wavelength of the soliton, and the pulse width are sensitive to temperature variations. To mitigate these effects, the laser setup is housed in an environmentally controlled room maintained at a constant temperature of 23 ± 0.5 °C. Additionally, the fiber-based components are mounted on a 3 cm thick copper plate, chosen for its high thermal inertia, which enhances thermal stability.

The SAM, being particularly sensitive to temperature fluctuations, is thermally managed using a Peltier element coupled with a fan-assisted heat sink, ensuring precise temperature control within ± 0.004 °C. Furthermore, to prevent condensation that could damage the SAM, an adjustable nitrogen gas flow is introduced when the surrounding temperature is particularly low, around 5 to 10 °C.

3.1.2 Characterization

This Characterization provides a concise overview of soliton properties in the Master Oscillator under various conditions. The analysis examines the dependence of the mean output power on SAM temperature and pump power, the behavior of first-order solitons with changing pump power, the impact of SAM temperature on the soliton spectrum, and the properties of second-order solitons.

Mean Output Power

The Master Oscillator was characterized by measuring its mean output power across a range of SAM temperatures (from 5 °C to 45 °C) and pump powers (from 0 to 260 mW) at a constant ambient temperature of approximately 23 °C. Figure 3.2 compares the mean output power of the Master Oscillator (MO) after the isolator at two extreme SAM temperatures, 10 °C and 45 °C. The results indicate a linear relationship between the mean output power ($P_{\text{mean,10}}$

and $P_{\text{mean},45}$) and the pump power (P_{pump}), described by the following equations:

$$\begin{aligned} P_{\text{mean},10} &= 4.636 \times 10^{-2} \times P_{\text{pump}} - 1.362, \\ P_{\text{mean},45} &= 4.360 \times 10^{-2} \times P_{\text{pump}} - 1.462. \end{aligned} \tag{3.1}$$

At both temperatures, the laser initially emits no light, as the losses are too significant compared to the gain. As the gain increases sufficiently, the SAM enables the release of stored energy in the form of intense laser pulses, leading to a Q-switching regime. The ranges for stable first-order and second-order soliton mode-locking are indicated, with an unstable regime of Q-switching instabilities separating them. At higher pump powers, the system transitions into higher-order soliton regimes, which are unstable.

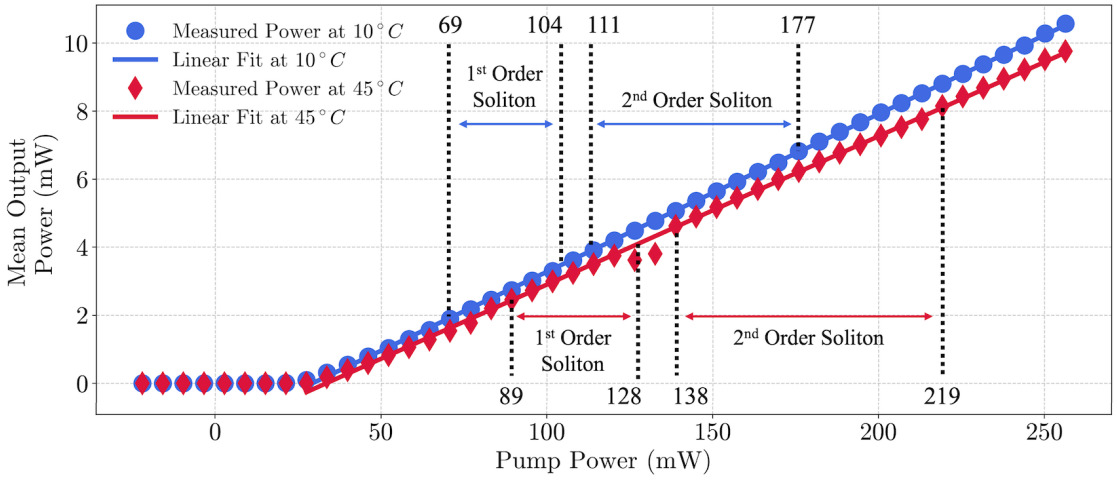

Figure 3.2 Mean output power of the MO at SAM temperatures of 10 °C and 45°C as a function of pump power.

It is observed that higher SAM temperatures result in lower mean output power and a higher pump power threshold. As explained in Section 2.1.4, increased SAM temperatures lead to reduced reflectance and higher saturation fluence, which in turn decrease the output power and raise the pump power threshold required to overcome the increased losses. This relationship is further illustrated in Figure 3.3, which shows the dependence of the SAM temperature on the mode-locking conditions. Specifically, it depicts the threshold pump power needed to enter the first-order soliton regime, the breakdown pump power where first-order soliton stability is lost, and the pump power threshold for entering the second-order soliton regime, all as functions of SAM temperature.

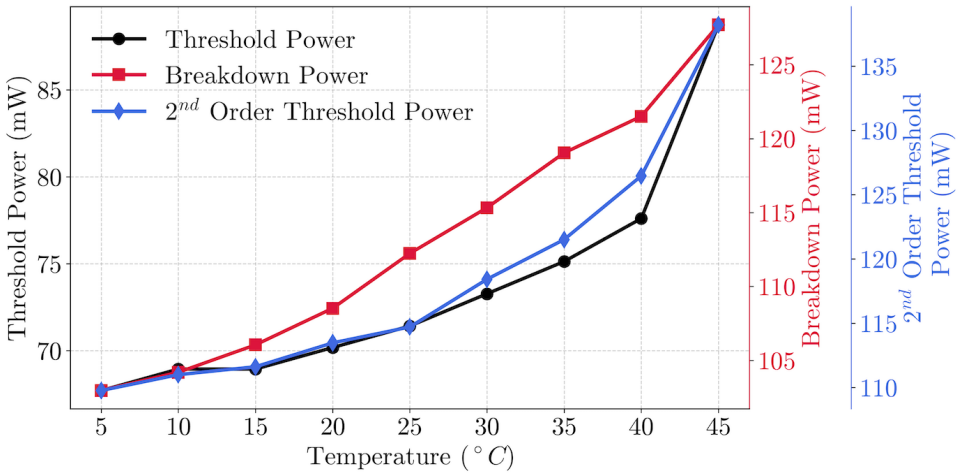

Figure 3.3 Pump power thresholds for mode-locking as a function of SAM temperature, showing the threshold power for entering the first and second-order soliton regimes, as well as the breakdown pump power where first-order soliton stability is lost.

Pump Power Dependence of First-Order Soliton

Figure 3.4(a) shows the normalized Power Spectral Density (PSD) of the first-order soliton for various pump powers, while maintaining the SAM temperature at a constant 10 °C. As predicted by the Area Theorem (2.30), increasing pump power results in shorter pulses and, consequently, a broader spectral bandwidth. Additionally, a redshift in the central wavelength is observed with increasing pump power. This shift can be attributed to the SAM converting some incoming photon energy into thermal energy, causing a transient rise in the temperature of the absorber during and after each pulse [19]. As the intracavity fluence increases, the SAM temperature rises further with each pulse, leading to a wavelength shift toward longer wavelengths as pump power increases.

Figure 3.4(b) provides a clearer illustration of this wavelength shift and also presents the Full Width at Half Maximum of the soliton pulse as a function of pump power, ranging from approximately 4.5 nm to 7.7 nm at maximum pump power.

Small peaks flanking the central soliton spectrum, known as *Kelly Sidebands* [35], are visible in Figure 3.4(a). These sidebands are a characteristic feature of fiber-based mode-locked lasers, arising from the interaction between the dispersion of the fiber and the nonlinearity of the soliton. As the soliton propagates through the cavity, it encounters periodic perturbations caused by imperfections in the laser cavity, leading to coupling with copropagating dispersive waves. Although this coupling is typically weak due to the continuously shifting relative phase between the soliton and the dispersive wave, near the soliton period $Z_0 = \pi T_0^2/2|\beta_2|$, a $\pi/4$

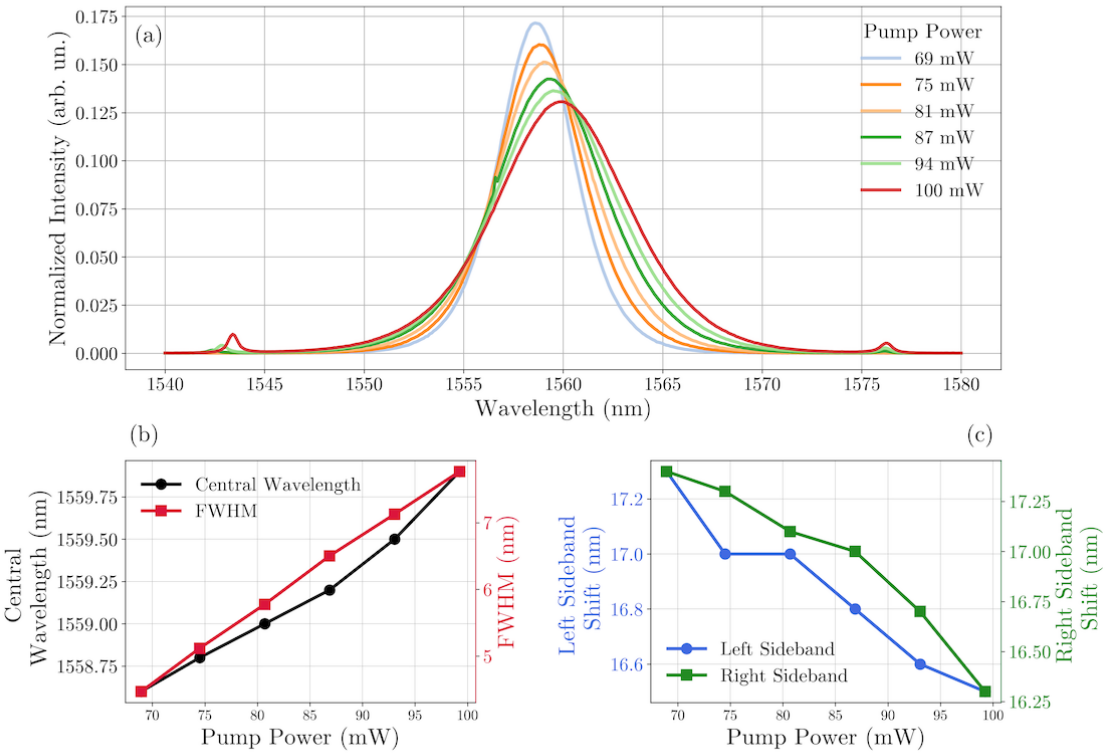

Figure 3.4 (a) Normalized PSD of first-order solitons at different pump powers and a constant SAM temperature of 10 °C. (b) Wavelength shift and FWHM of the soliton as a function of pump power. (c) Shift in left and right Kelly sidebands as a function of pump power.

phase shift from self-phase modulation enables quasi-phase matching between the soliton and dispersive waves, resulting in the observed sidebands.

These sidebands are usually symmetric around the central wavelength of the soliton. However, third-order dispersion can introduce asymmetry. The wavelength shift for the N^{th}-order Kelly sideband is given by [35]:

$$\delta\lambda_N = \mathrm{sgn}(N)\lambda_0\sqrt{\frac{2|N|}{cDL} - \frac{0.0787\lambda_0^2}{(c\tau_{\mathrm{FWHM}})^2}}, \tag{3.2}$$

where λ_0 is the central soliton wavelength, N is the sideband order, D represents the average intracavity dispersion, L is the cavity length, and τ_{FWHM} is the pulse duration at full width at half maximum.

The amplitude of these sidebands increases with higher pulse energies, corresponding to shorter pulse durations or higher pump powers. Minimizing these sidebands is essential because they are not intrinsic to the soliton pulse and contribute to energy loss, potentially destabilizing the soliton at high amplitudes. In these observations, only first-order Kelly sidebands are present, with relatively small amplitudes. Figure 3.4(c) shows the shift in the left and right sidebands as a function of pump power, highlighting a slight asymmetry and a decreasing spectral shift with increasing pump power.

Finally, these results provide an estimation of the pulse length using two methods:

1. **Using Kelly Sidebands:** The shift of Kelly sidebands relative to the central wavelength and the known mean intracavity dispersion in PM1550 fiber (15.9 ps/(nm km)) provide an estimate of the pulse duration at two extreme pump powers. Specifically, for pump powers of 69 mW and 104 mW, the pulse durations are estimated to be 576 fs and 312 fs, respectively.

2. **Using Time-Bandwidth Product:** According to Equation (2.12), the sech^2 pulse durations can be estimated from the spectral Full Width at Half Maximum (FWHM). The pulse durations for pump powers of 69 mW and 104 mW are estimated at 570 fs and 329 fs, respectively, which corroborates the results obtained by the first method.

Temperature dependence of first-order soliton

Figure 3.5 illustrates the effects of varying the temperature of the SAM on the soliton spectrum at their corresponding threshold pump powers. As expected from section 2.1.4, one can observe that increasing the temperature of the mirror yields a spectral shift to higher wavelength and broadens the spectral FWHM. Indeed, as the temperature increases, the absorbance increases resulting in higher pump power threshold. This higher pump threshold which in turn yields through the area theorem (2.30) a broader spectrum. The FWHM goes from 4.3 nm to 6 nm for the temperatures going from 5 °C to 45 °C resulting in respective pulse length of 594 fs and 393 fs.

Second-Order Soliton

Higher-order solitons, such as second-order solitons, occur when the input power exceeds the threshold required for a fundamental soliton in a fiber optic system [14]. While fundamental solitons maintain a consistent shape due to a balance between nonlinear effects and dispersion, higher-order solitons exhibit periodic oscillations in their shape and size. This periodic

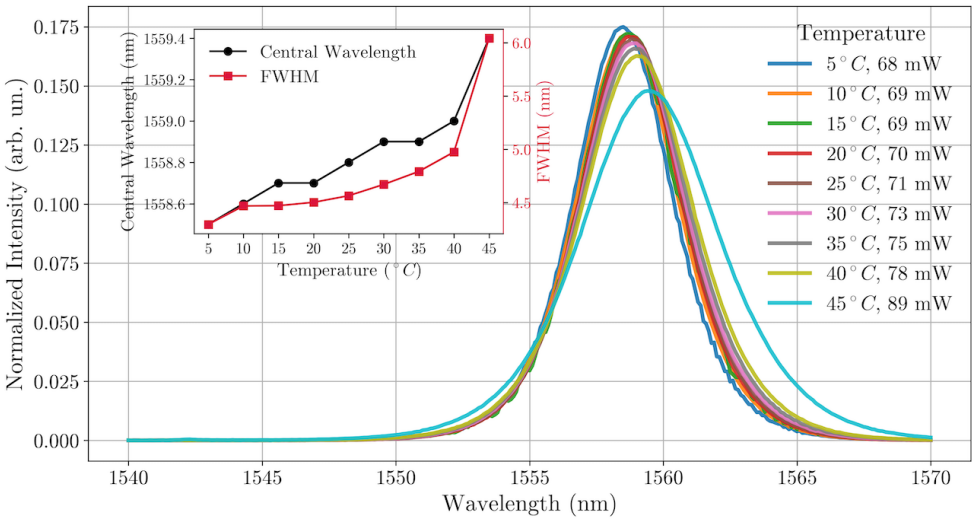

Figure 3.5 Effect of SAM temperature on the first-order soliton spectrum at the corresponding threshold pump powers. The inset shows the central wavelength and FWHM plotted as functions of SAM temperature.

behavior results from enhanced nonlinear effects due to the increased power, causing the soliton to compress and decompress as it propagates. As a result, higher-order solitons are less stable than fundamental solitons and are particularly sensitive to external perturbations, such as temperature fluctuations or variations in pump power. These complex pulses can break up into fundamental solitons through phenomena like higher-order dispersion, Raman scattering, or two-photon absorption [36].

In the experiments, stable second-order solitons were observed, indicating potential applications worth further exploration. However, it is important to note that maintaining stable propagation of higher-order solitons requires strict control over external factors, including temperature, pump power, and mechanical vibrations.

Figure 3.6(a) shows the PSD of second-order solitons at different pump powers. Figure 3.6(b) presents the corresponding central wavelength and FWHM as functions of pump power, and Figure 3.6(c) shows the spectral shift for the left and right first-order Kelly sidebands.

The FWHM increases from 6.7 nm to 9.3 nm as the pump power increases from 95 mW to 126 mW, corresponding to pulse durations of 380 fs and 274 fs, respectively.

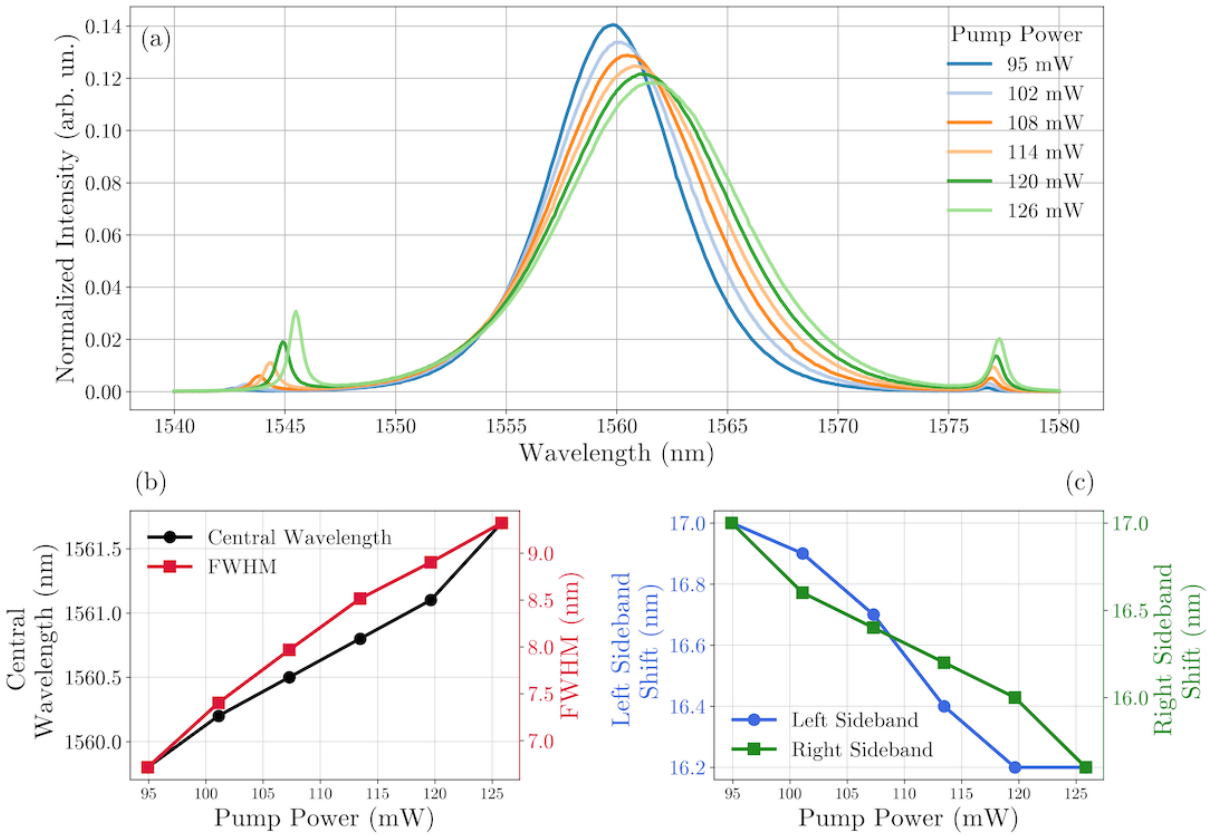

Figure 3.6 (a) PSD of second-order solitons at different pump powers. (b) Central wavelength and FWHM as functions of pump power. (c) Spectral shift of the left and right first-order Kelly sidebands as a function of pump power.

3.1.3 Relative Intensity Noise

Characterizing noise sources in a laser setup is essential, particularly in applications like generating quantum entangled photon pairs, where the performance depends heavily on the peak power of each laser pulse. A critical metric for assessing this aspect is the Relative Intensity Noise (RIN), which quantifies fluctuations in the output power of the laser over time, reflecting variations in the energy of individual pulses.

RIN is defined as the ratio of the standard deviation of pulse energies to the mean pulse energy [37]:

$$\mathrm{RIN} = \frac{\sigma_{\mathrm{energy}}}{\mu_{\mathrm{energy}}}. \tag{3.3}$$

Intensity fluctuations can arise from various sources. External factors include technical noise from the pump, thermal fluctuations, and mechanical vibrations, while internal noise is primarily due to quantum phenomena such as ASE or quantum vacuum fluctuations [38].

RIN is often characterized in the frequency domain via its PSD [39]:

$$\mathrm{RIN}(f) = \mathcal{F}\left\{\frac{\langle (P(t) - P_{\mathrm{mean}})^2 \rangle}{P_{\mathrm{mean}}^2}\right\}. \tag{3.4}$$

Here, P_{mean} is the average optical power, $\mathcal{F}$ denotes the Fourier transform, and $\langle (P(t) - P_{\mathrm{mean}})^2 \rangle$ represents the mean square intensity fluctuation. The Fourier transform of this fluctuation provides the noise spectral density.

The RIN PSD helps identify noise sources across different frequency ranges. In passive mode-locked lasers, noise at lower frequencies (below the relaxation oscillation frequency of erbium-doped fiber, around 1 kHz) is predominantly influenced by pump noise [38]. Although ASE also affects noise at these frequencies, its impact is typically minor compared to pump noise. Beyond this frequency, noise levels generally decrease significantly [40] [41], although it may increase slightly in cavities with high net intracavity dispersion.

Typically, the RIN PSD peaks around the relaxation oscillation frequency and then decreases, approaching the quantum noise limit near 1 MHz. This baseline noise, known as shot noise, is consistent across all frequencies:

$$S_{\mathrm{shot}} = \frac{2h\nu}{P_{\mathrm{mean}}}. \tag{3.5}$$

For the Master Oscillator, operating at a pump power of 69 mW with the SAM temperature maintained at 10 °C, the shot noise level is calculated to be -158 dB/Hz.

RIN can be measured using two primary techniques: in the time domain with an oscilloscope and in the spectral domain with an electrical spectrum analyzer. Both methods use a photodiode to convert the laser light into a photocurrent, which is then transformed into a voltage using a load resistance. The voltage response of the photodiode to a laser pulse is described by the convolution of the response function of the photodiode $\phi_{\mathrm{PD}}(t)$ with the pulse profile of the laser $P(t)$:

$$V_{\mathrm{PD}} \propto \int_{-\infty}^{\infty} \phi_{\mathrm{PD}}(t-\tau) P(\tau)\, d\tau \approx E_p \phi_{\mathrm{PD}}(t). \tag{3.6}$$

For accurate measurements, two conditions must be met:

- The pulse duration t_{pulse} must be much shorter than the response time of the photodiode t_{PD}: $t_{\text{pulse}} \ll t_{\text{PD}}$.
- The response time of the photodiode must be significantly shorter than the pulse train period T_r: $t_{\text{PD}} \ll T_r$.

The first condition allows the pulse profile to be approximated as a delta function proportional to the pulse energy, while the second ensures the ability to observe the noise floor between pulses.

Both measurement methods were applied in this study. Measurements were taken at the output of the Master Oscillator, operating at a pump power of 69 mW, with the SAM and ambient temperatures at 10 °C and 23 °C, respectively. While these parameters were used for characterization, any change in parameters would require a re-evaluation of the RIN.

An InGaAs photodiode (DET01CFC) with a 1.2 GHz bandwidth was used, connected to a 2.5 GHz oscilloscope (DSO9254A) with a 20 GSa/s sampling rate, 205 Mpts memory depth, and 8-bit vertical resolution. A reduced sampling rate of 10 GSa/s was used to extend measurement duration and improve Resolution Bandwidth (RBW), balancing the need to avoid undersampling and aliasing. This approach was validated through experimental procedures and previous studies [1].

This setup confirmed that the ultrafast criteria were met: a $t_{\text{pulse}} \approx 570$ fs pulse at the Master Oscillator output, a $T_r \approx 16$ ns pulse train period, and a photodiode response time of $t_{\text{PD}} \approx 0.8$ ns, ensuring $t_{\text{pulse}} \ll t_{\text{PD}} \ll T_r$ for accurate measurements.

Temporal Characterization of RIN

Figure 3.7 presents the temporal characterization of RIN, following the methodology described by R. Smith et al. [37]. The voltage for each pulse, V_{pulse}, is obtained by subtracting the noise floor voltage, V_{floor}, from the peak voltage, V_{peak}:

$$V_{\text{pulse}} = V_{\text{peak}} - V_{\text{floor}}. \tag{3.7}$$

Figure 3.7(a) illustrates this process, where the noise floor is averaged over 80% of the interval for each pulse period. Without averaging, the RIN is calculated over a frequency range determined by the measurement duration and the Nyquist limit, resulting in a temporal RIN in the range [64.5 Hz, 30 MHz] of 0.199%. A lower spectral range analysis, shown in Figure 3.7(b), applies a moving average window, resulting in a temporal RIN in the range [64.5 Hz, 1 MHz] of 0.1%.

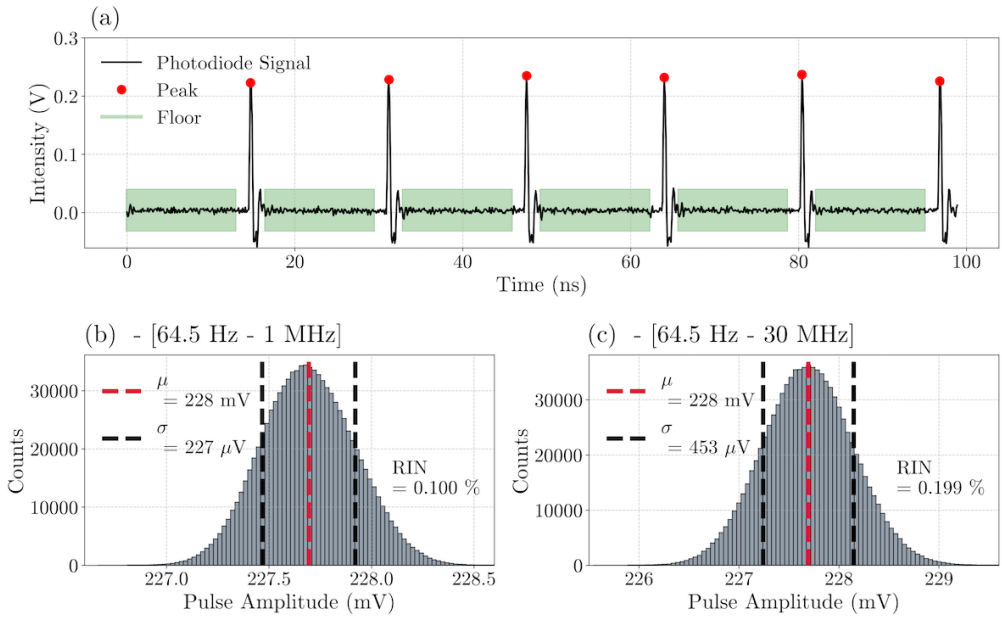

Figure 3.7 Temporal characterization of RIN at different spectral ranges.

Spectral Characterization

The RIN PSD was calculated using Eq. (3.4). Figure 3.8 displays the resulting RIN PSD under the same conditions as those used in the temporal characterization. The figure also includes the Integrated Root Mean Square Relative Intensity Noise (i-RIN), which is the square root of the integrated RIN, and the shot noise level.

As expected, a peak is observed near the relaxation oscillation frequency of the erbium gain medium at approximately 1 kHz, followed by a significant reduction at higher frequencies. However, around 1 MHz, the RIN PSD reaches a plateau at approximately -136 dB/Hz, which is believed to be primarily due to photodiode shot noise. This is a known issue in mode-locked fiber lasers, where RIN PSD measurements are often limited by the photodetection shot noise [38]. Although the RIN PSD should ideally be characterized up to half the repetition rate of the laser, the noise beyond 1 MHz is typically very low and near the quantum limit, so this range is often neglected in the literature.

Therefore, the RIN characterized around 1 MHz and above does not accurately reflect the true performance of the laser. However, calculating the i-RIN for frequencies below 1 MHz still provides valuable insights, and results above this frequency are provided for reference, though with caution. In this study, the integrated RIN over the frequency range [64.5 Hz, 1 MHz] is approximately 0.081%.

The RIN values obtained from both temporal and spectral domain measurements are con-

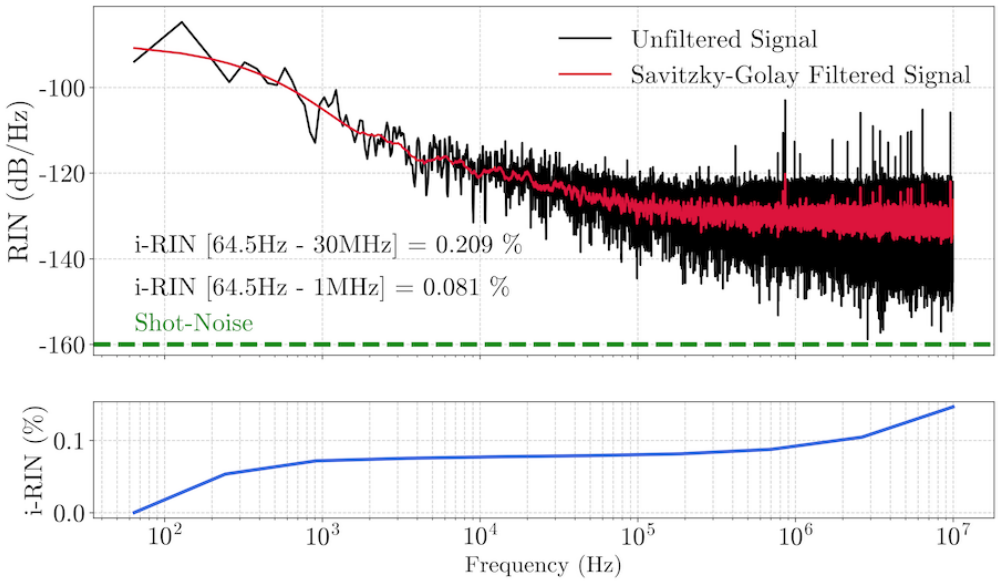

Figure 3.8 Spectral characterization of RIN, showing the power spectral density, integrated RMS RIN, and shot noise level.

sistent, confirming the validity of the approach. However, using a higher power photodiode is recommended to reduce the detection shot noise level beyond -158 dB/Hz. Additionally, employing an electrical spectrum analyzer could yield more accurate results in the spectral domain.

The integrated Root Mean Square (RMS) RIN of approximately 0.081% in the frequency range [64.5 Hz, 1 MHz] for a net intracavity dispersion of about -0.066 ps^2 is comparable to other setups [38]:

1. A 163-MHz Semiconductor Saturable Absorber Mirror (SESAM) soliton Er-fiber laser with -0.013 ps^2 net dispersion has an i-RIN of 0.072% in the range [10 Hz, 100 kHz] [41].

2. A 303-MHz Carbon Nanotube Saturable Absorber (CNT-SA) soliton Er-fiber ring laser with -0.0023 ps^2 net dispersion has an i-RIN of 0.032% in the range [10 Hz, 100 kHz] [42].

3. A 1-GHz SESAM soliton Er-fiber laser exhibits an i-RIN of 0.014% in the range [10 Hz, 10 MHz] [43].

4. A 1-GHz SESAM soliton Ytterbium-doped Potassium Yttrium Tungstate (Yb:KYW) laser shows an i-RIN of 0.08% in the range [1 Hz, 200 kHz] [44].

To further reduce the i-RIN, several improvements can be considered. Although the room

and SAM are temperature stabilized and some fiber components are placed on a high-inertia copper plate to minimize external disturbances, the primary source of intensity noise appears to be the pump technical noise. Despite current and temperature stabilization of the pump diode, implementing a feedback control loop that regulates the pump current based on the output power of the Master Oscillator could substantially reduce low-frequency noise in the laser.

Mean Output Power Stability

Figure 3.9 shows the mean output power of the Master Oscillator, recorded at a sampling rate of 1 Hz over a period of 60 minutes. This measurement allows the observation of potential transient behaviors and assesses the long-term stability of the setup. The measurement began several minutes after the mode-locked laser was started, with a pump power of 69 mW, while the room and SAM temperatures were kept at 23 °C and 10 °C, respectively. The output power remained stable, with a relative standard deviation of 0.056%.

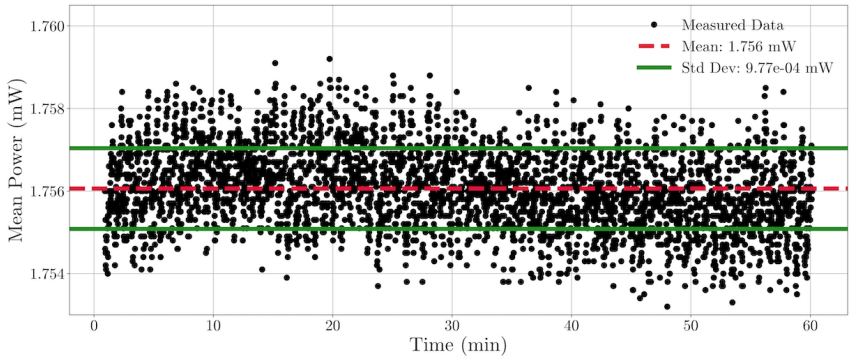

Figure 3.9 Mean output power drift of the Master Oscillator over 60 minutes.

3.2 Erbium-Doped Fiber Amplifier

The soliton pulse energy generated by the master oscillator is often insufficient to drive nonlinear processes such as SPDC. A commonly used solution to amplify such femtosecond pulses is the EDFA [45, 46]. In this setup, an erbium-doped fiber acts as the gain medium, pumped around 980 nm, to amplify the output pulse of the master oscillator.

During the amplification stage, the pulse transitions from a soliton to what is known as a *similariton*, which is another type of asymptotic solution to the GNLSE [47]. Similaritons exhibit a self-similar behavior, maintaining a parabolic intensity profile as they propagate.

Unlike solitons, which achieve stability through a balance between dispersion and nonlinearity, similaritons can increase in both amplitude and width while preserving their shape. This property allows them to withstand higher intensities without distorting, thus preventing wave breaking even under strong nonlinear conditions and enabling the maintenance of higher pulse energies.

However, at the end of the amplification stage, the high intensity within fused silica fibers can introduce several nonlinear effects that may degrade pulse quality. Although SPM is typically the predominant effect for soliton pulses in an EDFA [48], other nonlinear phenomena such as TOD and intrapulse Raman scattering [49] may also emerge. Intrapulse Raman scattering is particularly problematic as it redshifts the pulse spectrum by transferring energy from higher to lower frequency components due to the interaction between the pulse electric field and the vibrational modes of the fiber medium. To control these effects, the technique of Chirped Pulse Amplification (CPA) is utilized [50]. CPA involves stretching the pulse temporally before amplification, which lowers the peak power and, consequently, reduces the impact of nonlinearities during amplification. After the pulse has been amplified, it is recompressed to its original, or even a shorter, duration, allowing for high peak powers without the adverse effects typically associated with high-intensity interactions in the fiber.

This approach is particularly effective in managing the erbium gain bandwidth, as it facilitates the amplification of a wider spectral range while avoiding gain narrowing, a common challenge in EDFAs where the gain spectrum is often narrower than the signal spectrum.

In this work, the developed EDFA, when seeded with the master oscillator pulse, achieved a maximum averaged output power of approximately 265 mW and broadened the input pulse from a 4.5 nm FWHM to a 55 nm FWHM output.

3.2.1 Setup

Figure 3.10 illustrates the EDFA setup. The gain medium is bi-directionally pumped by two 979 nm Fiber Bragg grating stabilized diodes, each delivering up to 906 mW of continuous wave power. These diodes are coupled to polarization-maintaining fibers and are equipped with optical isolators to prevent back-reflections, ensuring consistent and stable operation. The pump light is routed into the erbium-doped fiber via a Wavelength Division Multiplexer.

Before entering the gain medium, the seed pulses from the master oscillator are temporally stretched by propagating through 1.7 meters of PM1550 fiber, which has anomalous dispersion ($\beta_2 = -0.0228$ ps^2/m). This stretching reduces the peak power, helping to minimize nonlinear effects. The stretched pulses are then amplified and simultaneously compressed

in 1.1 meters of highly doped polarization-maintaining erbium fiber (Er80-4/125-HD-PM), which has normal dispersion ($\beta_2 = 0.03$ ps^2/m), leading to an increase in pulse intensity.

To recompress the pulse while simultaneously minimizing nonlinear effects such as SPM, TOD, and intrapulse Raman scattering, the length of the PM1550 fiber after the second WDM is optimized to 0.5 meters to prevent nonlinear pulse break-up. At the output, the amplified light is coupled into an Fiber Connector / Angled Physical Contact (FC/APC) PM patch fiber, which reduces back-reflections and refracts any residual reflections out of the system. Finally, the light is collimated using an aspheric lens.

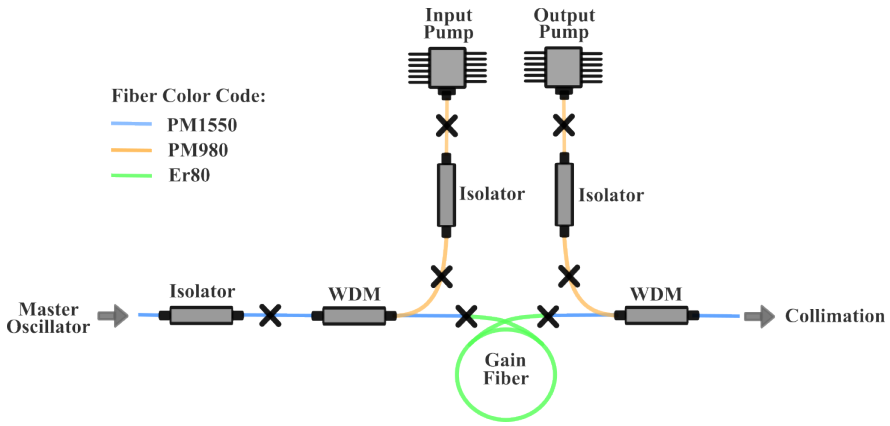

Figure 3.10 Schematic diagram of the EDFA setup. Crosses in the diagram indicate the locations of fiber splices. Adapted from the master thesis of Alexis Labranche [1].

3.2.2 Characterization

The performance of the EDFA was evaluated by independently varying the input and output pump powers while measuring the corresponding output spectra, FWHM, and output power, with the master oscillator serving as the seed source. In this context, the "input pump" refers to the diode that injects power co-directionally with the pulse propagation at the entry side of the EDFA, while the "output pump" denotes the diode providing counter-directional pumping.

The characterization was performed with the master oscillator operating at a pump power of 69 mW, a SAM temperature of 10 °C, and a room temperature of 23 °C, resulting in an average output power of 1.9 mW and a FWHM of 4.5 nm.

Single Pump Characterization

Figure 3.11 (a) shows the EDFA output spectrum as a function of varying input pump powers, with the output pump turned off. Figure 3.11 (b) illustrates the output spectrum for varying output pump powers, with the input pump turned off. For comparison, all spectra were normalized to the maximum intensity observed at the highest pump power of 906 mW. Notably, spectral oscillations indicative of SPM are observed in Figure 3.11 (a), but are absent in Figure 3.11 (b). This difference occurs because, in the first scenario, the pulse reaches higher energy more rapidly, propagating through a longer fiber length at elevated power, thereby increasing SPM effects.

Figure 3.11 (c) presents the variation in FWHM for both input and output pump configurations, with the opposing pump turned off in each case. Figure 3.11 (d) depicts the corresponding output power of the EDFA as a function of input and output pump powers.

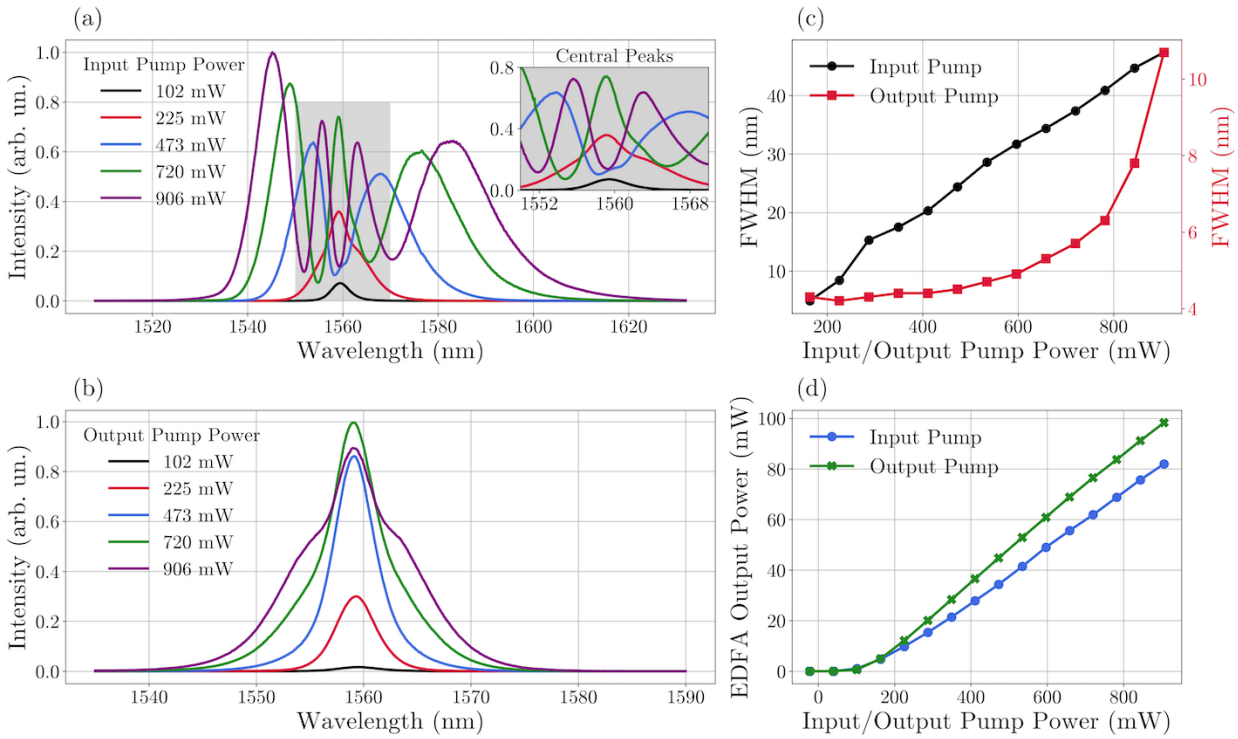

Figure 3.11 (a) EDFA output spectrum as a function of varying input pump powers with the output pump turned off. (b) EDFA output spectrum for varying output pump powers with the input pump turned off. (c) FWHM variation for input and output pump configurations. (d) Output power of the EDFA as a function of input and output pump powers.

Dual Pump Characterization

Figures 3.12 (a) and 3.12 (b) show the output spectrum of the EDFA for varying input and output pump powers, respectively, while the other pump is maintained at its maximum power. As with the single pump characterization, all spectra were normalized to the maximum intensity of the highest spectrum for comparison. When the input pump is set to its maximum power, the FWHM bandwidth shows a gradual increase as the output pump power rises, ranging from approximately 42 nm to 55 nm. In contrast, increasing the input pump power with the output pump at its maximum leads to a much more significant broadening, expanding from around 10 nm to 55 nm. This pronounced difference is due to the stronger SPM effects induced by the input pump compared to the output pump.

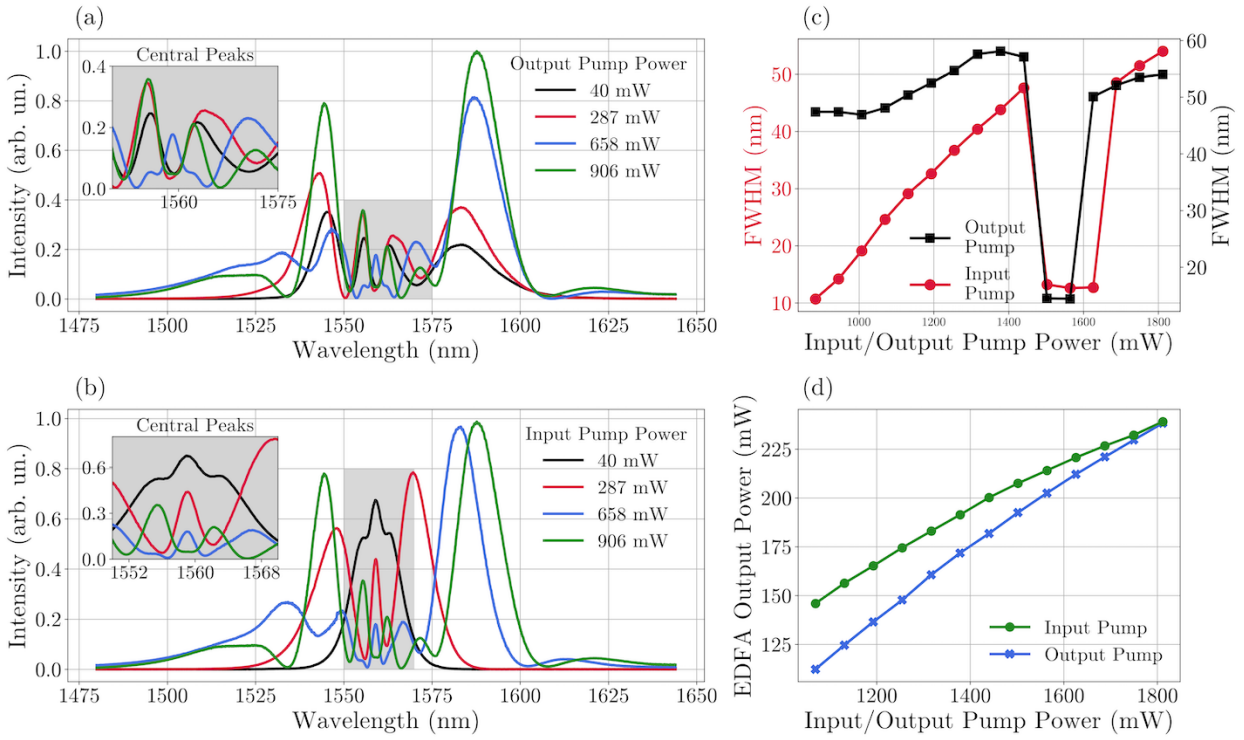

Figure 3.12 (a) EDFA output spectrum for varying input pump powers with the output pump set to its maximum power. (b) EDFA output spectrum for varying output pump powers with the input pump set to its maximum power. (c) FWHM variation for input and output pump configurations. (d) Output power of the EDFA as a function of input and output pump powers.

The nonlinear phase shift resulting from SPM, $\Delta\phi_{\mathrm{SPM}}$, can be estimated by counting the

number of peaks N in the spectrum using the formula [48]:

$$\Delta\phi_{\text{SPM}} \approx \left(N - \frac{1}{2}\right)\pi. \tag{3.8}$$

For an input power of 473 mW and an output power of 0 mW, as seen in Figure 3.11 (a), two spectral peaks are observed, corresponding to a nonlinear phase shift of 1.5π. In comparison, when both the input and output pumps are set to 906 mW, as shown in Figure 3.12 (a), seven peaks appear, indicating a nonlinear phase shift of 6.5π.

A reduction in spectral bandwidth is observed when the total pump power reaches approximately 1500-1600 mW. This is likely due to the emergence of a new peak caused by SPM, which causes the second peak at the lower wavelength to drop below the half-maximum intensity of the other peak at higher wavelengths.

The characteristic two-peak structure at the extremes of the spectrum, with multiple intermediary peaks, is a signature of SPM. However, an asymmetry is noted, with the peak at the longer wavelength being more intense than that at the shorter wavelength. This asymmetry could result from several factors, including intrapulse Raman scattering, which transfers energy from shorter to longer wavelengths, or from the initial pulse shape, where the Kelly sidebands of the soliton spectrum at the master oscillator output are more intense at longer wavelengths. The primary cause of this asymmetry, however, is likely the increased TOD at higher pulse energies within the EDFA, particularly in the fused silica fiber.

Gain Characterization

The gain provided by the EDFA was characterized as a function of the master oscillator input power. Figure 3.13 presents the output power and the corresponding gain as a function of the seed power. The results indicate a decreasing gain with increasing input power, dropping from approximately 26 dB to around 14 dB, which can be attributed to gain saturation in the EDFA. Additionally, a plateau is observed in the range of 1.9 mW to 3.7 mW, corresponding to the first-order soliton regime. This plateau indicates that in this regime, the output power of the EDFA is relatively insensitive to the output power of the master oscillator due to saturation effects.

At higher input powers, specifically in the range of 4 mW to 6.4 mW, which corresponds to the second-order soliton regime, the output power begins to increase again. This behavior occurs because in the second-order soliton regime, the repetition rate is doubled compared to the first-order soliton regime, resulting in a lower pulse energy. Consequently, the reduced pulse energy leads to less saturation of the EDFA, allowing for a renewed increase in output

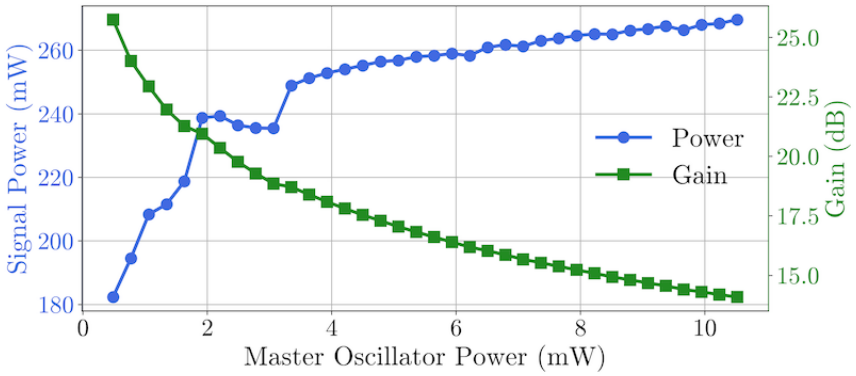

Figure 3.13 EDFA output power and corresponding gain as a function of master oscillator input power.

power.

3.2.3 Second Harmonic Generation Frequency-Resolved Optical Gating

To fully characterize the pulse at the output of the laser setup, it is essential to obtain information about the temporal shape of the electric fields along with the corresponding phase. A technique that enables this is Second Harmonic Generation Frequency-Resolved Optical Gating (SHG FROG) [51]. This technique utilizes the SHG process to measure the complete electric field (both intensity and phase) of an optical pulse. It operates on the principle of autocorrelation, where a pulse is split into two, and one of the pulses is delayed relative to the other. The two pulses are then combined in a second-order nonlinear medium, in this case, a Thin Beta Barium Borate (BBO) crystal, to generate a second harmonic signal. The spectrum of this second harmonic signal as a function of the delay between the two pulses allows for the reconstruction of the original temporal shape and phase of the pulse through an inversion algorithm.

Setup

Figure 3.14 shows the SHG FROG setup. An ultrafast laser pulse $E(t)$ is first split into two beams using a 50:50 beam splitter. One beam travels through a variable delay line τ, allowing precise control over the timing between the two pulses. Both beams are then recombined and focused into a nonlinear crystal via a parabolic mirror, generating a second harmonic signal $E_{\text{SHG}}(t, \tau) \propto E(t) \cdot E(t - \tau)$. The resulting second harmonic signal is collected and focused into a spectrometer, which records the intensity as a function of frequency and delay

time [52]:

$$I_{\mathrm{FROG}}(\omega,\tau) = \left| \int dt\, E(t)E(t-\tau)e^{-i\omega t} \right|^2 . \tag{3.9}$$

The pulse characteristics are retrieved using a Python implementation of the MATLAB package developed by Steven Byrnes [53]. This package implements the Principal Component Generalized Projections Algorithm (PCGPA) [54].

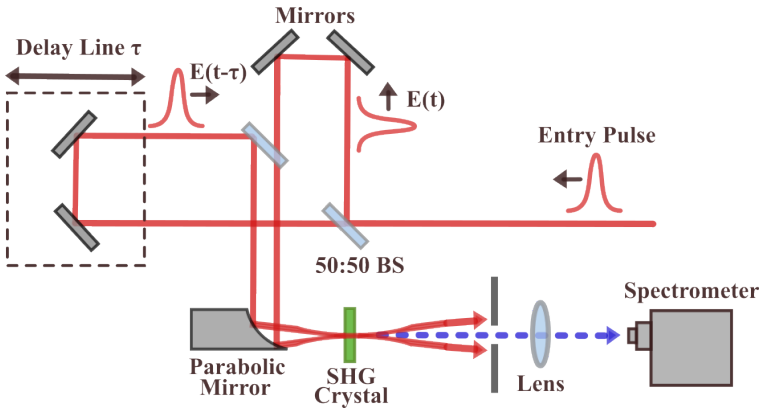

Figure 3.14 Schematic of the SHG FROG setup used for pulse characterization.

Results

Figure 3.15 presents the results for the master oscillator operating in the first-order soliton regime with a pump power of 69 mW, a SAM temperature of 10 °C, and a room temperature of 23 °C. The input and output pump powers for the EDFA were optimized at 535 mW and 906 mW, respectively to reach a total pulse energy of 3.95 nJ. Figures 3.15(a) and 3.15(b) show the measured and retrieved FROG traces, demonstrating good correspondence and confirming the accuracy of the pulse reconstruction. Figure 3.15(c) displays the transform-limited (TL) and retrieved temporal pulse profiles with their associated phases. The temporal pulse shape is consistent with similar setups [45, 46], exhibiting asymmetric pulse characteristics indicative of a mix of linear and higher-order chirp. The satellite peaks are likely due to parasitic TOD effects within the EDFA. Although the main peak encompasses approximately 60 % of the total pulse energy, the side peaks represent a significant loss of energy. Compensation methods, such as employing a prism compressor, should ideally be incorporated in this regime to mitigate these satellite pulses and potentially improve overall performance. Despite the presence of these artifacts, the achieved FWHM of 102 fs, although not as short as the Transform-Limited (TL) duration of 71 fs, should still be adequate for enhancing nonlinear effects in SPDC. The GDD is estimated at approximately -5500 fs^2.

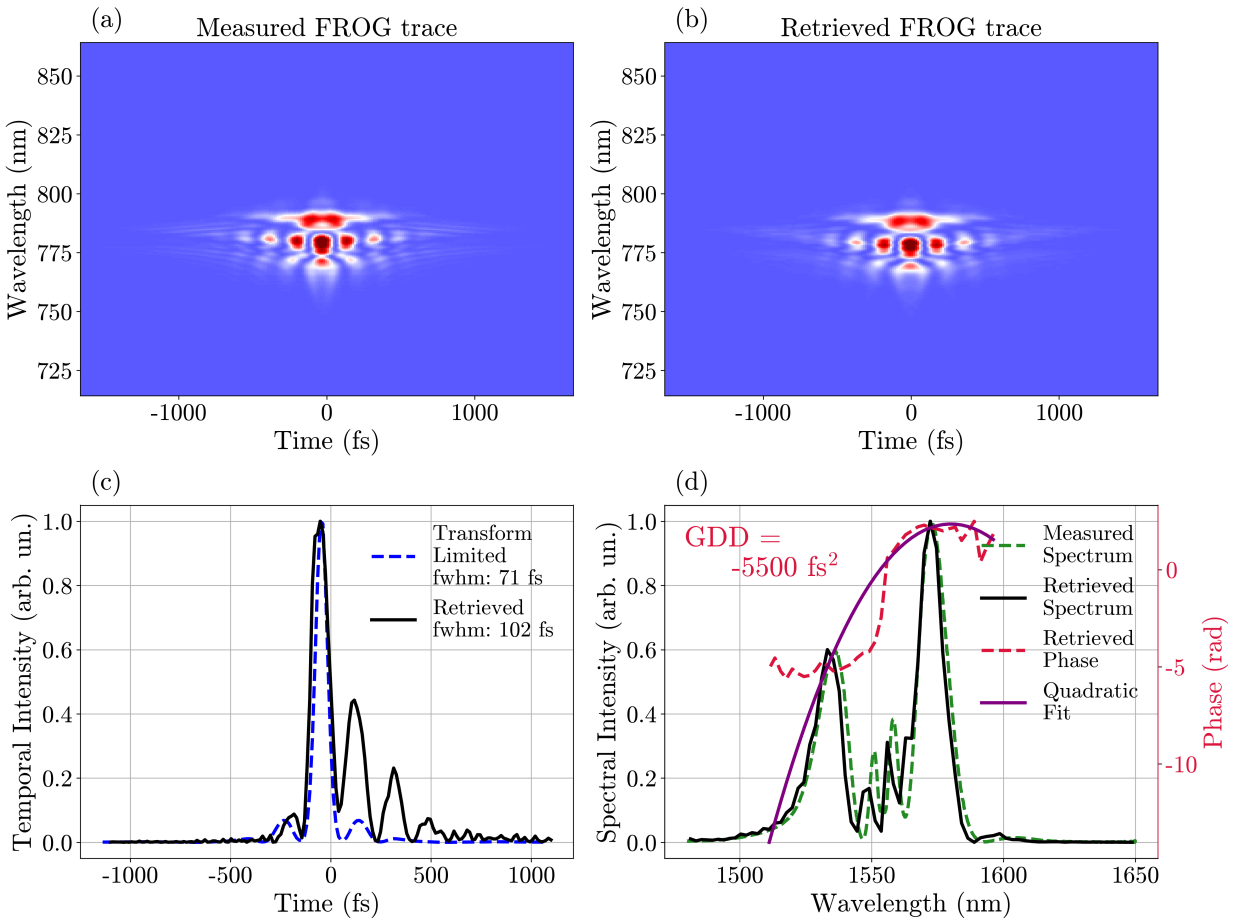

Figure 3.15 Characterization of the EDFA output in the first-order soliton regime using SHG FROG. Panels (a) and (b) show the measured and retrieved FROG traces, verifying effective pulse reconstruction. Panels (c) and (d) compare the transform-limited and retrieved pulse shapes and phases in the temporal and spectral domains, highlighting the effects of linear and higher-order chirp and the impact of parasitic TOD.

Figure 3.16 details the results for the master oscillator operating in the second-order soliton regime with a pump power of 111 mW, a SAM temperature of 10 °C, and a room temperature of 23 °C. Both the input and output pump powers of the EDFA were maximized at 906 mW. As the pulse energy in the second-order regime is lower than in the first-order regime, nonlinear effects such as SPM and TOD are diminished. This results in a narrower spectral bandwidth with fewer satellite pulses, leading to a central pulse that encapsulates almost all the pulse energy.

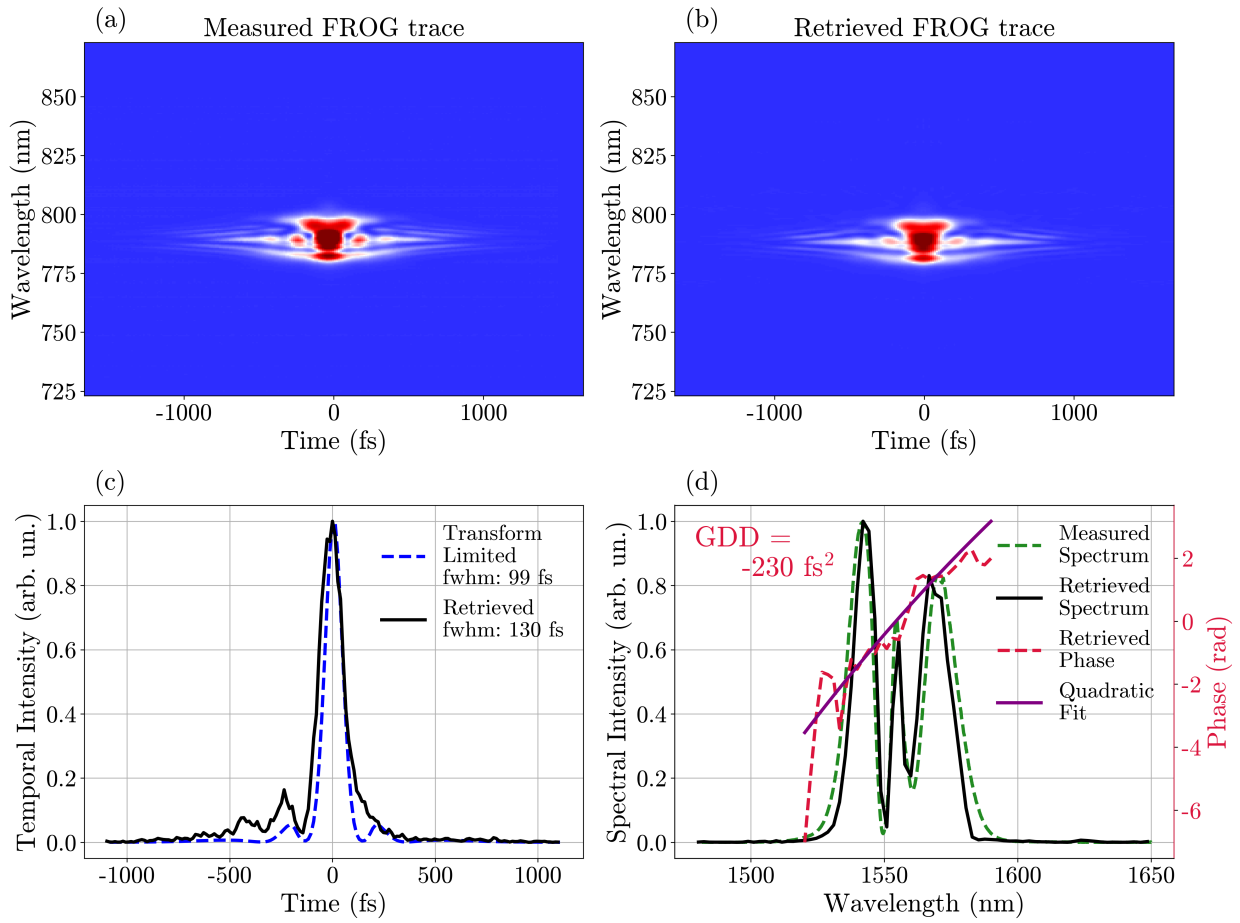

Figure 3.16 Characterization of the EDFA output in the second-order soliton regime using SHG FROG. Panels (a) and (b) show the measured and retrieved FROG traces, verifying effective pulse reconstruction. Panels (c) and (d) compare the transform-limited and retrieved pulse shapes and phases in the temporal and spectral domains, highlighting the effects of linear and higher-order chirp and the impact of parasitic TOD.

3.3 Discussion

The ultrafast fiber laser system developed in this chapter has been extensively characterized for versatile use across various configurations. The system consists of two main components: the Master Oscillator and the Erbium-Doped Fiber Amplifier.

The Master Oscillator operates effectively in both first and second-order soliton regimes. In the first-order regime, it produces stable solitons at approximately 1559 nm, with a repetition rate of 60.9 MHz, supporting pulse energies from 30 pJ to 75 pJ and temporal widths between 594 fs and 312 fs. In the second-order regime, it maintains solitons around 1560 nm with a doubled repetition rate of 121.8 MHz, accommodating pulse energies from 30 pJ to 72 pJ

and durations from 380 fs to 261 fs. The system demonstrates high output stability with a relative intensity noise of approximately 0.081% from 64.5 Hz to 1 MHz.

The EDFA amplifies these pulses via chirped pulse amplification, achieving a maximum averaged output power of approximately 265 mW and broadening the pulse from 4.5 nm to 55 nm FWHM. SHG FROG measurements show a pulse duration of 102 fs in the first-order regime and 130 fs in the second-order regime at the EDFA output.

The characterization of RIN requires further improvement, as current measurements are limited by photodetection shot noise. Additionally, implementing a feedback loop based on the output optical power to regulate the pump current could help reduce technical noise and further stabilize the laser output.

Although the system performs well, its capabilities can be further optimized. The nonlinear effects within the EDFA present challenges that could be mitigated by implementing a more controlled Chirped Pulse Amplification process. Adjusting the pre-chirp fiber length at the input of the EDFA and incorporating a prism compressor at the output could help minimizing nonlinear effects and reducing the impact of satellite pulses.

Finally, the ultrafast laser system provides a solid foundation for the cascaded SHG-SPDC process, offering the necessary high-intensity, stable pulses required for efficient nonlinear optical conversion.

CHAPTER 4 SECOND HARMONIC GENERATION

4.1 Introduction

Following the development of the ultrafast fiber laser system in the previous chapter, this section introduces the SHG stage, which will be integrated into a cascaded setup in future work. In this setup, the SHG stage doubles the frequency of the pump laser, producing a second harmonic signal that serves as the pump for the subsequent SPDC process. This method is particularly useful for quantum optics experiments, where the original pump pulse will be used as a local oscillator for balanced homodyne detection of the signal and idler fields.

This chapter describes the design and characterization of the SHG setup, focusing on the arrangement of optical components to maximize SHG efficiency. The selection of Magnesium Oxide-doped Periodically Poled Lithium Niobate (MgO:PPLN) as the nonlinear crystal is explained, along with methods to increase SHG power while minimizing the risk of crystal damage. Additionally, a single-prism pulse compressor is implemented to filter out residual pump light and further compress the SHG pulse temporally.

4.2 Setup

Figure 4.1 illustrates the setup for the Second Harmonic Generation process. The pulsed pump beam, generated by the master oscillator and amplified by the Erbium-Doped Fiber Amplifier, is collimated using an aspheric lens to minimize spherical aberrations. PM fibers and PM components are used throughout the laser setup, ensuring a linearly polarized output.

The setup includes a Half-Wave Plate (HWP) followed by a Polarizing Beam Splitter (PBS), which refines the polarization of the beam and enables the extraction of a portion of the beam to be used as a local oscillator in future experiments. A second HWP adjusts the pump polarization to meet the quasi-phase matching conditions in the PPLN crystal. An aspheric lens $L1$ focuses the pump beam into the PPLN crystal, while a second aspheric lens $L2$ collimates the generated second harmonic and collects any residual pump light. Both fields are directed through a single-prism compressor, primarily to spatially filter out residual pump light, which was found to interfere with the detection of the SPDC signal in the subsequent stages. The compressor also offers the potential for further temporal compression of the second harmonic pulse, though this has not yet been fully optimized. The resulting second harmonic signal is then prepared for the following stages of the project, including the SPDC

process.

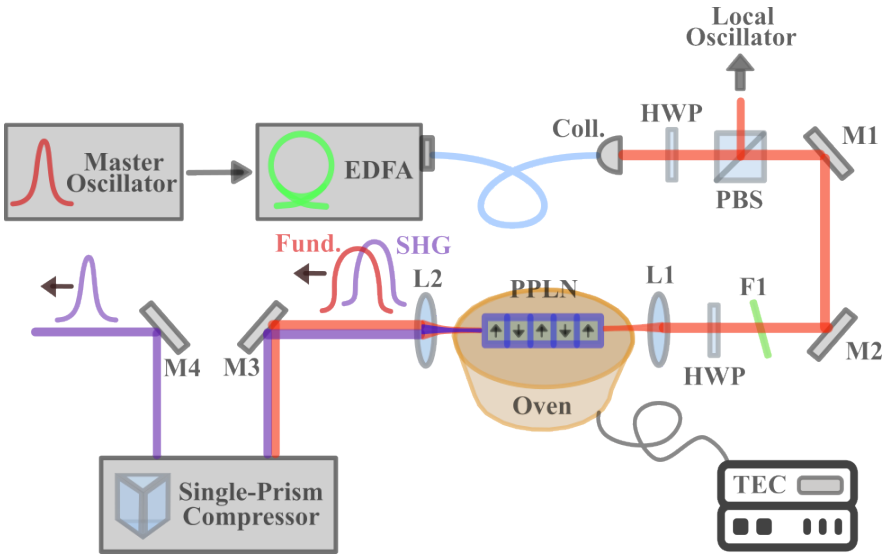

Figure 4.1 Schematic of the SHG setup showing the key components and their arrangement for effective second harmonic generation. M: Mirror; L: Lens; F: Filter; EDFA: Erbium-doped fiber amplifier; HWP: half-wave plate; PBS: polarizing beam splitter; Coll.: collimator; Fund.: fundamental; SHG: generated second harmonic; PPLN: periodically-poled Lithium Niobate crystal.

4.3 Optimizing Focusing and Temperature in MgO:PPLN for SHG Efficiency

The second-order nonlinear crystal selected for SHG is a type-0 5% MgO-doped periodically poled lithium niobate, where both the pump and Second Harmonic (SH) fields exhibit extraordinary polarization. This crystal, chosen for its high second-order nonlinear coefficient ($d_{\text{eff}} = 14$ pm/V), has a length of 0.3 mm to minimize temporal walk-off effects. Manufactured by Covesion, it features six grating periods ranging from 18.8 μm to 20.3 μm in steps of 0.3 μm.

To optimize SHG power, careful consideration of the focusing conditions is essential. According to the literature [55, 56], the ideal condition occurs when $L/b \approx 2.84$, where L is the optical path length in the crystal and b is the confocal parameter (twice the Rayleigh length). However, overly small focus areas within the crystal can lead to damage. Two primary damage mechanisms are the Photorefractive Effect [57], which involves refractive index changes due to the redistribution of free electrons, and Green Induced Infrared Absorption (GRIIRA) [58], caused by green light from parasitic higher-order effects that can lead to infrared absorption and damage through polarons formed from crystal defects such as Niobium

(Nb) antisite defects and Iron (Fe) ion impurities.

To achieve a balance between the optimal L/b ratio, available focal lengths, and the manufacturer's specified damage threshold of 8 GW/cm^2, a collimation lens with a focal length of 6.34 mm (C110TM-C) was used, along with additional lenses $L1$ and $L2$ (11 mm, C220TM-C). This configuration resulted in an L/b ratio of 0.9 and a peak intensity within the crystal of 6.9 GW/cm^2. While the L/b ratio deviates from the ideal, this setup ensures efficient SHG output without exceeding the damage threshold of the crystal, thereby balancing performance and crystal longevity.

Temperature control is also key to optimizing SHG efficiency by fine-tuning the quasi-phase-matching conditions. The PPLN crystal is housed in an oven controlled by a Thermoelectric Controller (TEC), which allows precise temperature adjustments from ambient to 200 °C. The theoretical relationship between the PMF and temperature for a grating period of 19.7 μm is shown in Figure 4.2, where the dispersion characteristics for MgO:PPLN are taken from the Sellmeier equations presented in [59]. The inset of Figure 4.2 shows how the central wavelength and FWHM of the PMF vary with temperature. Although PPLN crystals are typically sensitive to temperature variations, the short crystal length in this setup reduces the overall impact of temperature changes. While models predict an optimal phase-matching temperature around 100 °C for a 1560 nm pump wavelength, experimental results showed maximum SHG power at a lower temperature of 70 °C for most grating periods.

4.4 Characterization of SHG Spectrum Across PPLN Grating Periods

Figure 4.3 presents the SHG spectra measured for various PPLN grating periods, with the crystal maintained at a temperature of 70 °C. These measurements were performed with the master oscillator operating in the first-order soliton regime, under a pump power of 69 mW, a saturable absorber mirror temperature of 10 °C, and an ambient room temperature of 23 °C. The input and output pump powers for the EDFA were set at 535 mW and 906 mW, respectively.

The results demonstrate that the SHG signal can be tuned over a wavelength range from 760 nm to 800 nm, with corresponding average powers between 14.5 mW and 46 mW. Lower PPLN grating periods produced broader spectra at shorter wavelengths, whereas higher grating periods resulted in narrower spectra at longer wavelengths. The peak SH power was observed at a grating period of 19.7 μm, indicating an optimal configuration for achieving maximum output power around 792 nm.

The inset graph shows the average power output as a function of the grating period, high-

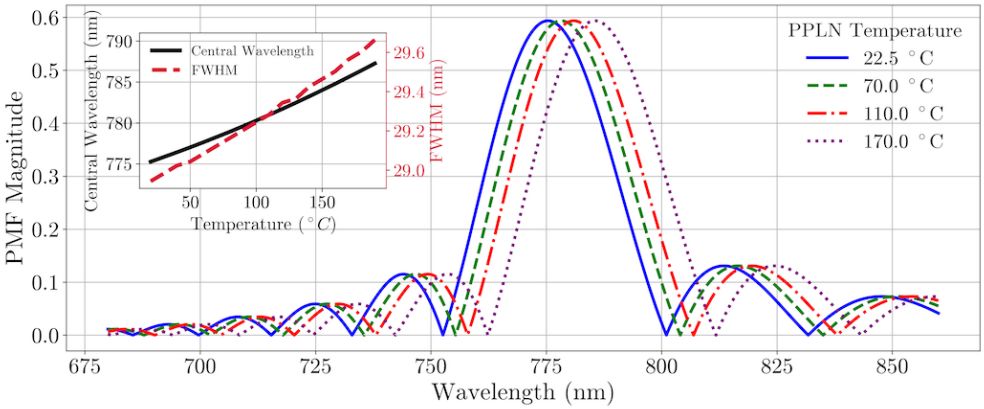

Figure 4.2 Temperature dependence of the PMF for PPLN with a grating period of 19.7 μm, showing variations in central wavelength and FWHM at different temperatures.

lighting that while the 19.7 μm period yields the highest power, other periods, especially at the extremes of the grating range, may provide more suitable spectral profiles for specific applications.

At the grating period of 19.7 μm, the measured pulse energy reaches 0.76 nJ. Considering the total energy of the pump pulse, the conversion efficiency is approximately 20 %. However, when accounting only for the energy contained in the main peak of the pump pulse, the conversion efficiency increases to 32 %. Notably, compressing the pump pulse prior to SHG could enhance the conversion efficiency further.

4.5 Single Prism Pulse Compressor

As previously mentioned, a single-prism pulse compressor, adapted from the model presented by Chauhan et al. [60], has been implemented at the output of the SHG setup with a SF10 Prism. This configuration primarily serves to spatially filter out the residual pump light, which was found to be detrimental when trying to detect the SPDC signal. Additionally, it provides the potential for further temporal compression of the second harmonic pulse, although this aspect was not a primary focus.

Figure 4.4(a) illustrates the setup of the single-prism pulse compressor. The chirped input pulse enters from the left and first encounters a half mirror, which directs the pulse through the prism before reaching a retroreflector. The pulse is then reflected back through the prism, passes through a roof mirror ensuring correct angular orientation, and is redirected again by the retroreflector to make a final pass through the prism. The beam exits the compressor by reflecting off the upper part of the half mirror. This design inherently maintains zero angular

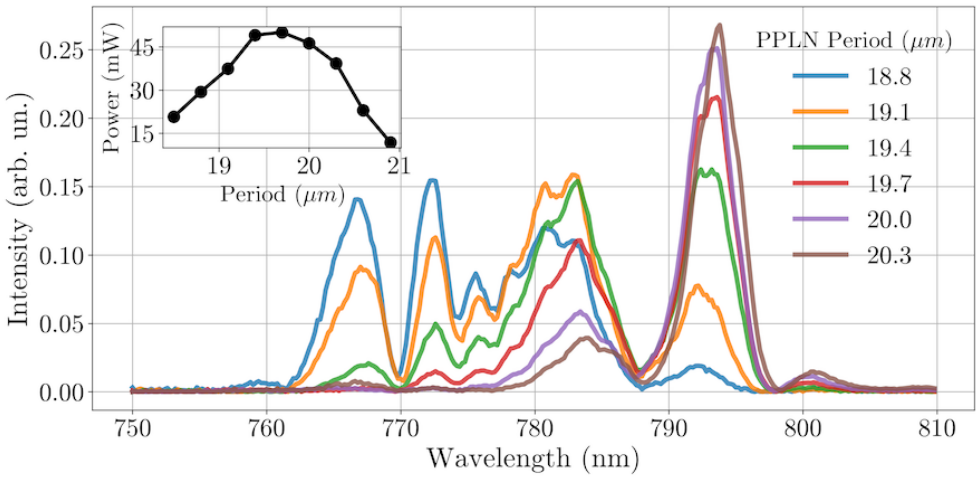

Figure 4.3 SHG spectra for different PPLN grating periods at a crystal temperature of 70 °C, showing the dependency of output power with grating period.

dispersion, zero pulse-front tilt, zero spatial chirp, and unity magnification, simplifying the traditional setup complexities associated with alignment and tuning.

The prism is positioned to disperse the incident light into its constituent wavelengths at Brewster's angle, $\theta_B = \tan^{-1}(\frac{n_{\text{prism}}}{n_{\text{air}}}) \approx 59.715°$, crucial for minimizing p-polarized light loss due to reflection at the air-prism interface. The GDD imparted by this configuration can be precisely calculated through ray tracing, which accounts for both geometric and material dispersion effects within the prism setup [61]:

$$\left.\frac{\mathrm{d}^2\phi}{\mathrm{d}\omega^2}\right|_{\omega_l} = \frac{\lambda_l^3}{2\pi c^2}\left[L_g \left.\frac{\mathrm{d}^2 n}{\mathrm{d}\lambda^2}\right|_{\lambda_l} - \left(4L + \frac{L_g}{n^3}\right)\left(\left.\frac{\mathrm{d}n}{\mathrm{d}\lambda}\right|_{\lambda_l}\right)^2\right], \tag{4.1}$$

where $L = 2q + \delta_c$ represents the apex-to-apex prism distance, q is the distance between the prism and the retroreflector, δ_c is the constant internal path length in the retroreflector and L_g, the optical path length through the prism glass, depending on the apex angle α.

Figure 4.4(b) shows the autocorrelation trace obtained using the FR-103MN industrial autocorrelator from Femtochrome, similar to the work of Wasylczyk et al. [62]. The measurement was taken with a distance of 23 cm between the prism and the retroreflector, resulting in an estimated GDD of -1402 fs^2. It is important to note that this distance has not been optimized, as the current results were satisfactory. However, further optimization could lead to better performance. The trace was recorded for a PPLN crystal with a grating period of 19.7 μm, with the master oscillator operating in the first-order soliton regime. The operating

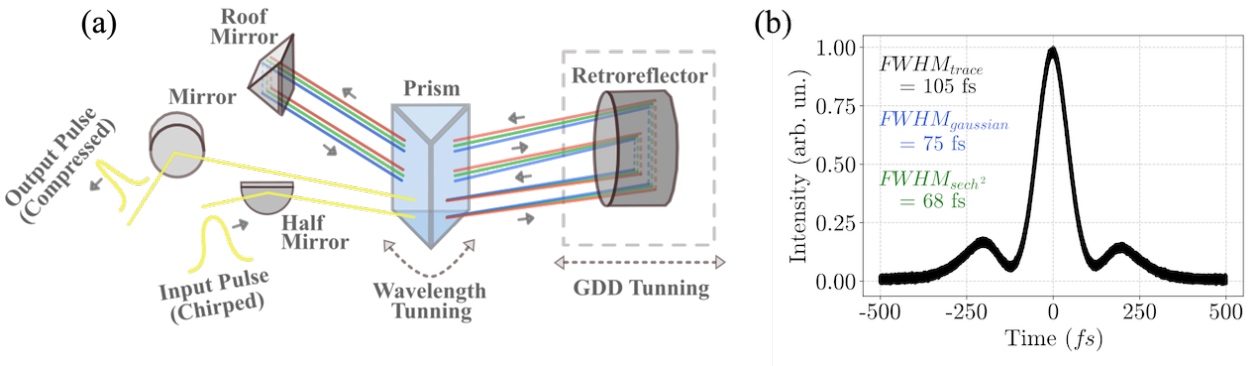

Figure 4.4 (a)Schematic diagram of the single-prism pulse compressor setup showing the path of the chirped input pulse through the optical components, illustrating the process of pulse compression and the final collimated output. (b) Autocorrelation trace of the pulse from a PPLN with a period of 19.7 μm operating under first-order soliton conditions, displaying a temporal FWHM of 105 fs.

conditions included a pump power of 69 mW, a SAM temperature of 10 °C, and an ambient temperature of 23 °C. The input and output powers for the EDFA were set at 535 mW and 906 mW, respectively.

The autocorrelation trace exhibits a complex structure, with prominent side lobes likely caused by the presence of satellite pulses in the pump pulse, as seen in the SHG FROG trace in Figure 3.15. The trace has a FWHM of 105 fs. Assuming a Gaussian pulse profile, the estimated pulse width would be approximately 75 fs, while a sech^2 profile would suggest a pulse duration of about 68 fs. However, caution is advised when interpreting these values, as the idealized pulse shapes do not account for the side lobes observed in the autocorrelation trace, indicating a more complex pulse structure.

Autocorrelation measurements, while useful for estimating pulse width, do not capture the full temporal structure of the pulse, particularly when additional features like satellite pulses are present. These features can distort the pulse shape and lead to inaccuracies in the estimated pulse duration. Thus, relying solely on the autocorrelation trace may provide an incomplete picture of the pulse characteristics. To obtain a more detailed temporal profile, a frequency-resolved optical gating measurement, similar to that performed on the pump pulse at the EDFA output, is recommended. This would allow for the reconstruction of the full temporal structure of the SHG pulse.

Moreover, the satellite pulses could potentially be mitigated by using a two-prism pulse compressor before the SHG stage, as discussed in the previous section. This would facilitate more precise pulse shaping and compression, reducing the occurrence of satellite pulses and

enhancing the overall pulse quality for subsequent nonlinear processes.

4.6 Discussion

The optimization of the SHG output from the MgO:PPLN crystal was successfully achieved to ensure sufficient power levels for the subsequent SPDC process. The optimization process involved fine-tuning the focusing conditions and temperature control of the crystal, balancing the goal of maximizing SHG efficiency with the need to avoid potential crystal damage. The resulting spectra demonstrated that the SHG signal could be tuned effectively across a wavelength range from 760 nm to 800 nm, with average powers ranging from 14.5 mW to 46 mW. Lower poling periods of the PPLN crystal produced broader spectra at shorter wavelengths, while higher periods yielded narrower spectra at longer wavelengths, with a peak at a grating period of 19.7 μm. This configuration was identified as optimal for achieving higher SHG output, particularly around 792 nm.

Despite the positive outcomes, certain areas require further optimization. The performance of the single-prism pulse compressor, while effective in filtering residual pump light, has not been fully optimized for temporal compression. As discussed earlier, the current setup achieves a theoretical GDD of -1402 fs^2 but was not optimized beyond that point, as the results were considered sufficient for this phase of the project. However, further investigation into the capabilities of the pulse compressor could lead to better compression results, which would improve the overall system performance and enhance the efficiency of the subsequent SPDC process.

Moreover, the autocorrelation measurements of the SHG pulse indicated the presence of satellite pulses, which likely arose from the complex pump pulse structure. Addressing this issue through improved compression techniques, such as implementing a two-prism pulse compressor before the SHG stage, could help eliminate these satellite pulses, resulting in cleaner pulse profiles and more efficient nonlinear processes. Additionally, operating the SHG process with the pump laser in the second-order soliton regime offers another avenue for improvement. This approach could reveal configurations that enhance the SHG output, further aligning the performance of the system with the specific requirements of the SPDC stage.

In conclusion, the development and characterization of the SHG stage have provided a solid foundation for the next phase of the project, focused on SPDC. While the current results support the goal of generating entangled photon pairs, opportunities remain for further improvements in pulse compression and spectral optimization. Future work will build on these

findings to refine the system and enhance its overall performance.

CHAPTER 5 OPTIMIZING SECOND-ORDER NONLINEAR MATERIALS

5.1 Introduction

Building on the experimental groundwork detailed in the previous two chapters, including the development of an ultrafast fiber laser system and the successful demonstration of second harmonic generation, this chapter shifts focus to optimizing second-order nonlinear materials. These materials are crucial for the future development of the Spontaneous Parametric Down-Conversion stage, with the goal of creating a bright, pure, and broadband source of entangled photons.

Non-classical light sources fundamentally depend on second-order nonlinear materials that facilitate processes like Spontaneous Parametric Down-Conversion and Second Harmonic Generation [24, 63]. Modulating the nonlinear susceptibility in these materials can significantly influence the efficiency and spectral characteristics of the resulting optical processes.

The importance of such modulation has seen a surge in the development of inverse design techniques aiming at optimizing crystal structures for diverse applications [64–66]. While various methods, from machine learning [22] to algorithms like simulated annealing [29, 67] and Monte Carlo [28], have emerged, challenges persist in achieving an ideal entangled photon source characterized by high photon rates, spectral purity, and broadband performance.

This work extends upon previous earlier methodologies that employed simulated annealing, suggesting that genetic algorithms could yield more sophisticated solutions across a broader spectrum of problems [29,67]. To this end, a genetic algorithm has been developed to address these complexities. Drawing inspiration from natural evolution, this algorithm focuses on crafting optimal crystal designs. Its efficiency, especially in fields where the search space is vast and the landscape of potential solutions has numerous local optima, has been validated in previous studies [68–70].

Additionally, two distinct optimization methods have been developed. The first extends the traditional methods within the framework of first-order perturbation, specifically tailored for tuning the phase matching function of crystals, which will be refereed as the *PMF Optimization Problem*. The second method directly incorporates the nonlinear coupled mode wave equation, allowing to directly explore the dynamics happening in the crystal, and look at the spectral distribution of signal/idler fields without resorting to the low-gain approximation, which will be refereed as the *Nonlinear Coupled Mode Equations (NCME) Optimization Problem*.

5.2 Methodology

5.2.1 Problem Formulation

As depicted in Figure 5.1(a), nonlinear crystals are modeled as segmented into N domains, each of equal width, Λ. This width can be chosen arbitrarily by the user, for instance, to correspond to the coherence length of the nonlinear process under consideration, defined as $\Lambda = \pi/\Delta k$ [24, 63], or any other required value. Each domain has an orientation, d, which can take values of either $+1$ or -1. Collectively, these domains define the nonlinear profile of the crystal, forming the set of unknown parameters, Θ, in the inverse problem:

$$\Theta = \{d_1, d_2, ..., d_{N-1}, d_N\}. \tag{5.1}$$

The total number of possible crystal configurations within the solution space is 2^N. Each nonlinear profile can be associated to a specific phase-matching function, $\Phi(\Delta k)$, when addressing the *PMF Optimization Problem*. Alternatively, these profiles can be incorporated into the nonlinear coupled mode equations to compute the resulting signal and idler spectra in the context of the *NCME Optimization Problem*. In either case, the task consist in finding the nonlinear profile that most closely aligns with the desired phase-matching function or the target spectra. The challenge lies in navigating this vast, non-convex space to find the optimal profile.

5.2.2 Phase-Matching Function Optimization

As said previoulsy, each domain configuration can be associated with a given phase matching function $\Phi(\Delta k)$ via a Fourier transform [29] :

$$\Phi(\Delta k) = \int_{-L/2}^{L/2} g(z) e^{i\Delta k(\omega_s, \omega_i)} dz, \tag{5.2}$$

where L represents the length of the crystal, $\Delta k(\omega_s, \omega_i) = k_p(\omega_s + \omega_i) - k_s(\omega_s) - k_i(\omega_i)$ is the phase mismatch depending on the material dispersion and $g(z) \in \{-1, +1\}$ is the continuous representation of the nonlinear profile of the crystal Θ along the direction of propagation z.

A target PMF $\Phi_t(\Delta k)$ can then be defined such that the problem consist in minimizing the Mean Squared Error (MSE) :

$$\mathrm{MSE}_{\mathrm{pmf}} = \sum_{n=1}^{M} \frac{|\Phi(\Delta k_n) - \Phi_t(\Delta k_n)|^2}{M}. \tag{5.3}$$

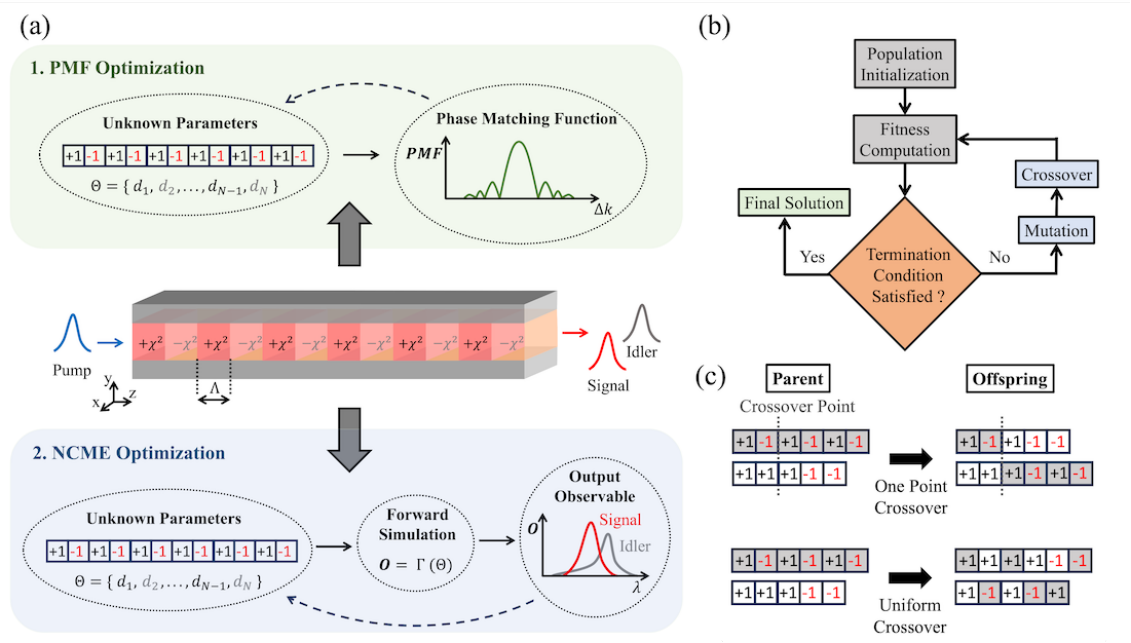

Figure 5.1 (a) Representation of the inverse problem. (b) Diagram of the genetic algorithm. (c) One-point and uniform crossover diagram.

This measure the distance between the Φ and Φ_t by selecting sufficiently many, say $M = 1000$, points Δk_n in a given range of phase mismatch values.

5.2.3 NCME Optimization

In the second optimization method, target spectra for the signal and idler fields, $T_{\mathrm{s}}(\omega_s)$ and $T_{\mathrm{i}}(\omega_i)$, are defined. The output state of the crystal is represented by the spectra of the signal and idler fields, $O_{\mathrm{s}}(\omega_s)$ and $O_{\mathrm{i}}(\omega_i)$, in the SPDC process occurring within the crystal. These spectra are used to evaluate how closely the unknown parameters align with the target functions.

The dynamics of the system are captured by the forward simulation function, $\Gamma(\cdot)$. To simplify the problem, the transverse spatial distribution of the fields is neglected, focusing instead on the propagation axis and spectral distribution, as the primary dynamics of interest occur in these domains. However, it is worth noting that further investigation into the transverse effects could reveal other interesting applications [22]. The nonlinear coupled-mode wave equations are derived based on (2.51) and (2.52), with an additional simplification made using the undepleted pump approximation (the pump field remains largely unaffected by the weak SPDC process) :

$$
\begin{aligned}
i\frac{\partial \mathcal{A}_i^{(\mathrm{out})}(z,\omega)}{\partial z} &= -\frac{\omega^2}{c^2 k_i(\omega)}\,\chi^{(2)}(z)\int \mathrm{d}\omega' e^{-i\Delta k(\omega,\omega')}\mathcal{A}_p(z,\omega+\omega')\mathcal{A}_s^{(\mathrm{vac})*}(z,\omega'),\\
i\frac{\partial \mathcal{A}_s^{(\mathrm{out})}(z,\omega)}{\partial z} &= -\frac{\omega^2}{c^2 k_s(\omega)}\,\chi^{(2)}(z)\int \mathrm{d}\omega' e^{-i\Delta k(\omega,\omega')}\mathcal{A}_p(z,\omega+\omega')\mathcal{A}_i^{(\mathrm{vac})*}(z,\omega'),\\
i\frac{\partial \mathcal{A}_i^{(\mathrm{vac})}(z,\omega)}{\partial z} &= -\frac{\omega^2}{c^2 k_i(\omega)}\,\chi^{(2)}(z)\int \mathrm{d}\omega' e^{-i\Delta k(\omega,\omega')}\mathcal{A}_p(z,\omega+\omega')\mathcal{A}_s^{(\mathrm{out})*}(z,\omega'),\\
i\frac{\partial \mathcal{A}_s^{(\mathrm{vac})}(z,\omega)}{\partial z} &= -\frac{\omega^2}{c^2 k_s(\omega)}\,\chi^{(2)}(z)\int \mathrm{d}\omega' e^{-i\Delta k(\omega,\omega')}\mathcal{A}_p(z,\omega+\omega')\mathcal{A}_i^{(\mathrm{out})*}(z,\omega').
\end{aligned}
\tag{5.4}
$$

Here, $\mathcal{A}_i^{(\mathrm{out})}$ and $\mathcal{A}_s^{(\mathrm{out})}$ represent the envelopes of the idler and signal fields, respectively, such that the output spectra are given by $O_{\mathrm{i}}(\omega_i) = \mathcal{A}_i^{(\mathrm{out})}(z = L/2, \omega_i)$ and $O_{\mathrm{s}}(\omega_s) = \mathcal{A}_s^{(\mathrm{out})}(z = L/2, \omega_s)$, which are subsequently normalized. The system of equations is then numerically integrated using the fourth-order Runge-Kutta method, as described in Ref. [71].

This simulation takes the unknown parameters as inputs and produces the corresponding output spectra. The inverse design problem then involves determining the set of unknown parameters, Θ, that best match the given target functions [22]:

$$
\Theta = \Gamma^{-1}(T_{\mathrm{s}}, T_{\mathrm{i}}),
\tag{5.5}
$$

where Γ^{-1} represents the inverse problem.

To assess the alignment between the obtained output spectra and the desired target spectra, a MSE fitness function is employed:

$$
\mathrm{MSE}_{\mathrm{jsa}} = \sum_{n=1}^{M}\left[\frac{[|\,O_{\mathrm{s}}(\omega_{s,n})| - |\,T_{\mathrm{s}}(\omega_{s,n})|]^2 + [|\,O_{\mathrm{i}}(\omega_{i,n})| - |\,T_{\mathrm{i}}(\omega_{i,n})|]^2}{M}\right].
\tag{5.6}
$$

This metric quantifies the distance between the output spectra and the target functions by sampling a sufficiently large number of M points across the frequency ranges of interest.

5.2.4 Genetic Algorithm Description

The genetic algorithm developed for optimizing nonlinear crystal designs operates in four key stages, as outlined in Figure 5.1(b) and supported by previous studies [68–70, 72]:

1. **Initialization:** The algorithm begins by generating an initial population of n crystal designs. These designs can be randomly generated, based on predefined poling profiles,

or provided by the user (e.g., from a previous optimization). Crystal length can be specified with minimum and maximum bounds, allowing more exploration, or fixed by setting equal bounds.

2. **Simulation and Fitness Evaluation:** Each crystal design undergoes a forward simulation to calculate its output observable, such as by integrating the PMF or solving nonlinear coupled mode equations. The fitness of each design is then evaluated by comparing the output to the target.

3. **Termination Condition:** The algorithm iterates through generations until a termination condition is met, such as achieving a desired fitness level or reaching the maximum number of iterations.

4. **Genetic Operators:** If the termination condition is not met, the algorithm applies genetic operators—mutation, crossover, elitism, and natural selection—to evolve the population for the next generation.

The genetic operators are applied as follows to ensure a thorough exploration of the solution space:

- **Elitism:** The top 10% of individuals, based on fitness, are directly copied to the next generation to conserve they high-quality traits.

- **Uniform Crossover:** This operation is applied with a probability of 0.9 and involves combining genes from two parent crystals. Random segments of poling profile from each crystal are swapped iteratively. The process continues until the entire length of the shorter profile is covered, with each swap occurring with a probability of 0.9.

- **One-Point Crossover:** Applied with a probability of 0.8, this operator selects a random cut-point within the crystal profiles of two parents. Segments beyond this point are swapped, generating two new offsprings.

- **Mutation:** Each crystal undergoes a mutation step with a probability of 0.9. During this step, the orientation of each domain within the crystal may be flipped. The probability of flipping a domain is inversely proportional to the total length of the crystal.

- **Population Injection:** To prevent premature convergence and maintain diversity, 10% of each new generation consists of newly generated, randomly poled crystals. This ensures exploration of larger areas of the solution space.

These genetic mechanisms are designed to iteratively refine the crystal designs, promoting continuous improvement and adaptation across successive generations.

5.3 Results

All the results presented in this section have been done for a Potassium Titanyl Phosphate (KTP) crystal. More specifically, for type-II quasi phase matching with a gaussian pump centered around 792 nm with a Full Width at Half Maximum of 15 nm and signal/idler photons centered around 1584 nm.

PMF Optimization

The PMF Optimization algorithm developed during this project has been made available as an open-source tool on GitHub [73]. To demonstrate its broad applicability, several test cases were conducted. The primary objective was to design a pure entangled photon source by optimizing for a broadband and separable Joint Spectral Amplitude (JSA). A Gaussian target function with a Full Width at Half Maximum of 30 nm was used. The crystal length was allowed to vary between 1 mm and 3 mm, and the genetic algorithm operated with a population size of 200 over 200 generations. The optimized design resulted in a crystal length of approximately 1.2 mm, with the corresponding poling function shown in Figure 5.2(f). The associated phase matching function, as a function of the phase mismatch, is displayed in Figure 5.2(b). Figure 5.2(d) shows the resulting JSA, with a purity estimated at 98.5%. The purity was calculated following the method of Graffitti et al. [29], using Schmidt decomposition on the discretized JSA matrix of 100×100 over a range about eight times the PMF spectral width. The Schmidt coefficients are presented in Figure 5.2(h).

Additionally, Figures 5.2 shows the comparison with a standard periodically poled KTP crystal. Figures 5.2(e) and (a) show the poling function and the corresponding phase matching function, respectively. The JSA for this case, presented in Figure 5.2(c), yielded a purity of 82%, with the associated Schmidt coefficients shown in Figure 5.2(g).

Compared to the results reported by Graffitti et al. [29], which achieved a purity of 99.4% but with half the spectral bandwidth, the findings here show a slightly lower purity. Performance improvements to the algorithm could potentially be made by increasing the population size or the number of generations. However, the algorithm proposed by Schmidt et al. is considered to be faster and more efficient for Gaussian profiles, but it requires the user to input well-chosen parameters such as crystal length, target PMF amplitude, and domain width for successful convergence. If these initial parameters are too far from the optimal solution, the

algorithm may fail to converge, requiring an iterative process of parameter adjustment.

In contrast, the genetic algorithm developed in this work can explore a less constrained solution space, with variable crystal length and PMF amplitude, but tends to converge more slowly. A hybrid approach could be considered in future work, where the GA first finds parameters close to the optimal solution, which can then be refined using Graffitti et al.'s algorithm to achieve faster convergence.

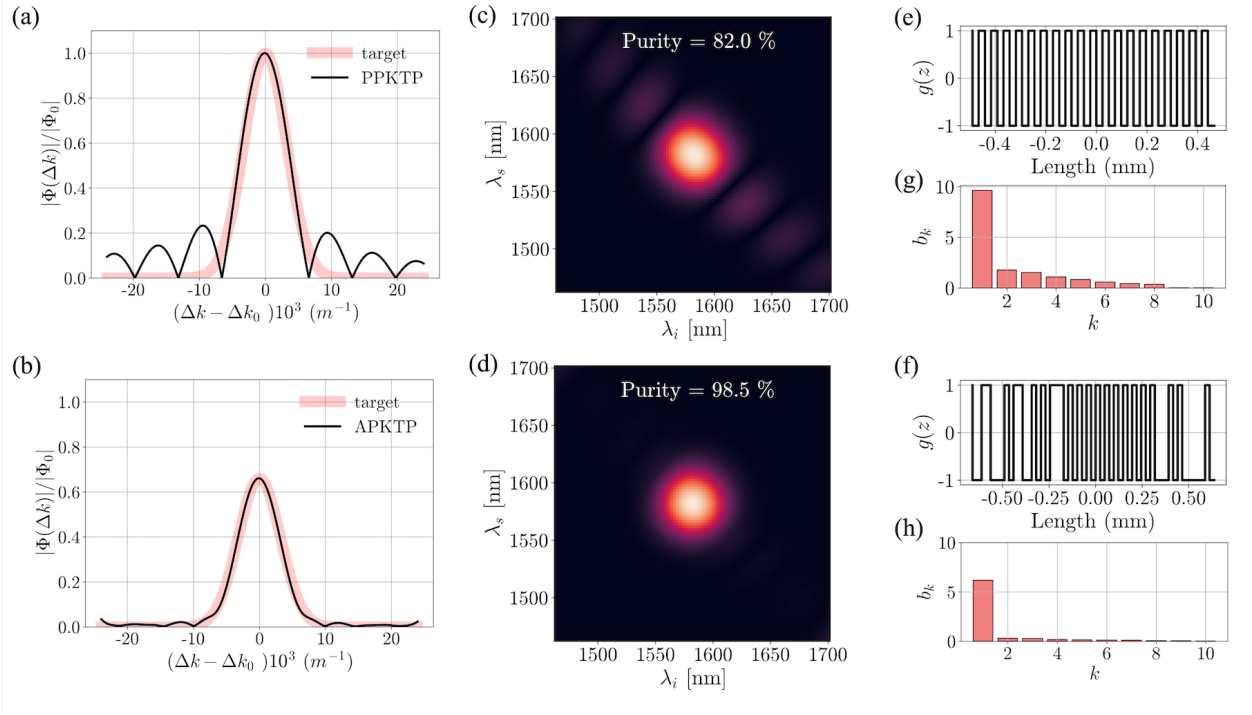

Figure 5.2 Poling profiles, phase matching functions, and JSAs for PPKTP and APKTP crystals. (a) Phase matching function for PPKTP. (b) Phase matching function for APKTP. (c) Joint Spectral Amplitude (JSA) for PPKTP. (d) JSA for APKTP. (e) Poling profile for PPKTP. (f) Poling profile for APKTP. $|\Phi_0|$ represents the absolute peak amplitude of the phase matching function for the PPLN crystal.

To validate the performance of the Genetic Algorithm, Figure 5.3(a) and (b) show the evolution of the average fitness and the best crystal fitness over successive generations for the example shown in Figure 5.2(b). Both fitness metrics exhibit exponential decay, consistent with expected GA behavior [72]. Moreover, Figure 5.3(b) illustrates that the algorithm maintains a consistent standard deviation across generations, effectively preventing premature convergence. The evolution of the mean crystal length over generations, presented in Figure 5.3(d), shows a tendency toward the length of the best crystal, despite minor offsets due to the population injection mechanism at each iteration.

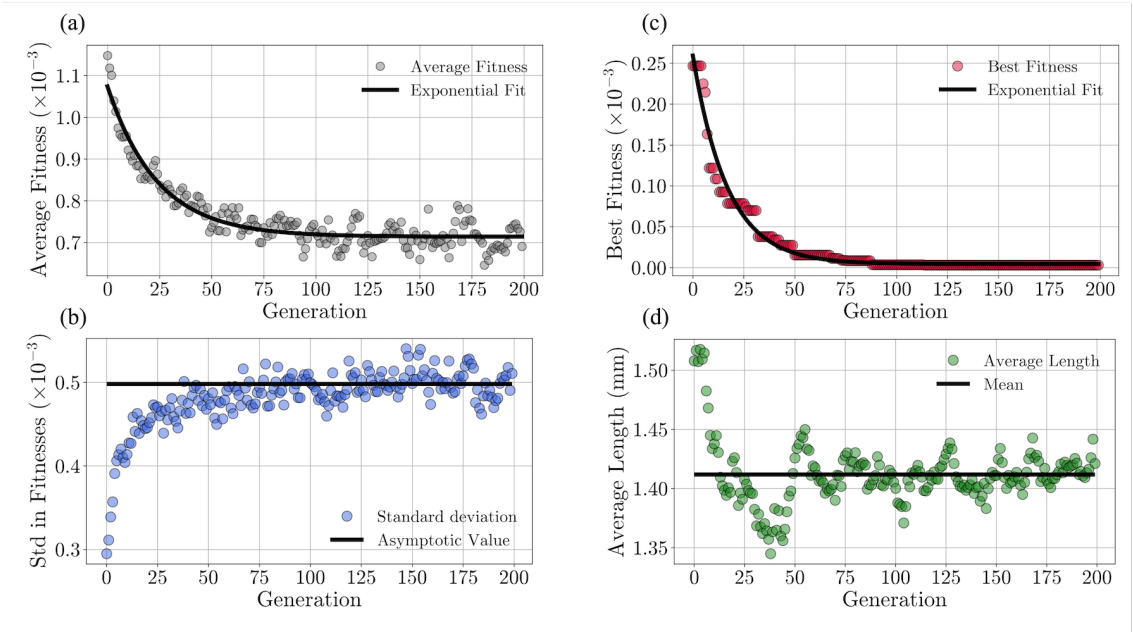

Figure 5.3 Evolution of fitness and crystal length metrics during GA optimization. (a) Average fitness across generations. (b) Best crystal fitness across generations. (c) Standard deviation of fitness across generations. (d) Mean crystal length evolution across generations.

Finally, the GA demonstrates potential advantages in optimizing non-conventional or complex profiles, where traditional methods, such as simulated annealing, may be less effective. To further showcase the versatility of the algorithm, several additional cases were tested, as shown in Figure 5.4. The phase matching functions and their corresponding poling functions are presented for various target profiles, including triangular, multiple Gaussian peaks, rectangular, and Tukey window shapes [74].

NCME Algorithm

Before doing any optimization, the Nonlinear Coupled Mode Equations are solved for two well-known cases—bulk KTP and periodically poled KTP (PPKTP)—to establish a baseline for the spectral characteristics targeted for improvement. The context for this analysis involves a Gaussian pump with a 15 nm FWHM bandwidth centered at 792 nm, designed to generate signal and idler photons centered at 1584 nm. Here the goal is set to achieve a spectral output as close as possible to a target Gaussian profile with a 30 nm FWHM bandwidth centered at 1584 nm.

Figure 5.5 illustrates the results for both the bulk KTP and Periodically Poled Potassium Titanyl Phosphate (PPKTP) cases. Figures 5.5(a), (b), and (c) present the poling profile,

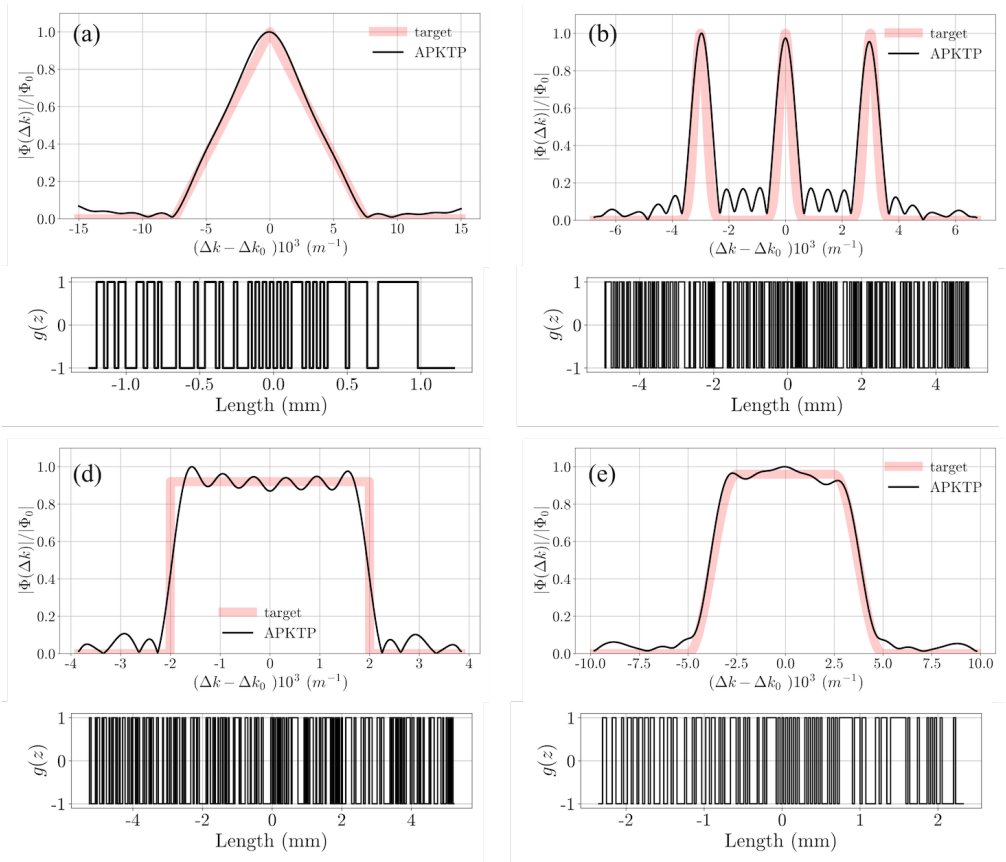

Figure 5.4 Phase matching functions and poling profiles for various target shapes. (a) Triangular target. (b) Multiple Gaussian peaks target. (c) Rectangular target. (d) Tukey window target. Each phase matching function is normalized to its absolute peak amplitude $|\Phi_0|$.

field intensity evolution along the propagation distance z, and the corresponding signal/idler spectra for the bulk KTP. The bulk crystal exhibits the characteristic oscillatory field intensity pattern, with a period matching the coherence length of the process, as discussed in Section 2.2.1. However, this oscillation decays along the propagation distance due to the broad spectral bandwidth of the pump.

Figures 5.5(d), (e), and (f) present the corresponding results for the PPKTP crystal. The periodic poling leads to an enhanced field intensity along the z-axis, promoting more efficient nonlinear interactions. Despite this, the signal/idler spectra exhibit significant sidelobes, deviating from the desired Gaussian target.

Given the persistence of sidelobes in the PPKTP case, the NCME algorithm was subsequently applied to the Aperiodically Poled Potassium Titanyl Phosphate (APKTP) crystal design presented in the previous section (see figure 5.2(b)). Figures 5.6(a), (b), and (c) show the poling profile, field intensity evolution, and signal/idler spectra for the APKTP crystal under

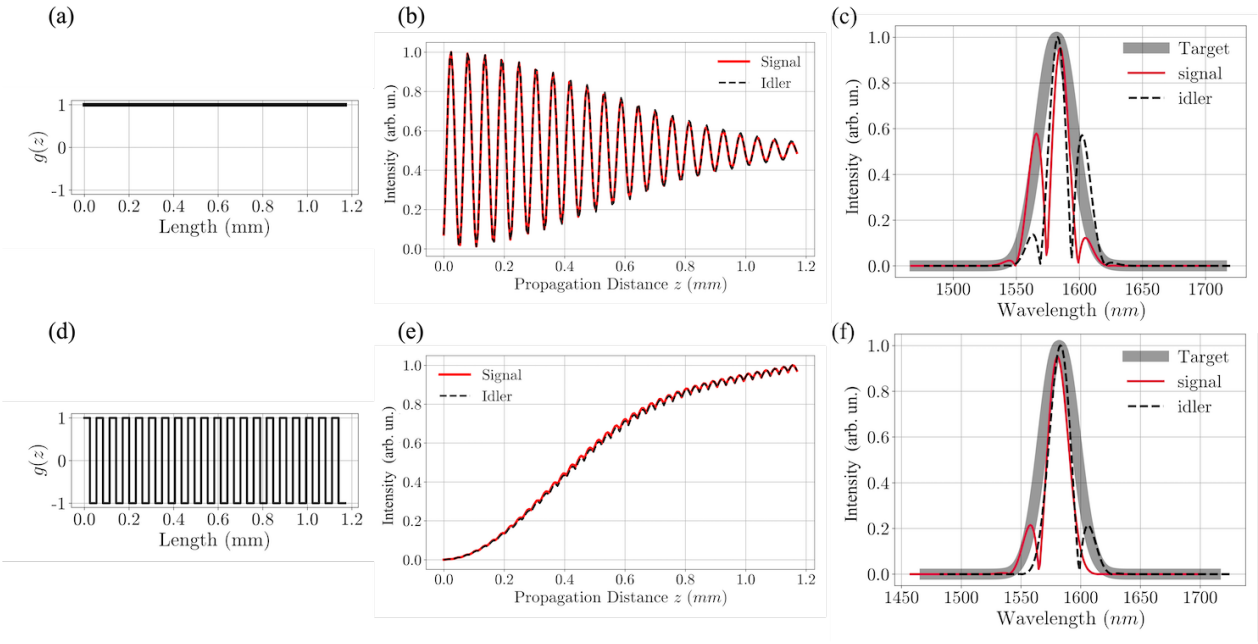

Figure 5.5 (a) Poling profile, (b) field intensity evolution, and (c) signal/idler spectra for bulk KTP. (d) Poling profile, (e) field intensity evolution, and (f) signal/idler spectra for PPKTP.

the same Gaussian pump conditions. While the spectral output shows an improvement over the PPKTP case, with reduced sidelobes, it still falls short of perfectly matching the target Gaussian profile.

To further refine the spectral characteristics, the Genetic Algorithm is finally applied to optimize the poling function of the APKTP crystal. The GA was run with a population size of 100 over 200 generations, using the same Gaussian pump and targeting a Gaussian profile with a 30 nm FWHM bandwidth centered at 1584 nm. Figures 5.6(d), (e), and (f) present the results of this optimization. The optimized poling profile led to a significant reduction in sidelobes, achieving a spectral output closely aligned with the target function. This demonstrates the effectiveness of the GA in fine-tuning the nonlinear response of the crystal, resulting in a more desirable spectral output.

5.4 Discussion

The optimization of KTP crystal poling profiles, using Phase-Matching Function and Nonlinear Coupled Mode Equations methods with the support of a Genetic Algorithm, has demonstrated significant potential in improving the spectral characteristics of entangled photon sources.

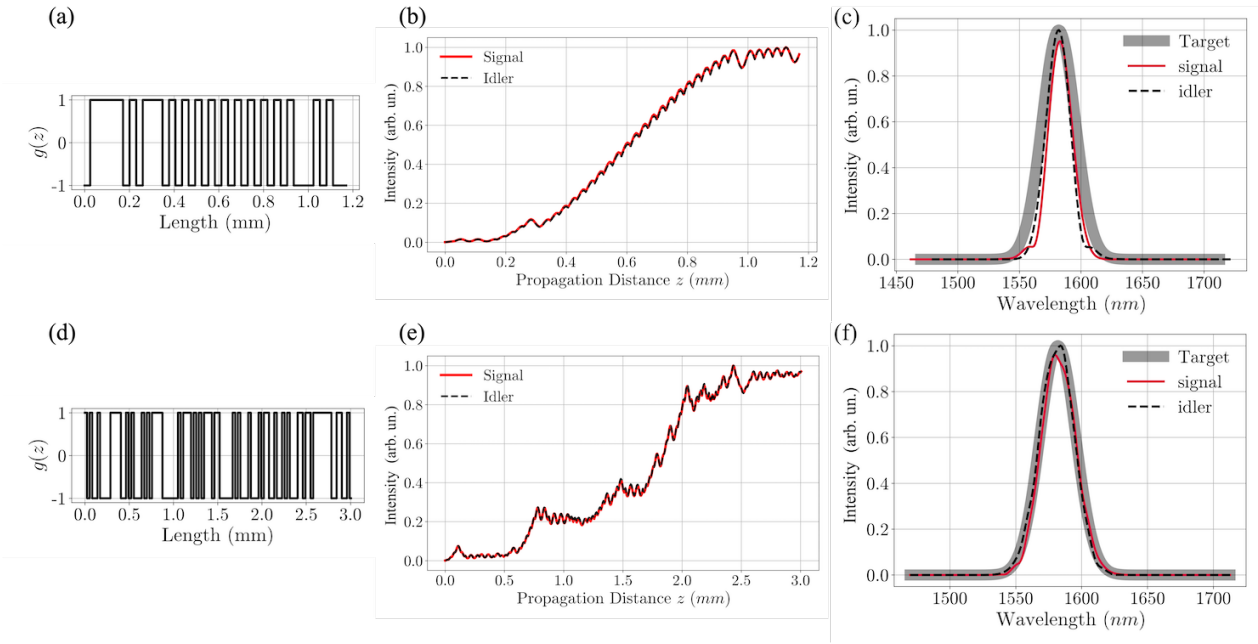

Figure 5.6 (a) Poling profile, (b) field intensity evolution, and (c) signal/idler spectra for APKTP before GA optimization. (d) Poling profile, (e) field intensity evolution, and (f) signal/idler spectra for APKTP after GA optimization.

The PMF Optimization demonstrated its effectiveness in tailoring the nonlinear profile of the crystal to achieve a highly separable Joint Spectral Amplitude. The genetic algorithm proved particularly useful in navigating the complex solution space, allowing the identification of a crystal design that yields a purity of 98.5% for the target Gaussian spectrum.

The NCME Optimization method further extended the capabilities of the crystal design process by directly modeling the dynamics of the signal and idler fields within the crystal. The initial analysis of bulk KTP and PPKTP configurations provided a valuable baseline. The GA then successfully found an APKTP design that minimized the sidelobes and brought the signal/idler spectra into close alignment with the target Gaussian profile.

While the Genetic Algorithm is effective in optimizing KTP crystal poling profiles, its success depends heavily on carefully tuning parameters like population size, mutation rates, and crossover probabilities. If these parameters are not well-adjusted, the process can become resource-intensive and inefficient. Additionally, the NCME approach, despite offering a detailed understanding of the nonlinear dynamics in the crystal, introduces further complexity. It is more computationally intensive and its outcomes are highly dependent on external factors like pump characteristics (e.g., chirp, noise). Small deviations in experimental conditions can significantly affect the results, reducing the robustness of this method. In contrast,

PMF optimization targets the intrinsic properties of the crystal, which can be fine-tuned experimentally, such as through temperature adjustments, making it a more stable and experimentally controllable option in many cases.

CHAPTER 6 CONCLUSION

6.1 Summary of Works

This thesis outlines the initial efforts toward developing a bright source of entangled photons. The focus has been on designing and characterizing the ultrafast fiber laser system, implementing the Second Harmonic Generation stage, and developing an algorithm to optimize second-order nonlinear materials. These components are fundamental to the Spontaneous Parametric Down-Conversion process, which will be further investigated in future research, including a subsequent master thesis.

In Chapter 3, a low-noise ultrafast fiber laser system was developed to serve as the pump source for the SHG stage. The system comprises a Master Oscillator (MO) that operates in both first and second-order soliton regimes, as well as an Erbium-Doped Fiber Amplifier. The MO exhibited stable performance, producing pulse energies between 30 and 75 pJ with pulse durations ranging from 594 to 261 fs, and an integrated RMS Relative Intensity Noise of approximately 0.081%. The EDFA further amplified these pulses, increasing the spectral bandwidth from 4.5 nm to 55 nm, with a maximum averaged output power of 265 mW. SHG FROG measurements recorded pulse durations of 102 fs in the first-order soliton regime and 136 fs in the second-order regime at the EDFA output.

Chapter 4 described the SHG stage, which employed a MgO-doped periodically poled lithium niobate crystal. The system was optimized to generate maximum SH power at a 19.7 μm grating period and a crystal temperature of 70 °C. This setup produced a second harmonic output of 46 mW average power centered at 792 nm with an autocorrelation trace showing a full-width at half-maximum of 105 fs.

In Chapter 5, an algorithm was developed to optimize second-order nonlinear materials critical for the SPDC process. The algorithm used both Phase-Matching Function (PMF) and Nonlinear Coupled Mode Equations (NCME) methods, guided by a Genetic Algorithm (GA). The PMF optimization achieved a Joint Spectral Amplitude with 98.5% purity and a 30 nm bandwidth centered at 1584 nm. The NCME method further refined the crystal design by reducing spectral sidelobes. Additionally, the PMF optimization algorithm demonstrated its capability to handle non-conventional target profiles effectively.

6.2 Limitations

While this work has made significant progress, several areas offer opportunities for further improvement. The stability of the ultrafast fiber laser system was influenced by pump technical noise at lower frequencies, and RIN measurements were constrained above 1 MHz due to photodetection shot noise. Additionally, third-order dispersion and Self-Phase Modulation in the EDFA led to satellite pulses, which introduced challenges in achieving transform-limited pulse durations.

In the SHG setup, the maximum achievable second harmonic power was constrained by the damage threshold of the PPLN crystal. Moreover, the autocorrelation trace of the SHG pulse revealed the presence of satellite pulses, suggesting that the pulse shape could be further optimized.

The Genetic Algorithm effectively optimized KTP crystal poling profiles but required careful tuning of key parameters like population size and mutation rates. While the PMF optimization provided more reliable experimental results by focusing on the intrinsic parameters of the crystal, the NCME method is believed to be more sensitive to external factors, such as pump characteristics, making experimental applications more complex.

6.3 Future Research

Future research should aim to reduce RIN in the ultrafast fiber laser system, particularly at low frequencies, potentially through pump stabilization techniques. Advanced dispersion management, such as using a prism compressor or chirped mirror pairs, could mitigate higher-order dispersion effects, moving closer to achieving transform-limited pulses.

For the SHG setup, exploring alternative crystals like KTP and complex designs like aperiodic poling and fanout configurations could increase SH power and bandwidth flexibility. Implementing SHG FROG on the SH pulse would provide a more detailed temporal characterization, and applying a two-prism pulse compressor on the pump before the SHG stage could help reduce these satellite pulses observed in the autocorrelation trace. Additionally, further study of the single-prism pulse compressor and SHG properties under second-order soliton conditions is recommended.

For optimizing second-order nonlinear materials, incorporating more physics-based constraints could narrow the solution search space. Refining GA hyper-parameters and exploring alternative algorithms, such as gradient descent or machine learning, could lead to more robust solutions. Additionally, a hybrid approach combining the strengths of the GA for exploring

a broader, less constrained solution space with simulated annealing for refining the solution within a smaller space could potentially offer improved performance.

Experimental validation of SPDC predictions and spectral purity optimization will be crucial. A collaboration with the Fabulas Lab at Polytechnique Montréal is already underway to advance the development of these critical nonlinear materials. Continued research, including a follow-up master thesis, will focus on the development and implementation of the SPDC process.

REFERENCES

[1] A. Labranche, "Conception of a Low-Noise Ultrafast Fiber Laser System Toward nJ Phase Stable Pulses in the Mid-Infrared," Master's thesis, Polytechnique Montréal, 2020.

[2] K. C. Tan and H. Jeong, "Nonclassical Light and Metrological Power: An Introductory Review," *AVS Quantum Science*, vol. 1, no. 1, p. 014701, Dec. 2019.

[3] P.-A. Moreau, E. Toninelli, T. Gregory, and M. J. Padgett, "Imaging with quantum states of light," *Nature Reviews Physics*, vol. 1, no. 6, pp. 367–380, Jun. 2019.

[4] V. Giovannetti, S. Lloyd, and L. Maccone, "Advances in quantum metrology," *Nature Photonics*, vol. 5, no. 4, pp. 222–229, Apr. 2011.

[5] T. L. Collaboration, "Enhanced sensitivity of the LIGO gravitational wave detector by using squeezed states of light," *Nature Photonics*, vol. 7, no. 8, pp. 613–619, Aug. 2013.

[6] M. D. Eisaman, J. Fan, A. Migdall, and S. V. Polyakov, "Invited Review Article: Single-photon sources and detectors," *Review of Scientific Instruments*, vol. 82, no. 7, p. 071101, Jul. 2011.

[7] A. Dutta, "Chapter 4 - Fourier Transform Infrared Spectroscopy," in *Spectroscopic Methods for Nanomaterials Characterization*, ser. Micro and Nano Technologies, S. Thomas, R. Thomas, A. K. Zachariah, and R. K. Mishra, Eds. Elsevier, 2017, pp. 73–93.

[8] K. Hashimoto, D. B. Horoshko, M. I. Kolobov, Y. Michael, Z. Gefen, and M. V. Chekhova, "Fourier-transform infrared spectroscopy with undetected photons from high-gain spontaneous parametric down-conversion," *Communications Physics*, vol. 7, no. 1, pp. 1–7, Jul. 2024.

[9] G. M. D'Ariano, M. D. Laurentis, M. G. A. Paris, A. Porzio, and S. Solimeno, "Quantum tomography as a tool for the characterization of optical devices," *Journal of Optics B: Quantum and Semiclassical Optics*, vol. 4, no. 3, p. S127, Mar. 2002.

[10] A. I. Lvovsky and M. G. Raymer, "Continuous-variable optical quantum-state tomography," *Reviews of Modern Physics*, vol. 81, no. 1, pp. 299–332, Mar. 2009.

[11] A. F. Abouraddy, M. B. Nasr, B. E. A. Saleh, A. V. Sergienko, and M. C. Teich, "Quantum-optical coherence tomography with dispersion cancellation," *Physical Review A*, vol. 65, no. 5, 2002.

[12] Z. Ibarra-Borja, C. Sevilla-Gutiérrez, R. Ramírez-Alarcón, H. Cruz-Ramírez, and A. B. U'Ren, "Experimental demonstration of full-field quantum optical coherence tomography," *Photonics Research*, vol. 8, no. 1, 2020.

[13] S. Virally, P. Cusson, and D. V. Seletskiy, "Enhanced Electro-optic Sampling with Quantum Probes," *Physical Review Letters*, vol. 127, no. 27, p. 270504, Dec. 2021.

[14] G. P. Agrawal, *Nonlinear Fiber Optics*, 6th ed. Academic Press, 2019.

[15] L. Rivard, "Development of a Versatile 76 MHz Fiber Based Source of 9-fs Pulses in the Near-Infrared and Phase-Stable ps Pulses in the Mid-Infrared," Master's thesis, Polytechnique Montréal, 2023.

[16] B. E. A. Saleh and M. C. Teich, *Fundamentals of Photonics*, 2nd ed. Wiley-Interscience, 2007.

[17] D. Marcuse, *Theory of Dielectric Optical Waveguides, Second Edition.* Academic Press, 2012.

[18] A. S. Rao, "Overview on Second and Third Order Optical Nonlinear Processes," Dec. 2016.

[19] A. Diebold, T. Zengerle, C. G. E. Alfieri, C. Schriber, F. Emaury, M. Mangold, M. Hoffmann, C. J. Saraceno, M. Golling, D. Follman, G. D. Cole, M. Aspelmeyer, T. Südmeyer, and U. Keller, "Optimized SESAMs for kilowatt-level ultrafast lasers," *Optics Express*, vol. 24, no. 10, pp. 10 512–10 526, May 2016.

[20] R. W. Boyd, *Nonlinear Optics*, 3rd ed. Academic Press, 2008.

[21] G. Imeshev, M. A. Arbore, M. M. Fejer, A. Galvanauskas, M. Fermann, and D. Harter, "Ultrashort-pulse second-harmonic generation with longitudinally nonuniform quasi-phase-matching gratings: pulse compression and shaping," *JOSA B*, vol. 17, no. 2, pp. 304–318, Feb. 2000.

[22] E. Rozenberg, A. Karnieli, O. Yesharim, J. Foley-Comer, S. Trajtenberg-Mills, D. Freedman, A. M. Bronstein, and A. Arie, "Inverse design of spontaneous parametric down-conversion for generation of high-dimensional qudits," *Optica*, vol. 9, no. 6, pp. 602–615, Jun. 2022.

[23] L. Peng, L. Hong, and Z. Li, "Theoretical solution of second-harmonic generation in periodically poled lithium niobate and chirped periodically poled lithium niobate thin film via quasi-phase-matching," *Physical Review A*, vol. 104, no. 5, p. 053503, Nov. 2021.

[24] A. Christ, A. Fedrizzi, H. Hübel, T. Jennewein, and C. Silberhorn, "Chapter 11 - Parametric Down-Conversion," in *Experimental Methods in the Physical Sciences*, ser. Single-Photon Generation and Detection, A. Migdall, S. V. Polyakov, J. Fan, and J. C. Bienfang, Eds. Academic Press, Jan. 2013, vol. 45, pp. 351–410.

[25] G. Harder, "Optimized down-conversion source and state-characterization tools for quantum optics," Ph.D. dissertation, Universität Paderborn, 2016.

[26] A. U'Ren, C. Silberhorn, R. Erdmann, K. Banaszek, W. Grice, I. Walmsley, and M. Raymer, "Generation of Pure-State Single-Photon Wavepackets by Conditional Preparation Based on Spontaneous Parametric Downconversion," *Laser Physics*, vol. 15, Dec. 2006.

[27] P. J. Mosley, J. S. Lundeen, B. J. Smith, P. Wasylczyk, A. B. U'Ren, C. Silberhorn, and I. A. Walmsley, "Heralded Generation of Ultrafast Single Photons in Pure Quantum States," *Physical Review Letters*, vol. 100, no. 13, p. 133601, Apr. 2008.

[28] E. Ramos-Israde, K. Garay-Palmett, and R. S. Cudney, "Randomly aperiodically poled $LiNbO_3$ crystal design by Monte Carlo–Metropolis with simulated annealing optimization for ultrabroadband photon pair generation," *Applied Optics*, vol. 60, no. 34, pp. 10 587–10 593, Dec. 2021.

[29] F. Graffitti, D. Kundys, D. T. Reid, A. M. Brańczyk, and A. Fedrizzi, "Pure down-conversion photons through sub-coherence-length domain engineering," *Quantum Science and Technology*, vol. 2, no. 3, p. 035001, Jul. 2017.

[30] M. W. Mitchell, "Parametric down-conversion from a wave-equation approach: Geometry and absolute brightness," *Physical Review A*, vol. 79, no. 4, p. 043835, Apr. 2009.

[31] E. Brambilla, A. Gatti, M. Bache, and L. A. Lugiato, "Simultaneous near-field and far-field spatial quantum correlations in the high-gain regime of parametric down-conversion," *Physical Review A*, vol. 69, no. 2, p. 023802, Feb. 2004.

[32] G. Divyangna, "Evaluation of Gain and Noise Figure Spectrum of EDFA by Optimizing its Parameters with Different Pumping Schemes in the Scenario of WDM System," in *Emerging Technology Trends in Electronics, Communication and Networking*, S. Gupta and J. N. Sarvaiya, Eds. Springer, 2020, pp. 136–146.

[33] S. Kumar and F. Lederer, "Gordon–Haus effect in dispersion-managed soliton systems," *Optics Letters*, vol. 22, no. 24, pp. 1870–1872, Dec. 1997.

[34] J. P. Gordon and H. A. Haus, "Random walk of coherently amplified solitons in optical fiber transmission," *Optics Letters*, vol. 11, no. 10, Oct. 1986.

[35] M. Dennis and I. Duling, "Experimental study of sideband generation in femtosecond fiber lasers," *IEEE Journal of Quantum Electronics*, vol. 30, no. 6, pp. 1469–1477, Jun. 1994.

[36] S. R. Friberg and K. W. DeLong, "Breakup of bound higher-order solitons," *Optics Letters*, vol. 17, no. 14, pp. 979–981, Jul. 1992.

[37] C. R. Smith, R. D. Engelsholm, and O. Bang, "Pulse-to-pulse relative intensity noise measurements for ultrafast lasers," *Optics Express*, vol. 30, no. 5, pp. 8136–8150, Feb. 2022.

[38] J. Kim and Y. Song, "Ultralow-noise mode-locked fiber lasers and frequency combs: principles, status, and applications," *Advances in Optics and Photonics*, vol. 8, no. 3, pp. 465–540, Sep. 2016.

[39] R. Hui and M. O'Sullivan, "Chapter 3 - Characterization of Optical Devices," in *Fiber Optic Measurement Techniques*. Academic Press, 2009, pp. 259–363.

[40] C. Kim, K. Jung, K. Kieu, and J. Kim, "Low timing jitter and intensity noise from a soliton Er-fiber laser mode-locked by a fiber taper carbon nanotube saturable absorber," *Optics Express*, vol. 20, no. 28, pp. 29 524–29 530, Dec. 2012.

[41] K. Wu, P. P. Shum, S. Aditya, C. Ouyang, J. H. Wong, H. Q. Lam, and K. E. K. Lee, "Noise conversion from pump to the passively mode-locked fiber lasers at 1.5 μ," *Optics Letters*, vol. 37, no. 11, pp. 1901–1903, Jun. 2012.

[42] C. Kim, D. Kim, Y. Cheong, D. Kwon, S. Y. Choi, H. Jeong, S. J. Cha, J.-W. Lee, D.-I. Yeom, F. Rotermund, and J. Kim, "300-MHz-repetition-rate, all-fiber, femtosecond laser mode-locked by planar lightwave circuit-based saturable absorber," *Optics Express*, vol. 23, no. 20, pp. 26 234–26 242, Oct. 2015.

[43] H. Byun, M. Y. Sander, A. Motamedi, H. Shen, G. S. Petrich, L. A. Kolodziejski, E. P. Ippen, and F. X. Kärtner, "Compact, stable 1 GHz femtosecond Er-doped fiber lasers," *Applied Optics*, vol. 49, no. 29, pp. 5577–5582, Oct. 2010.

[44] T. C. Schratwieser, C. G. Leburn, and D. T. Reid, "Highly efficient 1 GHz repetition-frequency femtosecond Yb3+:KY(WO4)2 laser," *Optics Letters*, vol. 37, no. 6, pp. 1133–1135, Mar. 2012.

[45] J. Nicholson, A. Yablon, P. Westbrook, K. Feder, and M. Yan, "High power, single mode, all-fiber source of femtosecond pulses at 1550 nm and its use in supercontinuum generation," *Optics Express*, vol. 12, no. 13, pp. 3025–3034, Jun. 2004.

[46] F. Tauser, A. Leitenstorfer, and W. Zinth, "Amplified femtosecond pulses from an Er:fiber system: Nonlinear pulse shortening and self-referencing detection of the carrier-envelope phase evolution," *Optics Express*, vol. 11, no. 6, pp. 594–600, Mar. 2003.

[47] F. O. Ilday, J. R. Buckley, W. G. Clark, and F. W. Wise, "Self-Similar Evolution of Parabolic Pulses in a Laser," *Physical Review Letters*, vol. 92, no. 21, p. 213902, May 2004.

[48] R. H. Stolen and C. Lin, "Self-phase-modulation in silica optical fibers," *Physical Review A*, vol. 17, no. 4, pp. 1448–1453, Apr. 1978.

[49] J. P. Gordon, "Theory of the soliton self-frequency shift," *Optics Letters*, vol. 11, no. 10, pp. 662–664, Oct. 1986.

[50] D. Strickland and G. Mourou, "Compression of amplified chirped optical pulses," *Optics Communications*, vol. 56, no. 3, pp. 219–221, Dec. 1985.

[51] R. Trebino, *Frequency-Resolved Optical Gating: The Measurement of Ultrashort Laser Pulses*, 2000th ed. Springer, 2002.

[52] A. M. Weiner, *Ultrafast Optics*, 1st ed. Wiley, 2009.

[53] "Frequency-resolved optical gating (FROG)," Aug. 2024. [Online]. Available: https://www.mathworks.com/matlabcentral/fileexchange/34986-frequency-resolved-optical-gating-frog

[54] D. Kane, "Recent progress toward real-time measurement of ultrashort laser pulses," *IEEE Journal of Quantum Electronics*, vol. 35, no. 4, pp. 421–431, Apr. 1999.

[55] G. D. Boyd and D. A. Kleinman, "Parametric Interaction of Focused Gaussian Light Beams," *Journal of Applied Physics*, vol. 39, no. 8, pp. 3597–3639, Jul. 1968.

[56] M. McGeoch and R. Smith, "Optimum second-harmonic generation in lithium niobate," *IEEE Journal of Quantum Electronics*, vol. 6, no. 4, pp. 203–205, Apr. 1970.

[57] M. Aillerie, P. Bourson, M. Mostefa, F. Abdi, and M. D. Fontana, "Photorefractive Damage in congruent LiNbO3. Part II. Magnesium doped Lithium Niobate Crystals," *Journal of Physics: Conference Series*, vol. 416, no. 1, p. 012002, Mar. 2013.

[58] Y. Furukawa, K. Kitamura, A. Alexandrovski, R. K. Route, M. M. Fejer, and G. Foulon, "Green-induced infrared absorption in MgO doped LiNbO3," *Applied Physics Letters*, vol. 78, no. 14, pp. 1970–1972, Apr. 2001.

[59] O. Gayer, Z. Sacks, E. Galun, and A. Arie, "Temperature and wavelength dependent refractive index equations for MgO-doped congruent and stoichiometric LiNbO3," *Applied Physics B*, vol. 91, no. 2, pp. 343–348, May 2008.

[60] V. K. Chauhan, J. Cohen, P. M. Vaughan, P. Bowlan, and R. Trebino, "Distortion-Free Single-Prism/Grating Ultrashort Laser Pulse Compressor," *IEEE Journal of Quantum Electronics*, vol. 46, no. 12, pp. 1726–1731, Dec. 2010.

[61] A. K. Gunther, "PPLN-based photon pair sources toward biphoton quantum frequency conversion," Ph.D. dissertation, University of Waterloo, Aug. 2018.

[62] P. Wasylczyk, "Ultracompact autocorrelator for femtosecond laser pulses," *Review of Scientific Instruments*, vol. 72, no. 4, pp. 2221–2223, Apr. 2001.

[63] A. Anwar, C. Perumangatt, F. Steinlechner, T. Jennewein, and A. Ling, "Entangled photon-pair sources based on three-wave mixing in bulk crystals," *Review of Scientific Instruments*, vol. 92, no. 4, p. 041101, Apr. 2021.

[64] W. Ma, Z. Liu, Z. A. Kudyshev, A. Boltasseva, W. Cai, and Y. Liu, "Deep learning for the design of photonic structures," *Nature Photonics*, vol. 15, no. 2, pp. 77–90, Feb. 2021.

[65] P. R. Wiecha, A. Arbouet, C. Girard, and O. L. Muskens, "Deep learning in nano-photonics: inverse design and beyond," *Photonics Research*, vol. 9, no. 5, pp. B182–B200, May 2021.

[66] S. Ren, A. Mahendra, O. Khatib, Y. Deng, W. J. Padilla, and J. M. Malof, "Inverse deep learning methods and benchmarks for artificial electromagnetic material design," *Nanoscale*, vol. 14, no. 10, pp. 3958–3969, Mar. 2022.

[67] A. Dosseva, L. Cincio, and A. M. Branczyk, "Shaping the joint spectrum of down-converted photons through optimized custom poling," *Physical Review A*, vol. 93, no. 1, p. 013801, Jan. 2016.

[68] Z. He, K. Yuan, G. Xiong, and J. Wang, "Inverse Design and Experimental Verification of Metamaterials for Thermal Illusion Using Genetic Algorithms," *Chinese Physics Letters*, vol. 40, no. 10, p. 104402, Oct. 2023.

[69] S. Xiao, F. Zhao, D. Wang, J. Weng, Y. Wang, X. He, H. Chen, Z. Zhang, Y. Yu, Z. Zhang, Z. Zhang, and J. Yang, "Inverse design of a near-infrared metalens with an extended depth of focus based on double-process genetic algorithm optimization," *Optics Express*, vol. 31, no. 5, pp. 8668–8681, Feb. 2023.

[70] R. Tom, S. Gao, Y. Yang, K. Zhao, I. Bier, E. A. Buchanan, A. Zaykov, Z. Havlas, J. Michl, and N. Marom, "Inverse Design of Tetracene Polymorphs with Enhanced Singlet Fission Performance by Property-Based Genetic Algorithm Optimization," *Chemistry of Materials: A Publication of the American Chemical Society*, vol. 35, no. 3, pp. 1373–1386, Feb. 2023.

[71] Z. Zhang, L. Chen, and X. Bao, "A fourth-order Runge-Kutta in the interaction picture method for numerically solving the coupled nonlinear Schrodinger equation," *Optics Express*, vol. 18, no. 8, pp. 8261–8276, Apr. 2010.

[72] S. Katoch, S. S. Chauhan, and V. Kumar, "A review on genetic algorithm: past, present, and future," *Multimedia Tools and Applications*, vol. 80, no. 5, pp. 8091–8126, Feb. 2021.

[73] Colin Dietrich, "colinDietrich/GaPmf." [Online]. Available: https://github.com/colinDietrich/GaPmf

[74] F. Harris, "On the use of windows for harmonic analysis with the discrete Fourier transform," *Proceedings of the IEEE*, vol. 66, no. 1, pp. 51–83, Jan. 1978.

APPENDIX A COMPONENTS OF THE LASER SETUP

Table A.1 Detailed Components List

Component	**Model/Part Number**	**Comment**
Fiber Bragg grating stabilized pump diode (605mW)	1999CMB	Pump diode for the MO.
Fiber Bragg grating stabilized pump diode (1050mW)	1999CVB	Pump diode for the EDFA.
Saturable absorber mirror	SAM-1550-21-2ps-x	Mounted on a passive heat sink.
Polarization maintaining fiber	PM1550-XP	Same PM fiber for MO and EDFA.
Highly doped PM erbium fiber	Er80-4/125-HD-PM	Same fiber for MO and EDFA.
Wavelength division multiplexer	WDM-PM-1598-B-P-7-0-1W	Routes CW pump light counter-directionally. Same for MO and EDFA.
Output coupler 30/70	PCF-15-1-30-B-P-7-0-FB	Directs 65% power back into cavity, 29% output.
Polarization maintaining circulator	IO-G-1550	Ensures unidirectional light flow.
Optical isolator - Master oscillator	IO-G-1550	Minimize feedback into optical cavity at the output of the MO.
Optical isolator - EDFA	HPMI-98-01-N-L-Q-F-1-P	High power optical isolator for the pumps driving the EDFA.
Thermoelectric Temperature Controller	LDT-5525B	Controls temperature of SAM.
Laser diode controller	CLD1015	Laser Diode and Temperature Controller to drive and cool pigtailed butterfly laser diodes for MO and EDFA.

APPENDIX B VYTRAN SPLICING PARAMETERS FOR POLARIZATION-MAINTAINING AND ERBIUM-DOPED FIBERS

Table B.1 Splice Parameters for PM1550-Er80 Fiber Splicing

Splice Parameters	**Units**	**Pm1550-Er80_POLISH**
Gas Flow / Argon	l/min	0.65
Splice power	W	20
Filament on time	sec	3
Fiber push velocity	steps/sec	700
Fiber pre-push distance	$\times 10^{-6}$ m	5
Fiber pre-gap distance	$\times 10^{-6}$ m	8
Fiber hot push distance	$\times 10^{-6}$ m	12
Hot push delay	ms	350
Fire Polish Parameters		
Fire Polish delta	$\times 10^{-6}$ m	85
Number of passes	ad.	12
Fire polish power	W	18.5
Cool down time	s	90
Velocity	step/s	300
Argon	l/min	0.65
Cool threshold	s	60
PM Alignment Configuration		
Left	ad.	PM-1550
Left diameter	$\times 10^{-6}$ m	125
Left type	ad.	Fuji(Panda)
Left P1	pixels	31
Left P2	pixels	44
Right	ad.	Er-80
Right diameter	$\times 10^{-6}$ m	125
Right type	ad.	Fuji(Panda)
Right P1	pixels	25
Right P2	pixels	40

APPENDIX C SUPPLEMENTARY NOTES ON SPONTANEOUS PARAMETRIC DOWN-CONVERSION (SPDC)

Absolute Brightness

In regimes where the nonlinear interaction permits the use of first-order perturbation theory, one can derive the biphoton generation rates (pairs per second). Schneeloch et al. [30] investigated this under assumptions of a collimated Gaussian pump beam in a bulk nonlinear crystal, a quasi-monochromatic pump, and an undepleted pump approximation, where the pump intensity remains constant throughout the interaction.

The relevant expressions from their results are summarized in Table C.1, including the pump σ_p and signal σ_1 beam widths, the crystal length L_z, effective nonlinear coefficient d_{eff}, group velocity dispersion κ, and group indices for the signal n_{g1} and idler n_{g2} beams with P denoting the pump power. Additionally, $\Delta n_g = |n_{g1} - n_{g2}|$ and $\phi \approx 0.335$.

For periodic poling and higher order quasi-phase matching, one must multiply the biphoton rate by $\frac{4}{n^2\pi^2}$, however this factor is typically included in d_{eff}.

Table C.1 Generation rate formulas for different types of SPDC. SM/MM respectively stand for single-/multi-mode.

Type	**Formula**
Type-0/I, SM	$\sqrt{\frac{2}{\pi^3}}\frac{2}{3\epsilon_0 c^3}\frac{n_{g1}n_{g2}}{n_1^2 n_2^2 n_p}\frac{d_{\text{eff}}^2\omega_p^2}{\sqrt{\kappa}}\left\lvert\frac{\sigma_p^2}{\sigma_1^2+2\sigma_p^2}\right\rvert^2\frac{P}{\sigma_p^2}L_z^{3/2}$
Type-0/I, MM	$\frac{32\sqrt{2\pi^3}}{27\epsilon_0 c}\frac{n_{g1}n_{g2}}{n_1^2 n_2^2}\frac{d_{\text{eff}}^2}{\lambda_p^3\sqrt{\kappa}}\frac{P\sqrt{L_z}}{\phi}$
Type-II, SM	$\frac{1}{\pi\epsilon_0 c^2}\frac{n_{g1}n_{g2}}{n_1^2 n_2^2 n_p}d_{\text{eff}}^2\omega_p^2\frac{1}{\Delta n_g}\left\lvert\frac{\sigma_p^2}{\sigma_1^2+2\sigma_p^2}\right\rvert^2\frac{P}{\sigma_p^2}L_z$

These formulas serve as theoretical lower bounds for experimental biphoton rates. Particularly, when employing a pulsed Gaussian beam focused within a bulk crystal, the localized enhancement in peak power from temporal and spatial focusing is expected to increase the biphoton generation rates, typically resulting in higher experimental values.

Non-Perturbative Quantum Description of SPDC

To predict outcomes in a stronger pump regime, one can go beyond first-order perturbation theory and extend the calculations to higher-order perturbative terms, revealing effects such as multi-photon generation. Alternatively, it is also possible to analyze SPDC using a non-

perturbative approach, leading to the derivation of the two-mode squeezed vacuum (TMSV) state [30].

Instead of expanding the exponential in (2.64), one can directly apply the squeezing operator to the vacuum state [25]:

$$\begin{aligned} |\text{TMSV}\rangle &= \hat{S}(\zeta)|0\rangle \\ &= \frac{1}{\cosh r}\sum_{n=0}^{\infty}(-e^{i\phi}\tanh r)^n|n,n\rangle \\ &= \sqrt{1-|\lambda|^2}\sum_{n=0}^{\infty}\lambda^n|n,n\rangle \end{aligned} \tag{C.1}$$

Where $\zeta = re^{i\phi}$ is the squeezing parameter and $\lambda = -e^{i\phi}\tanh r$.
This state exhibits perfect photon-number correlations, making it useful for heralding photon-number states or Fock states. By using a photon-number detector on one mode, the corresponding mode is projected onto the detected photon number. This approach is widely used in low-power regimes to generate single photons.

To examine the properties of individual signal or idler modes, one can trace out the complementary mode. For instance, tracing out the idler mode gives the reduced density matrix for the signal mode as:

$$\rho_s = \text{Tr}_i(|\text{TMSV}\rangle\langle\text{TMSV}|) = (1-|\lambda|^2)\sum_{n=0}^{\infty}|\lambda|^{2n}|n\rangle\langle n| \tag{C.2}$$

The probability of having n photons in the remaining mode is given by:

$$P_n = (1-|\lambda|^2)|\lambda|^{2n} = (1-e^{\frac{-\hbar\omega}{k_BT}})e^{\frac{-n\hbar\omega}{k_BT}} \tag{C.3}$$

This expression describes a thermal distribution, following the Boltzmann distribution, where $|\lambda|^2 = e^{\frac{-\hbar\omega}{k_BT}}$, and the mean photon number is $\langle n\rangle = \sinh^2 r$.